Analysis of Signal Propagation and Excitability in Computational Models of an Identified *Drosophila* Motoneuron

by

Sandra Berger

A Dissertation Presented in Partial Fulfillment
of the Requirements for the Degree
Doctor of Philosophy

Approved June 2014 by the
Graduate Supervisory Committee:

Sharon Crook, Chair
Steven Baer
Thomas Hamm
Brian Smith

ARIZONA STATE UNIVERSITY

August 2014

ABSTRACT

Cell morphology and the distribution of voltage gated ion channels play a major role in determining a neuron's firing behavior, resulting in the specific processing of spatiotemporal synaptic input patterns. Although many studies have provided insight into the computational properties arising from neuronal structure as well as from channel kinetics, no comprehensive theory exists which explains how the interaction of these features shapes neuronal excitability. In this study computational models based on the identified *Drosophila* motoneuron (MN) 5 are developed to investigate the role of voltage gated ion channels, the impact of their densities and the effects of structural features.

First, a spatially collapsed model is used to develop voltage gated ion channels to study the excitability of the model neuron. Changing the channel densities reproduces different *in situ* observed firing patterns and induces a switch from resonator to integrator properties. Second, morphologically realistic multicompartment models are studied to investigate the passive properties of MN5. The passive electrical parameters fall in a range that is commonly observed in neurons, MN5 is spatially not compact, but for the single subtrees synaptic efficacy is location independent. Further, different subtrees are electrically independent from each other. Third, a continuum approach is used to formulate a new cable theoretic model to study the output in a dendritic cable with many subtrees, both analytically and computationally. The model is validated, by comparing it to a corresponding model with discrete branches. Further, the approach is demonstrated using MN5 and used to investigate spatially distributions of voltage gated ion channels.

ACKNOWLEDGEMENTS

Dr. Sharon Crook was and is a great advisor; she gave me new insights and improved my skills in scientific working. She was very patient and supported me not only academically. Therefore I owe her my greatest thanks. I am very grateful to Dr. Steven Baer for giving me valuable advice and input and working with me on my research. I also want to thank the other members of my dissertation committee, Dr. Thomas Hamm and Dr. Brian Smith for their feedback and time. I thank Beverly McBride for her help and administrative support.

Special thanks go to Dr. Carsten Duch for helpful discussions and input about neurobiological topics. Moreover I thank him and his lab members Stevie Ryglewski, Fernando Vonhoff and Claudia Kuehn for providing their experimental data. I thank Marco Herrera-Valdez; he expanded my knowledge in computational modeling and his ideas and input helped me to start with my project. I further want to thank Cengiz Gunay for valuable discussions regarding my research. I thank Felix Evers for helping me getting started with NEURON. I thank my office mate Dori Luli for her friendship and moral support. I also thank Sarah Blum-Sheller and her family for all the help. I thank my husband Jakob Bilger for always believing in me, his support and love, I could not have done it without him. Many thanks to my family; especially to my parents for everything they have done for me and to my parents in law for all their support.

TABLE OF CONTENTS

LIST OF FIGURES

Figure Page

LIST OF TABLES

LIST OF ABBREVATIONS

Abbrevation	Description
AP	Action potential
CV	Coefficient of variation
f-I curve	Frequency-current relationship
IQR	Interquartile range
ISI	Interspike interval
K^+	Potassium ion
MN	Motoneuron
Na^+	Sodium ion
PRC	Phase response curve
SD	Standard deviation
SIZ	Spike initiating zone
SNIC	Saddle node on invariant cycle

LIST OF SYMBOLS

Symbol	Units	Description
$A_{i,\,j}$	-	Voltage attenuation from location i to j.
k_B	$\mathrm{J\,K^{-1}}$	Boltzmann constant ($\approx 1.380\,658\,2 \times 10^{-23}\,\mathrm{J/K}$).
C_m	$\mu\mathrm{F/cm^2}$	Membrane capacitance per unit area.
c_m	nF	Membrane capacitance.
d_b, d_p	μm	Diameter of the branches, primary neurite.
e	C	Elementary charge ($\approx 1.602\,177\,33 \times 10^{-19}\,\mathrm{C}$).
$\triangle G$	J	Change in Gibbs free energy.
γ^b, γ^h	-	Relative position of the energy barrier for gating particle in the membrane for the Shab activation gate b, for the DmNa_v inactivation gate h.
g_i	μS	Conductance of channel type i.
$\overline{g}_L$, $\overline{g}_{Na}$, $\overline{g}_{sb}$	μS	Maximal conductance of leak channels, DmNa_v channels, Shab channels.
$\overline{g}_{syn}$	μS	Maximal conductance of a synapse.
$\widetilde{g}_L$, $\widetilde{g}_{sb}$	μS	Ratio of the maximal conductance of leak and DmNa_v channels, Shab and DmNa_v channels.
I_{app}	nA	Applied current.
I_{Na}, I_{sb}	nA	Ionic current mediated by DmNa_v channels, Shab channels.
I_{ion_B}, I_{ion_P}	-	Sum of voltage dependent ion currents at the branches, at the primary neurite.
I_{PB}	nA	Longitudinal current between primary neurite and branches.
λ_b, λ_p	mm	Length constant of the branches, of the primary neurite without branches.
L_x, L_z	-	Normalized length of the primary neurite, of the branches.
l_b, l_p	μm	Length of the branches, of the primary neurite.
m_∞	-	Steady state fraction of open DmNa_v activation gates.

Symbol	Units	Description
$\overline{N}$	μm^{-1}	Number of branches per physical length.
$\overline{n}$	-	Number of branches per unit electrotonic length.
R_a	Ωcm	Axial resistance per unit area.
$\alpha(V)$	ms^{-1}	Forward rate constant for the conformational change of a gating particle, resulting in the open state .
α_0	ms^{-1}	Frequency factor of the rate constant α.
$\beta(V)$	ms^{-1}	Backward rate constant for the conformational change of a gating particle, resulting in the closed state .
β_0	ms^{-1}	Frequency factor of the rate constant β.
r^b, r^h, r^m	ms^{-1}	Rate of activation for the Shab activation gate b, for the $DmNa_v$ inactivation gate h, for the Shab activation gate b.
R_{in}	$M\Omega$	Input resistance.
$R_{B\infty}$, $R_{P\infty}$	$M\Omega$	Input resistance of a semi-infinite branch, of a semi-infinite primary neurite without branches.
R_m	Ωcm^2	Membrane resistance per unit area.
R_{PB}	$M\Omega$	Ohmic resistance between primary neurite and branches.
τ_{decay}, τ_{rise}, τ_m	ms	Time constant of the decay of a post synaptic current, of the rise of a post synaptic current, of V_m.
T	K	Temperature.
V_m	mV	Membrane potential.
V_{cl}	mV	Voltage clamp potential.
V_H^b, V_H^h, V_H^m	mV	Half activation voltage for Shab activation gates b, for $DmNa_v$ inactivation gates h, for $DmNa_v$ activation gates m.
V_m	mV	Membrane potential in point model.
V_{syn}, V_K, V_L, V_{Na}	μS	Reversal potential of a postsynaptic current, K^+ current, leak current, Na^+ current.
z^b, z^h, z^m	-	Gating charge of the Shab activation gates b, the $DmNa_v$ inactivation gate h, the $DmNa_v$ activation gates m

CHAPTER 1

INTRODUCTION

How does dendritic morphology in combination with different spatial distributions of ion channels influence cell behavior? As Andrew Huxley noted in his Nobel Lecture in 1963: "Very often my expectations turned out to be wrong and an important lesson I learned from these manual computations was the complete inadequacy of one's intuition in trying to deal with a system of this degree of complexity." Here, we create mathematical models, based on experimental data from the fruitfly *Drosophila melanogaster*, in order to conduct a computational study aimed to investigate how changes of different parameters in physiological ranges influence the input-output properties of neurons. Overall, the goal of this project is to tackle the question of how the monopolar structure of neurons, common in invertebrates, influences electrical signaling in combination with spatially nonuniform voltage dependent membrane conductances.

Despite the increasing importance of *Drosophila* as a model system for investigating the molecular mechanisms underlying dendritic development and morphology (reviewed in Corty et al., 2009), neural circuitry, and electrophysiology (reviewed in Baines and Pym, 2006), few computational models of their ion channels have been developed and little is known about the propagation of electrical signals in this system. A major disadvantage of using *Drosophila* arises from its small size, which compromises experimental accessibility. Further, due to the monopolar structure of many invertebrate neurons, the spike initiating zone (SIZ) is usually assumed to be distant from the soma, and the exact location is usually not known. This is particularly problematic for the interpretation of electrophysiological data, which are obtained by recordings from the soma. The use of computational modeling techniques can help predict the behavior of membrane dynamics at experimentally inaccessible locations and help connect electrophysiological and other molecular biological findings to neuronal function.

The main function of neurons is to decode information obtained via synaptic input and compute the appropriate output, usually encoded by means of action potentials (APs). In order to understand how these computations are carried out, it is critical to understand how input integration depends on the electrotonic properties of the dendritic tree as well as how and where the APs are initiated. Both aspects depend on the dynamical properties of the transmembrane potential, which in turn is determined by the geometry of the cell and the ion channel kinetics, distribution, and density. In various vertebrate neurons computational studies have been applied successfully to gain insights into these complex relationships.

In this work we focus on the identified *Drosophila* motoneuron 5 (MN5) since its morphology, electrophysiology and certain aspects of its behavior during fight have been well characterized experimentally. Our computational modeling approach includes morphologically realistic multicompartment models and spatially reduced mathematical models and is based on biophysically motivated assumptions. Initially we consider the contributions of cell structure to dynamical behavior separately from the contributions of nonlinear ion channel kinetics. These parallel modeling studies provide a basis for quantifying and analyzing the specific impact of both on model behavior. Exploration of the parameter space in order to understand the impact of changes in parameters is important due to the inherent variability of biological systems.

1.1 Background and Significance

Computations performed by the nervous system depend on a properly tuned interplay of network properties such as connectivity and synaptic strength and the intrinsic properties of single neurons; thus it is critical to understand the computation of single neurons. The development of neurons is determined and influenced by global and local

cues, resulting in an overwhelming variety of distinct morphologies with different membrane properties. Diverse patterns of protein expression lead to different ion channel combinations, which are furthermore not uniformly distributed over the entire plasma membrane but targeted to and expressed at specific locations (Nusser, 2009). This results in different types of neurons with distinct functions.

Drosophila and other invertebrates provide valuable model systems for investigating neuronal development (Corty et al., 2009), ion channel kinetics, and their impact on firing properties. Many invertebrate neurons can be identified individually, and often molecular mechanisms are comparable to those in vertebrate systems. The spiking responses and neuronal morphology in these neurons have been investigated at different developmental stages (Choi et al., 2004) and changes in these properties have been observed during development (Duch and Levine, 2000), after targeted genetic manipulations, and under different pharmacological conditions (Peng and Wu, 2007; Duch et al., 2008; Ryglewski and Duch, 2009). In particular, the use of *Drosophila* in research is of great interest due to the development of new genetic tools for experimentation. However, the impact of structural properties of neurons and specific ion channel kinetics on neuronal function remains largely unclear. Computational methods have proven useful for providing insights into the interplay of channel dynamics, dendritic structure, and synaptic locations in vertebrates (Mainen and Sejnowski, 1996; Segev and London, 2000), and modelling allows for an examination of the impact of parameters that are not experimentally separable and for generating predictions about experimentally inaccessible locations.

Ultimately, neuronal function is determined by the transmission and propagation of information via APs, where input information is encoded in a digital code. Characteristics of a neuron's spiking behavior depend on conditions given by its environment (e.g. an

isolated cell versus one embedded in a network). However, different neurons also exhibit distinct characteristic features under standardized or similar conditions such as constant current injection (Shepherd, 2004). Hodgkin classified neurons according to their spiking behavior upon steady current injection, and the resulting frequency-current relationship (f-I curve) generally can be divided into three distinct classes (Hodgkin, 1948). Numerous subsequent studies have analyzed the relationship between this classification and the output properties of a model neuron (Rinzel and Ermentrout, 1989; Ermentrout, 1996; Gutkin et al., 2003; St-Hilaire and Longtin, 2004; Tateno and Robinson, 2007; Tateno and Robinson, 2006; Tateno et al., 2004) and, from a dynamical systems point of view, how this classification relates to the underlying mathematical structure of the model (Izhikevich, 2007; Prescott et al., 2008).

1.1.1 Diversity of Ion Channels and Impact on Neuronal Dynamics

The generation of action potentials, their shape and firing patterns depend in large part on voltage gated sodium (Na^+) and potassium (K^+) channels. Experimental and theoretical studies show that differences in spiking patterns can be related to different combinations of ion channel densities (Goldman et al., 2001; Zeberg et al., 2010) with different channel kinetics. These differences affect the timing of APs, influence subthreshold integration of synaptic input and the filtering properties of the neuronal structure, resulting in bandpass or highpass filtering properties. Consequently, the response of a neuron to synaptic input will depend on the underlying dynamics. Therefore, in order to study the functional relevance of synaptic distributions and temporal properties, it is necessary to either have a good understanding of the dynamical properties of the neuron in question or to explore a broad parameter space via numerical studies.

Drosophila has only one confirmed Na^+ channel gene $DmNa_v$ (Miyazaki et al., 1996; Mee et al., 2004), which is subject to alternative splicing. The voltage dependency of the macroscopic currents carried by the different splice variants have been characterized in heterologous expression systems using voltage clamp recordings (Olson et al., 2008; Lin et al., 2009). K^+ channels show the greatest diversity among ion channels (Coetzee et al., 1999; Jan et al., 1977), where voltage gated ion channels fall roughly into two categories, the non-inactivating or slowly inactivating delayed rectifier and the rapidly inactivating, transient A-type currents (Hille, 1992). In *Drosophila* neurons two genes, *Shab* and *Shaw*, encode delayed rectifier current conducting channels. Shab and Shaw channels are members of the K_v2 and K_v3 subfamilies, respectively (Wei et al., 1990; Covarrubias et al., 1991; Tsunoda and Salkoff, 1995a; Tsunoda and Salkoff, 1995b). Since Shaw channels show a very low voltage sensitivity, it is suggested to operate rather as a leak channel, while Shab conducts the majority of delayed rectifier currents (Tsunoda and Salkoff, 1995b). The kinetics of the Shab channel are reported to be comparable to the classical (as described by Hodgkin-Huxley) delayed rectifier K^+ channel (Tsunoda and Salkoff, 1995b). Two further genes encode channels conducting A-type currents, that show fast inactivation kinetics. Activation and inactivation properties of *Drosophila* voltage gated K^+ channels have been characterized in homologous expression systems as well as in *Drosophila* neurons (Covarrubias et al., 1991; Gasque et al., 2005; Islas and Sigworth, 1999; Tsunoda and Salkoff, 1995b). Their contributions on firing properties have been studied using pharmacology and genetical manipulations in order to remove the currents (Choi et al., 2004; Peng and Wu, 2007; Gasque et al., 2005; Ryglewski and Duch, 2009; Ping et al., 2011). Comparing different mutant neurons indicates that Shab is required for repetitive spiking, while A-type channels regulate the firing frequency and lower the spike threshold, to induce a delay to first spike (Choi et al., 2004; Ping et al., 2011).

1.1.2 Influence of Neuronal Structure

The integration of synaptic inputs depends on spatial and temporal interaction and the attenuation of the resulting membrane potential changes. Therefore, the processing of synaptic input depends on the location of the input sites relative to each other, the structure of the dendritic tree, and the membrane properties (Koch and Segev, 2000; Häusser and Mel, 2003; London and Häusser, 2005; Katz et al., 2009). It is widely accepted that even passive dendritic structures have an impact on signal integration, propagation and firing properties (Crook et al., 1998; Lewis and Rinzel, 2004; Schwemmer and Lewis, 2011). Using cable theory Rall (1962; 1964) provided the theoretical basis to explain, understand, and analyze the electrotonus in dendrites by using cable theory. The presence of voltage dependent ion channels increases its impact further, and the nonuniform distribution of ion channel densities and compositions can lead to variations in membrane behavior at different locations in the cell. For example in both invertebrate and vertebrate neurons, Shaker and members of the K_v1 subfamily are predominately found in axonal regions (Rogero et al., 1997; Jan and Jan, 1997; Lee et al., 2008; Ueda and Wu, 2006), whereas for Shal/K_v4 a somato-dendritic targeting has been shown (Diao et al., 2010; Chen et al., 2006; Johnston et al., 2000). Computational studies incorporating passive as well as active dendritic structures suggest that the spatial organization of the dendrite influences the dynamical properties and signal encoding of a neuron, leading to qualitatively different input-output behavior (Mainen and Sejnowski, 1996; Kirst et al., 2008; Goldberg et al., 2007; Elburg and Ooyen, 2010).

1.1.3 Variability

Accessing the specific role of different ion channels and neuronal structure is challenged by the considerable amount of variability from animal to animal. Furthermore,

compensation mechanisms and modulation adjust the membrane properties of neurons (Marder, 2011). In a recent review article Marder (2011) pointed out that these findings indicate the need "to measure as many system components as possible within an individual" and that fitting and combining independently obtained and averaged experimental data is unlikely to reproduce realistic model behaviour. Especially in the small *Drosophila*, it is hard to measure a variety of system parameters simultaneously. For this reason, it is necessary to explore the interactions emerging from changes in parameters in models to understand the impact of variations. Computational models allow for the assessment of the influence of individual parameters on neuronal dynamics independently and systematically.

1.1.4 *Drosophila* Motoneuron 5

In this work we focus on *Drosophila* MN5, which is one of five MNs that innervate the dorsolongitudinal flight muscles. During flight, MN5 discharges tonically with frequencies between ∼5 and 20 Hz (Koenig and Ikeda, 1980b; Koenig and Ikeda, 1980a), where firing frequency is linearly correlated with wing beat frequency and intramuscular calcium concentration (Gordon and Dickinson, 2006). Furthermore, it is suggested that low firing frequency is an inherent property of the neurons (Harcombe and Wyman, 1977).

MN5 has been used to study the relationship between neuronal function, dendritic morphology, and ion channel expression. Using the genetic power of *Drosophila*, which allows targeted manipulations of ion channel expression and proteins relevant for dendritic development, the impact of these factors has been related to functional relevance and activity-dependent dendritic growth (Duch et al., 2008). The electrophysiological

activity and ion channel kinetics have been recorded *in situ* with somatic patch clamp experiments (Duch et al., 2008; Ryglewski and Duch, 2009). The dendritic shape has been reconstructed and analyzed quantitatively (Vonhoff and Duch, 2010), and putative synaptic and Na^+ channel locations have been investigated (Kühn and Duch, 2013). Interestingly, in contrast to many invertebrate neurons, large action potentials can be recorded at the soma (Duch et al., 2008; Fayyazuddin et al., 2006).

Here we use a computational approach to investigate the impact of voltage gated ion channel distributions and kinetics on spike initiation, and we also study the effects of different locations of the SIZ in monopolar neurons on input integration and backpropagation of APs. Particularly for monopolar neurons, questions arise concerning to what extent the response to current stimulation depends on input location and how much information about neuronal function is available from recordings carried out at the soma when it is far from the SIZ. With the entire dendritic structure lying between the stimulus location and the SIZ, the resolution of the membrane dynamics in terms of subthreshold behavior at the location where the spikes are generated is limited. Additionally these recording conditions may influence the state of the entire neuron compared to the natural condition of synaptic input at dendritic locations and thus the response at the SIZ. With computational models, the response to synaptic input and current injection can be compared under different conditions, aiding the interpretation of electrophysiological recordings and stimulations at a single location and providing insight into input integration and processing mechanisms in monopolar neurons.

CHAPTER 2

POINT MODEL

2.1 Introduction

Drosophila MN5 shows considerable animal to animal variation in spiking behaviors upon current injection (Duch et al., 2008), ranging from non-repetitive responses (single spikes or single graded responses) to repetitive spiking with different f-I curves and varying delays to first spike. APs are generated due to voltage dependent ion channels. The dynamics of a patch of excitable membrane can be described mathematically with a set of ordinary differential equations. The best known model is due to Hodgkin and Huxley (1952), in which the membrane is modeled as a parallel electrical circuit consisting of a capacitor representing the lipid bilayer and conductances representing ion channels. The voltage dependent change in permeability of ion channels is described using conductance changes. Dynamical systems theory provides well suited tools for examining the behavior of such models. In models of excitable membranes, these different spiking dynamics can be related to different underlying bifurcation structures of the dynamical system (Izhikevich, 2007).

Transmembrane potential dynamics depend on diverse interacting nonlinear processes resulting from different kinetics of ion channels. Recent experimental studies suggest differential contributions for membrane excitability of K^+ currents conducted by Shab, Shal and Shaker channels (Gasque et al., 2005; Peng and Wu, 2007; Ping et al., 2011). Furthermore, it is known that regenerative currents like the persistent Na^+ and A-type K^+ current support aggregator properties connected to saddle node on invariant cycle (SNIC) bifurcations, the type I phase response curves (PRCs), and class I f-I curves. On the other hand, for example the delayed rectifier K^+ current evokes resonator properties associated with a Hopf bifurcation, type II PRCs, and the class II f-I curves (Hutcheon and Yarom, 2000; Ermentrout et al., 2001). However, the specific function of an ionic current

may depend on the properties of other currents and the modulatory state. Furthermore, experimental studies using genetic knock downs can be compromised by homeostatic regulation mechanisms (Marder and Goaillard, 2006), while pharmacological manipulations may suffer from low specificity of drugs (Greenwood and Leblanc, 2007).This can potentially lead to conclusions about the role of a certain ion channel that is not specific to that channel. The use of computational models can help resolve these issues, by allowing for controlled and independent variation of specific parameters.

To examine the function of specific ion channels, we begin with a mathematically reduced, two dimensional model of a patch of excitable membrane comprising two types of voltage gated ion channels. We develop models of Na^+ and K^+ voltage gated ion channels displaying kinetics based on channels expressed in *Drosophila*. The Na^+ channel is based on kinetics of $DmNa_V29$, which mediates a fast inward current, and the K^+ channel is based on kinetics of Shab, which mediates a delayed rectifier outward current.

If a dynamical system exhibits a qualitative change in its dynamics as parameters are varied, it is called a bifurcation. Typical changes include a change in the number or stability of fixed points or periodic orbits. When a model neuron transitions into repetitive firing in response to constant current injection, it indicates that the system undergoes a bifurcation. Yet it could be that the periodic orbit already existed and the stable fixed point still exists when current is injected, but the system was pushed on a trajectory in the basin of attraction of the limit cycle due to the perturbation. In this case the neuron is bistable and no bifurcation occurred. Furthermore, different types of a stable fixed points cause a different behavior of trajectories in its neighborhood. Similarly, different bifurcations impose certain characteristics on the behavior of the system. Bifurcation theory and phase plane analysis provide tools to analyze the bifurcations a dynamical system exhibits. Usually, in models of excitable membranes, a stable fixed point can either lose

stability via a Hopf bifurcation or disappear via a saddle-node bifurcation. In addition to fixed points, models of repetitively spiking neurons are expected to have stable limit cycles attractors for some range of applied current (I_{app}). Stable limit cycles can appear via four codimension one bifurcations: a fold limit cycle bifurcation, SNIC, a homoclinic orbit bifurcation, or a supercritical Hopf bifurcation (Guckenheimer and Holmes, 1983).

Here we ask whether changing the density of Shab channels is sufficient to switch between bifurcation types, whether this can cause the different observed response properties, and whether these suggest qualitatively different responses to synaptic input. It is important to investigate this question in order to understand the specific functions of other voltage gated ion channels. For example, in order to pinpoint the specific functions of A-type K^+ channels, which has been attempted in experimental as well as theoretical studies (Herrera-Valdez et al., 2010; Herrera-Valdez et al., 2009), it is necessary to understand what electrical properties can be generated in a minimal biologically realistic system. Some initial modeling studies were performed with Marco Herrera-Valdez (Herrera-Valdez et al., 2010; Herrera-Valdez et al., 2009; Herrera-Valdez et al., 2012). However, all studies described here were performed independently.

2.2 Methods

2.2.1 Model of Excitable Membrane

Membrane dynamics are described with a Hodgkin-Huxley type conductance based model (Hodgkin and Huxley, 1952), which uses a set of ordinary differential equations to model the current balance equation and the channel gating. According to Kirchhoff's law, the total current through the membrane is the sum of the capacitive current and

ionic currents mediated by the different channel types (indexed by i here), so that the current balance equation takes the form

$$c_m \frac{dV_m(t)}{dt} = -\sum_i I_i + I_{app}. \tag{1}$$

The ionic currents are modeled according to Ohm's law:

$$I_i = g_i(V_m - V_i), \tag{2}$$

where g_i is the voltage dependent conductance and V_i is the reversal potential of channel i. V_i arises from the reversal potential of the ions the channel is permeable for. In Herrera-Valdez et al. (2012), the equations for the currents were derived using an approach from Endresen et al. (2000) based on a combination of Ohm's and Fick's law such that, if considering channels permeable for only one type of ion,

$$\check{I}_i = A_i \sinh\left(\frac{z_{ion}e}{k_B T}(V_m - V_i)\right), \tag{3}$$

where z_{ion} is the valence of the ion that channel i is permeable for. However, the description of the electromotive force based on Ohms's law usually provides good fits to electrophysiological data and is used in many modeling studies. Incorporation of a spatial component and analysis of the passive properties will require the linear version at least for the passive portion of the model, which motivates our approach.

The channel conductance is modeled as the product of the maximal conductance and voltage dependent gating variables. The general formulation includes a gating variable to represent activation and one to represent inactivation Each gating variable is associated with a open probabilities p and q, respectively and a number of independently operating gates j and k, respectively; such that

$$g_i = \overline{g}_i p_i^j q_i^k. \tag{4}$$

The open probability of a gate p can be described with

$$\frac{dp}{dt} = \alpha(V)(1-p) - \beta(V)p, \tag{5}$$

where $\alpha(V)$ is the opening rate acting on the fraction of gates in the closed state (p-1) and $\beta(V)$ is the closing rate acting on the fraction of gates in the open state p. This can be rewritten as

$$\frac{dp}{dt} = \frac{p_\infty(V_m) - p}{\tau^p(V_m)}, \tag{6}$$

by setting

$$p_\infty(V_m) = \frac{1}{1+\frac{\beta(V)}{\alpha(V)}} \text{ and } \tau^p(V_m) = \frac{1}{\alpha(V)+\beta(V)}. \tag{7}$$

The rate functions are modeled by assuming that charged particles move across the membrane in response to an electric field, resulting in opening or closing of a gate. According to the Arrhenius expression for rate constants, the rate functions should be of the form

$$\alpha(V) = \alpha_0 \exp\left(-\frac{\Delta G(V_m)}{k_B T}\right) \text{ and } \beta(V) = \beta_0 \exp\left(-\frac{\Delta G(V_m)}{k_B T}\right), \tag{8}$$

where ΔG (V_m) is the voltage dependent difference in free energy between the two states. First order approximation of the free energy barrier and the assumption that the transition consists of the movement of charged particles across the membrane in response to an electric field results in

$$\alpha(V) = \alpha_0 \exp\left(\frac{-z^p e \gamma^p V_m}{k_B T}\right) \text{ and } \beta(V) = \beta_0 \exp\left(\frac{z^p e(1-\gamma^p) V_m}{k_B T}\right), \tag{9}$$

where k_B is the Boltzmann constant, α_0 and β_0 are constant frequency factors. $z^p e$ is the gating charge, where e is the elementary charge and z^p reflects the amount and distance the gating particle is moved. Setting

$$\frac{\beta_0}{\alpha_0} = \exp\left(V_H^p \frac{z^p e}{k_B T}\right) \text{ and } r^p = {\alpha_0}^{1-\gamma^p} {\beta_0}^{\gamma^p}, \tag{10}$$

Eqs. (7) become

$$p_\infty(V_m) = \frac{1}{1+\exp\left(\frac{-z^p e(V_m - V_H^p)}{k_B T}\right)} \text{ and } \tau^p(V_m) = \frac{\exp\left(\frac{-\gamma^p z^p e(V_m - V_H^p)}{k_B T}\right)}{r^p\left(1+\exp\left(\frac{z^p e(V_m - V_H^p)}{k_B T}\right)\right)}. \quad (11)$$

2.2.2 Ion Channels Models

The intrinsic dynamics of the membrane potential are determined by one Na^+, one K^+ and one leak current. The K^+ current (I_{sb}) is a delayed rectifier current and is based on kinetics reported for Shab channels, where we neglect the slow inactivation of those channels. The voltage dependence of the Na^+ current (I_{Na}) is based on currents mediated by channels encoded by the splice variant $DmNa_v29$, which is among others expressed in adult *Drosophila* neurons. The fast activation is assumed to be at steady state and the inactivation kinetics are similar to the activation kinetics of Shab channel gates (Rinzel, 1985; Av-Ron et al., 1991). This reduces the model to a two dimensional system and allows for phase plane analysis. The maximal conductances are then adjusted in order to resemble the response properties observed in *Drosophila* MN5 and to analyze the corresponding bifurcation structure. The membrane currents for Na^+ and K^+ and the leak current take the form

$$I_{Na} = \overline{g}_{Na} m_\infty{}^4 (1-n)(V_m - V_{Na}), \quad (12)$$

$$I_{sb} = \overline{g}_{sb} n^3 (V_m - V_K), \quad (13)$$

$$I_{Leak} = \overline{g}_L (V_m - V_L). \quad (14)$$

I_{Leak} accounts for currents with a relative small voltage dependence.

Voltage clamp recordings are used to constrain the parameters. When the voltage is held constant at V_{cl} , the solution to Eq. (6) is

$$p(t) = p_\infty(V_{cl}) + \left(p_0 - p_\infty(V_{cl})\right)\exp\left(\frac{-t}{\tau^p(V_{cl})}\right); \quad (15)$$

therefore, the membrane current mediated by a channel denoted by the index i becomes

$$I_i = \overline{g}_i \left(p_\infty(V_{cl}) + (p_0 - p_\infty(V_{cl})) \exp\left(\frac{-t}{\tau^p(V_{cl})}\right)\right)^j \left(q_\infty(V_{cl}) + (q_0 - q_\infty(V_{cl})) \exp\left(\frac{-t}{\tau^q(V_{cl})}\right)\right)^k (V_m - V_i). \quad (16)$$

The parameters for I_{sb} were obtained using voltage clamp recordings from *Drosophila* embryonal cell cultures (Tsunoda and Salkoff, 1995b). Cells were clamped to a holding potential of −50 mV, and the current in response to step potentials from −20 to 50 mV in 10 mV increments was recorded. The pre-step potential is assumed to be sufficiently low so that essentially all inactivation gates are open and all activation gates are closed. The duration of the pre-step is assumed to be long enough that the system is at steady state. The published traces were digitized and fitted simultaneously to Eq. (16) using a nonlinear least-squares optimization algorithm.

To constrain the Na^+ channel kinetics, Boltzmann equations with parameters that describe the activation and inactivation curves as reported by Olson et al. (2008) were used. The activation curve was obtained by clamping the cell at a holding potential of −120 mV and recording the current in response to step potentials from −120 to 60 mV in 5 mV increments. The peak currents for each step potential are divided by $(V - V_{Na})$ to obtain the peak conductance. The peak conductance as a function of voltage steps was fit with a Boltzmann equation. We fit the resulting curve with Eq. (16) to obtain a model for the $DmNa_V29$ activation gates. Recall, that parameters for the inactivation gates are the same as the parameters for the activation gate of Shab channels. The steady state inactivation curve was used to subsequently incorporate independent Na^+ inactivation. Olson et al. (2008) obtained this curve using pre-steps from −120 to 40 mV followed by a step potential of −5 mV. The peak current of each trace is divided by the maximal peak current among all steps, which is the one in response to the most hyperpolarized pre-step

and assumed to be the current amplitude, given all channels are in the open state. The normalized peak current as a function of voltage steps was fit with a Boltzmann equation. As before, the resulting curve is fitted with Eq. (16), yielding a model for the $DmNa_V29$ inactivation gate.

2.2.3 Software

Bifurcation diagrams were generated with numerical continuation methods, using PyCont a sub-package of PyDSTool (Clewley et al., 2007), which provides an interface to AUTO (Doedel et al., 2002). PRCs were calculated with the adjoint method implemented in PyDSTool. Stable and unstable manifolds for saddle points are obtained using XPPAUT (Ermentrout, 2002). The phase responses were determined by calculating the system's adjoint (Ermentrout and Kopell, 1991) using PyDSTool. Numerical simulations were performed using Python 2.7. The systems of ordinary differential equations are integrated using odeint from the scipy package, which uses lsoda from the FORTRAN odepac.

2.3 Results

2.3.1 Fitting of Ion Channel Models

To obtain models for Shab channels, traces from voltage clamp recordings (Tsunoda and Salkoff, 1995b) are fit with Eq. (16). The number of gates are usually chosen to best represent the experimentally measured ion current dynamics. Since the inactivation of Shab channels is small, we set the number of inactivation gates to zero. For the activation we use a power of one as in Herrera-Valdez et al. (2012), as well as, a power of four as used by Hodgkin and Huxley (1952). Both numbers provide fits that are in good agreement with the voltage clamp recordings of Shab currents (Fig. 2.1A). The values of the different

Table 2.1 Parameter sets for I_{sb}. Comparison of published values, fits of digitized experimental data with Eq. (16), and hand tuned parameters.

name	description	V_H^b [mV]	z^b	r^b [ms^{-1}]	γ^b	# of gates
sb_{pup}	published data [(1)]	-1.05 ± 1.20	1.59 ± 0.10	–	–	1
sb_1	fits with power of one	2.20	1.51	0.14	0.46	1
sb_4	fits with power of four	-39.3	0.94	0.17	0.49	4
sb_{def}	hand tuned from sb_4	-42.1	1.10	0.20	0.38	4
sb_z	fits with power of four and fixed z^b	-28.1	1.50	0.26	0.30	4

[(1)] Tsunoda and Salkoff (1995)

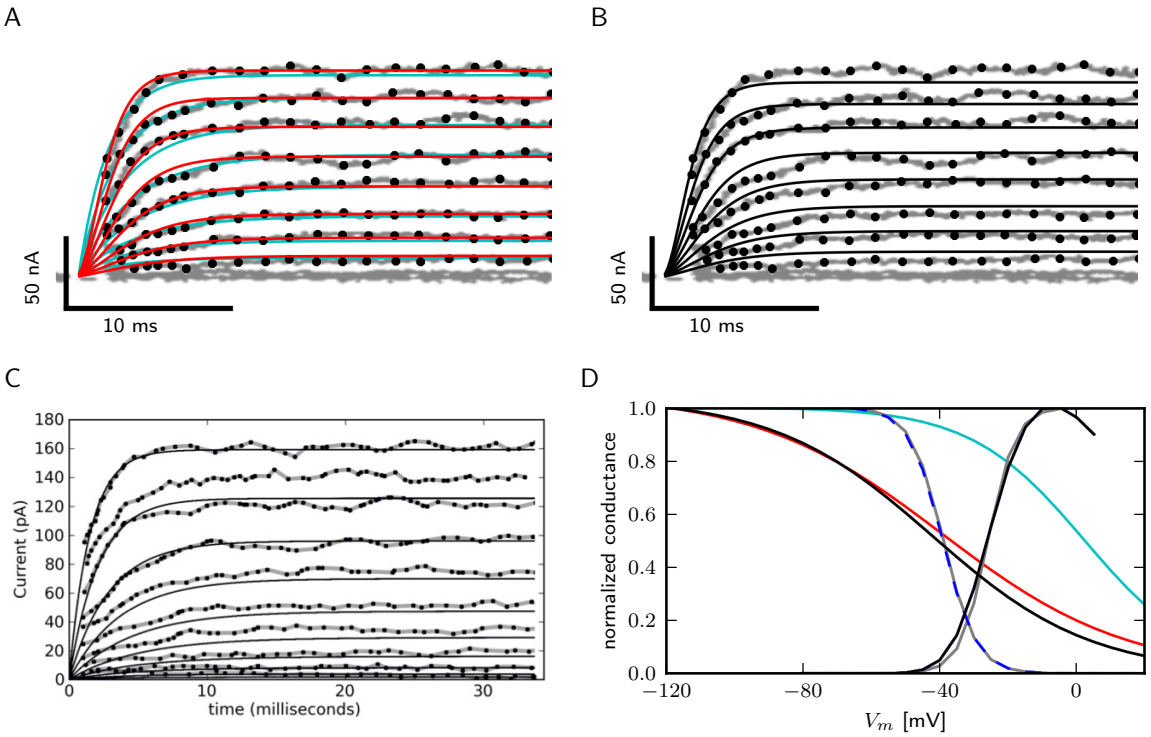

Figure 2.1 Data fits of Shab and DmNa$_v$29 channel parameters. A,B : Fig.4A from Tsunoda and Salkoff (1995) is shown in gray. A-C: digitized points from the published traces are marked as black circles. Model of Shab channels with parameters obtained from fits (A) with power one (sb_1, red) and power four (sb_4, cyan) and hand tuned parameters (sb_{def}, B, black). C: Fig.7 from Herrera-Valdez et al. (2012). D: Steady state activation and inactivation curves of DmNa$_v$29 according to Olson et al. (2008) (gray) and from models (note that the activation kinetics are the same in all models). Results using parameter sets sb_1, sb_4, sb_{def} indicated by red, cyan and black lines, respectively). Independent inactivation used in the three dimensional model is shown with dashed blue lines.

Table 2.2 Parameters for I_{Na}. Comparison of published values that where derived from fits of voltage clamp data with Boltzmann curves and values used in the models.

			published experimental data		model parameter	
			Olson et al. (2008)	Lin et al. (2009)	model 2D	model 3D
activation	V_H^m	[mV]	−25.9±1.2	−27.3±1.3	−33.00	−33.00
	k^m	[mV]	4.0±0.3	–	8.50	8.50
	z^m		–	–	3.00	3.00
	r^m	[ms^{-1}]	–	–	∞	∞
	power		1	1	3	3
inactivation	V_H^h	[mV]	−38.9±0.3	−48.1±1.3	−42.14	−39.14
	k^h	[mV]	4.8±0.1	–	≈ 23.07	≈ 4.91
	z^h		–	–	1.11	5.20
	r^h	[ms^{-1}]	–	–	0.20	0.15
	γ^h		–	–	0.38	0.38
	power		1	1	1	1

parameter sets are summarized in Tab. 2.1. In Eq. (16) the electromotive force is based only on Ohms's law, as it is commonly described in Hodgkin-Huxley type conductance based models and displays a linear current-voltage relationship. The model appears to resemble the data better than the electro-diffusion version of Herrera-Valdez et al. (2012; Fig. 2.1C). We do not examine, whether this is due to differences in the description of the current-voltage relationship or simply a result of the different parameter for the gating equations. However, it is likely that the differences are primarily caused by the different parameter (Herrera-Valdez, 2012).

For Na^+ channels only the parameters for Boltzmann curves used to fit the peak and tail currents from voltage clamp experiments were available (Olson et al., 2008). Therefore only z^m, z^h, V_H^m and V_H^h can be assessed. The inactivation curve for I_{Na} can be best represented using a power of four for the Shab channels (Tab. 2.1, Fig. 2.1D), because the half activation of a single gate is close to the value reported for $DmNa_v29$ (Tab. 2.2). The half inactivation values for other $DmNa_v$ splice variants are between −34.9 and −66.4 mV (Olson et al., 2008; Lin et al., 2009). None of the reported splice variants has a half inac-

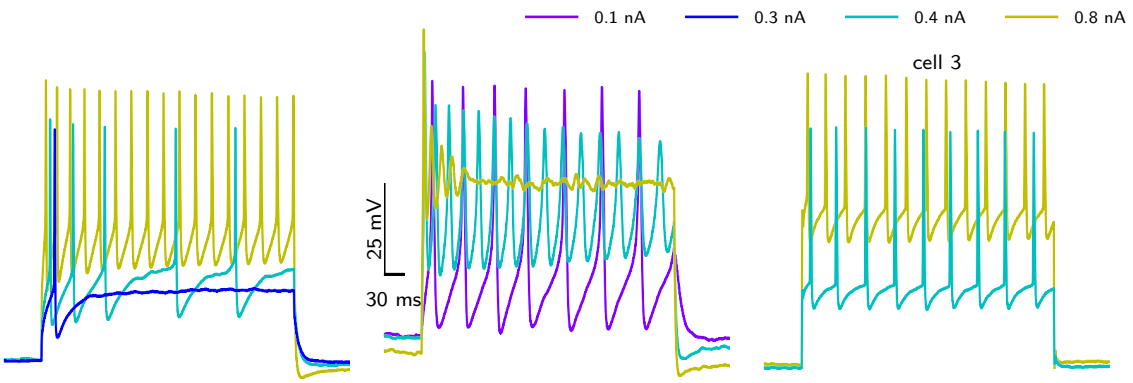

Figure 2.2 Different firing behaviors from three *Drosophila* MN5s. Recordings were made by S. Ryglewski.

tivation that is close to the value found for Shab channel activation using a power of one. However, the slope of the resulting inactivation curve for I_{Na} is too flat, indicating that the gating charge z^b is too small. The Shab channel kinetics were adjusted by hand in an attempt to improve z^b, leading to parameter set sb_{def}. Only a slight improvement could be achieved without compromising the Shab kinetics (Fig. 2.1B). Therefore, subsequent to the analyzes of the two dimensional model, we extend the model to a three dimensional model including a variable for I_{Na} inactivation. That allows different parameters for Na^+ inactivation and K^+ activation. Adjusting the gating parameter as summarized in Tab. 2.1 leads to a good agreement between model and data (Fig. 2.1D). In the following we use sb_{def} as default parameter set to model Shab channels dynamics.

2.3.2 Experimental Results

Intracellular recordings in whole cell patch configuration carried out by S. Ryglewski reveal substantial animal to animal variation in the responses to current pulses (see also Herrera-Valdez et al., 2012). Out of 52 cells, 38 % exhibit a single action potential for a low-amplitude current stimulation, with repetitive spiking that adapts in frequency for slightly increased stimulation (Fig. 2.2, left). Firing frequency increases with stimulation

amplitude. In 8 % of the 52 recorded cells a very low-amplitude stimulation produces repetitive spiking with a relatively a large duration of single APs (Fig. 2.2, middle). Stimulations with an amplitude that is close to the firing threshold observed in the other cases (0.4 nA) induces a large initial spike with subsequent broader spikes that diminish in amplitude. Increasing the stimulation amplitude further results in dampening oscillations that finalize in a depolarization block. Another common response, seen in 42 % of the 52 recorded cells, is depicted in Fig. 2.2 (right). Repetitive firing is induced by a stimulation amplitude of 0.4 nA, while the cell remains quiescent with stimulation amplitudes of 0.3 nA. Higher stimulus amplitudes result in only a slight increase in firing frequency. In rare cases (4 %), repetitive spiking occurs after a long delay, where the interspike interval (ISI) is smaller than the initial delay (not shown, but see Herrera-Valdez et al., 2012). Higher amplitudes elicit higher frequency spiking without initial delay.

2.3.3 Two Dimensional Membrane Model

2.3.3.1 General Model Behavior

In response to steady current injection, the model resembles the basic features of *Drosophila* MN5 (Fig. 2.3). Current pulses with amplitudes of the same order of magnitude as used in experiments cause the model to fire repetitively. However, compared to the majority of available recordings, the AP duration is too long and the firing frequency is quite high (Fig. 2.3 A). It is likely that these features may be adjusted by adding A-type currents to the model. Shaker current is thought to adjust the spike shape (Peng and Wu, 2007) and Shal is thought to decrease the firing frequency (Tsunoda and Salkoff, 1995a). Yet in some recordings the AP duration is even longer than in the model (Fig. 2.3 B). In contrast to the model from Herrera-Valdez et al. (2012), in this model APs appear on elevated potentials for a wide range of parameters, including the default parameters $s\,b_{def}$

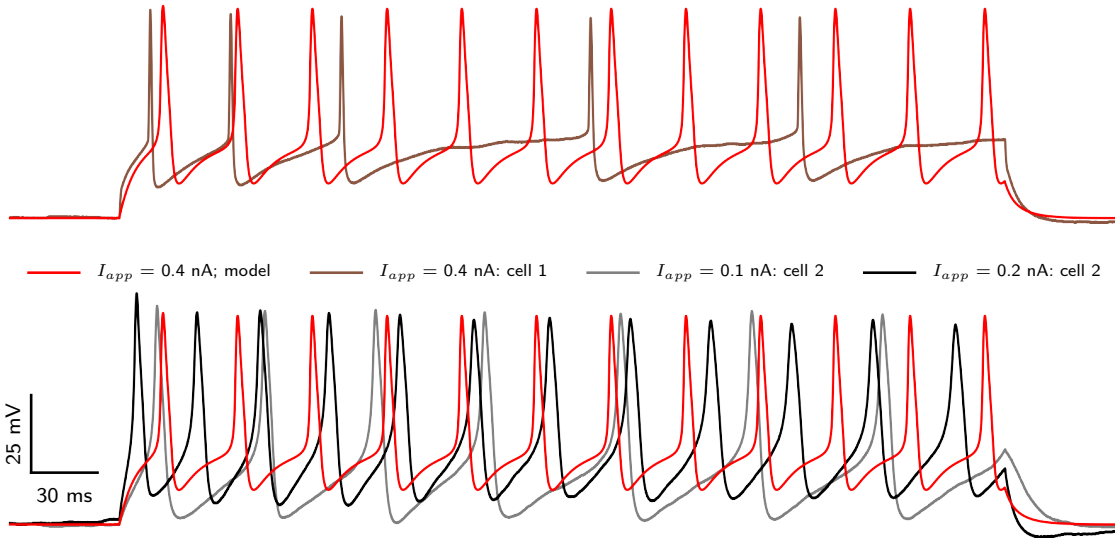

Figure 2.3 Comparison of electrophysiological data and model behavior. Membrane potential in response to squared pulse current injections of different amplitudes in the model and two different cells.

used for the model. This is a consequence of the combination of slightly different values for γ^b, z^b and r^b.

2.3.3.2 Sodium Channel Density

In large part, the density of sodium channels determines the maximal rate of change of the voltage ($^{dV_m}/_{dt}$) during the rising phase of an action potential. A phase-plane plot showing $^{dV_m}/_{dt}$ versus V_m for three different recordings as well as the model is depicted in Fig. 2.4. The maximal $^{dV_m}/_{dt}$ varies among cells and is between 55 and 20 $^{mV}/_{ms}$.

With a $\overline{g}_{Na}$ of 15.62 µS (Fig. 2.4 left, black trace) the maximal $^{dV_m}/_{dt}$ for the model takes a value of 35 $^{mV}/_{ms}$, which is between the observed values. Increasing $\overline{g}_{Na}$ to 20 µS results in a maximal $^{dV_m}/_{dt}$ of about 55 $^{mV}/_{ms}$ during the rising phase, which corresponds to the largest observed values (Fig. 2.4 right). In the following we show results for $\overline{g}_{Na} = 15.62\,\mu S$. However, a model with $\overline{g}_{Na} = 20\,\mu S$ in combination with a smaller $\overline{g}_L$ of 0.01 µS shows qualitatively similar behavior.

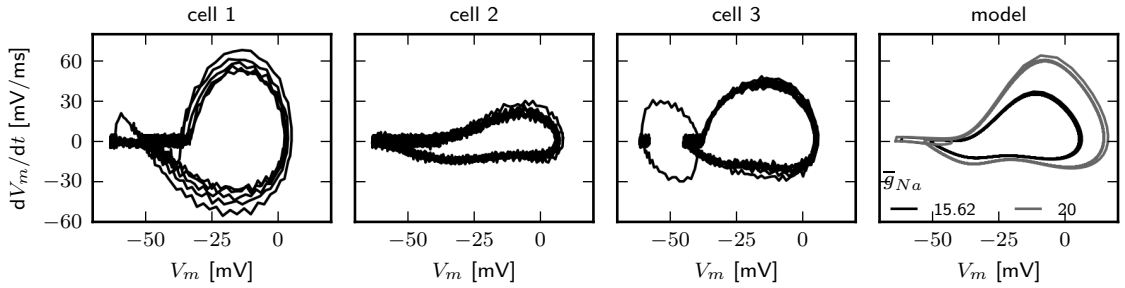

Figure 2.4 Phase plots of electrophysiological recordings and the model in response to squared pulse current injection.

2.3.3.3 Shab Channel Density Determines Bifurcation Type

In the following we keep the maximal conductance of Na^+ channels ($\overline{g}_{Na}$) constant and use the dimensionless ratio $\widetilde{g}_{sb}$ of the maximal conductance of Shab channels ($\overline{g}_{sb}$) and $\overline{g}_{Na}$. This serves as a measure for the Shab channel density, assuming that the maximal conductance is the product of the amount of channels in the membrane and the conductance of a single channel in the open state. We find that changing $\widetilde{g}_{sb}$ results in different bifurcation types as the system undergoes a transition from rest to spiking in response to current injection (Fig. 2.5) where low levels of Shab result in a saddle node bifurcation and high levels in a Hopf bifurcation.

Fig. 2.5B shows the bifurcation diagram for $\widetilde{g}_{sb}$ values of 0.57, 0.6, 0.782 and 1.347. This diagram shows the local stability of the fixed points (black) of the system and indicates Hopf points (blue) and saddle nodes (green). In all cases there are saddles nodes, but for $\widetilde{g}_{sb} = 1.347$ the stability changes via a subcritical Hopf bifurcation at $I_{app} = 0.653\,\text{nA}$. A stable limit cycle emerges at $I_{app} = 0.595\,\text{nA}$, hence a stable fixed point and stable limit cycle coexist. The coexistence of a stable fixed point and a stable limit cycle is also given with $\widetilde{g}_{sb} = 0.782$. Yet, the stability of the fixed point is lost via a saddle node bifurcation at $I_{app} = 0.4037\,\text{nA}$, while the stable limit cycle appears at $I_{app} = 0.3958\,\text{nA}$ via a global fold bifurcation of limit cycles (Fig. 2.5C right panel). Decreasing $\widetilde{g}_{sb}$ further to 0.6, the stable fixed point looses stability at $I_{app} = 0.4037\,\text{nA}$ and a stable limit cycle

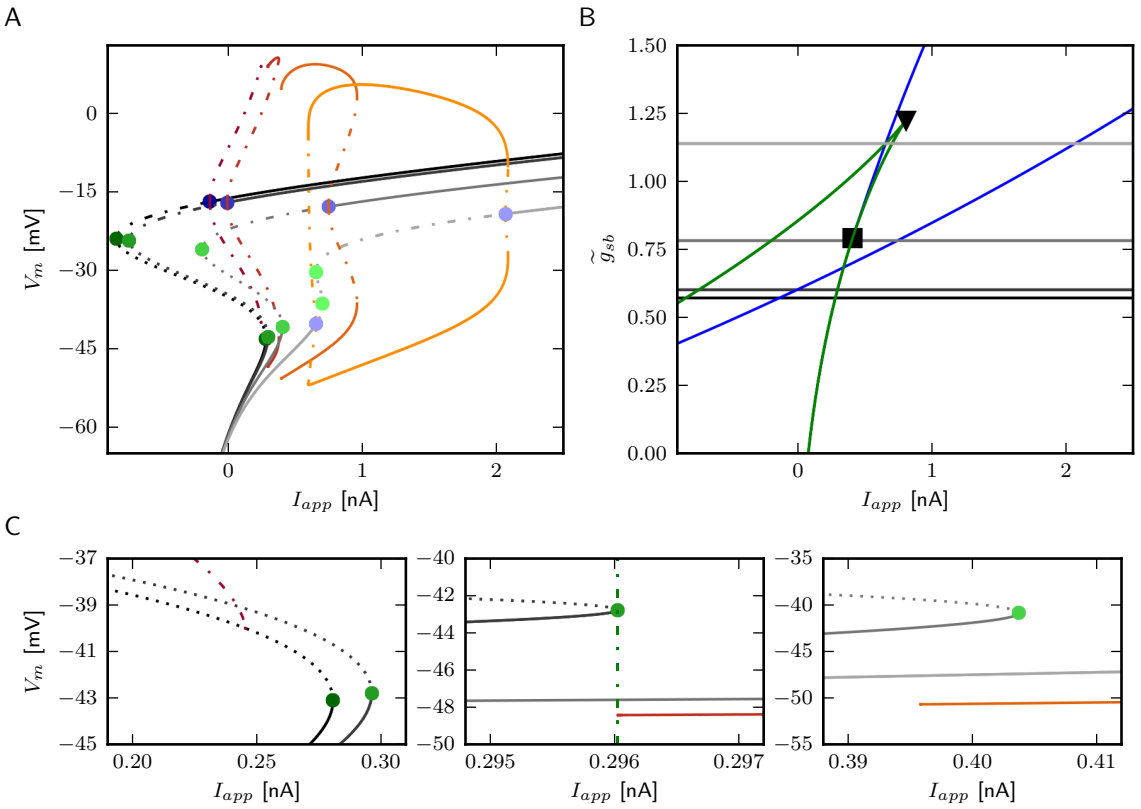

Figure 2.5 Bifurcation structure for different relative Shab densities. A: One parameter bifurcation diagrams for $\widetilde{g}_{sb}$: 0.57, 0.6, 0.782, 1.1347 (black to gray lines). Increasing $\widetilde{g}_{sb}$ changes the transition from rest into spiking from a saddle node (green points) to a Hopf (blue points) bifurcation. The minimum and maximum of periodic solutions are marked by red to orange lines for increasing $\widetilde{g}_{sb}$. The lines style indicates the stability (solid: stable; dashed: unstable)). B: Two parameter bifurcation diagram showing the course of the Hopf (blue) and saddle node (green) curves in the I_{app} x $\widetilde{g}_{sb}$ plane. Square and triangle indicate Bogdanov-Takens and cusp points, respectively. C: Magnification of selected areas in A.

emerges (Fig. 2.5C middel panel), indicating a saddle node on invariant cycle bifurcation and hence type I excitability. The saddle node bifurcation is also present with $\widetilde{g}_{sb} = 0.57$, yet no stable limit cycle could be found. Instead, an unstable limit cycle appears at about $I_{app} = 0.248$ nA and remains unstable until it disappears at the Hopf bifurcation. The trajectories of the system will traverse the phase space towards the more depolarized stable fixed point, if the system is pushed beyond the bifurcation point.

The two parameter bifurcation diagram (Fig. 2.5A) displays the change of the locations of saddle-nodes and Hopf points in the I_{app} - $\widetilde{g}_{sb}$ plane. Low levels of Shab density result in a saddle node bifurcation, and the saddle-nodes remain until $\widetilde{g}_{sb}$ is about 1.2216, where the two branches collide at a cusp point. However, near $\widetilde{g}_{sb} = 0.7895$ and $I_{app} = 0.4087$ there is a Bogdanov-Takens bifurcation. At this point the saddle node curve meets a Hopf curve, and for higher values of $\widetilde{g}_{sb}$, the fixed point loses stability at a Hopf point. This demonstrates that a non-monotonic I-V-curve does not necessarily indicate a loss of stability via a saddle node bifurcation. At $\widetilde{g}_{sb} \approx 0.7$ the right branch of the Hopf curve crosses the right branch of the saddle node curve, this means the system has two stable fixed points for an increasing range of I_{app}.

We use phase plane analysis to further investigate the characteristics of the system with the three chosen $\widetilde{g}_{sb}$ values for which stable periodic solutions can be induced. The model is stimulated with constant current injections of different amplitudes. The amplitudes were chosen to be just below, at and just above the emergence of the limit cycle as determined by the bifurcation diagram of Fig. 2.5. Fig. 2.6 shows the phase plane indicating the fixed points and the stable and unstable manifolds of the neutral saddle, when they exist. Without or with small subthreshold I_{app}, the unstable manifolds terminate at the stable fixed points and form heteroclinic trajectories (Fig. 2.6A and 2.6B left). Letting $\widetilde{g}_{sb} = 0.6$, and injecting a current of 0.296 nA, the unstable saddle point and stable node coalesce and disappear. The trajectory becomes a homoclinic invariant circle and gives rise to a limit cycle with infinite period; that is, stability is lost via a SNIC bifurcation. When I_{app} is increased further, low frequency spiking is induced (Fig. 2.6A right).

Increasing $\widetilde{g}_{sb}$ to 0.782, a single spike can be elicited with $I_{app} = 0.39$ nA. At this value the unstable manifolds still forms a heteroclinic orbit; however, the shape of the stable manifold changes so that it separates the initial values at rest and the stable fixed

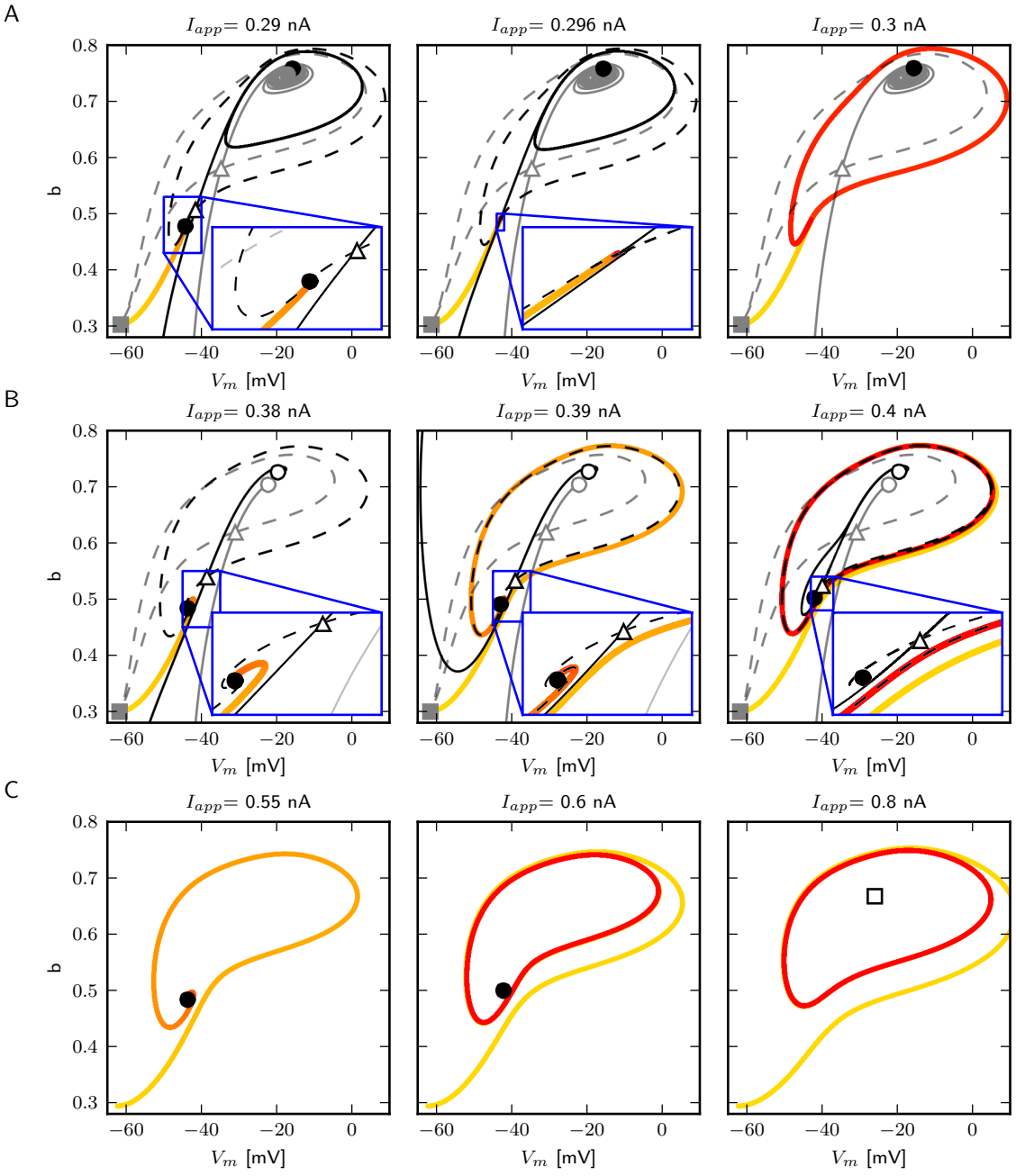

Figure 2.6 Changes of fixed point types and trajectories with increased current injection in phase space. $\widetilde{g}_{sb}$ 0.6 (A), 0.782 (B) and 1.1347 (C). Trajectories corresponding to initial conditions of the steady state without current injection are color coded from yellow (t=t_0) to red (t=t_{max}). Fixed points (gray/black), unstable manifolds (dashed) and stable manifolds (solid) at rest (gray) and for current injections as indicated (black). Fixed point are marked as follows: saddle (triangle), stable focus (filled circle), unstable focus (unfilled circle), stable node (filled square) and unstable node (unfilled square).

point (Fig. 2.6B middle). Hence a single spike is elicited because the trajectory must take a large excursion in order to approach the equilibrium. At $I_{app} = 0.395\,\text{nA}$, one unstable manifold converges onto itself, and a limit cycle attractor appears (Fig. 2.6B right). The trajectory moves around the stable fixed point indicating a saddle big homoclinic bifurcation, where a stable and unstable manifold of a saddle point coincide and form a homoclinic orbit, and the two other branches lie inside the homoclinic orbit. The unstable manifold separates the stable fixed point and the initial conditions at rest, resulting in repetitive spiking. A saddle node bifurcation occurs for I_{app} above $0.4\,\text{nA}$.

When increasing $\widetilde{g}_{sb}$ to 1.1347, stability is lost via a Hopf bifurcation (Fig. 2.6C). With $I_{app} = 0.55\,\text{nA}$, a single spike is elicited (Fig. 2.6C left). A stable limit cycle appears with $I_{app} = 0.6\,\text{nA}$, while the fixed point remains stable (Fig. 2.6C middle). The fixed point becomes unstable when increasing I_{app} (Fig. 2.6C right).

In order to compare the model response to published experimental data, we examine the behavior of the membrane potential over time (Fig. 2.7). Visual inspection reveals that changing $\widetilde{g}_{sb}$ has little influence on the spike shape. With $\widetilde{g}_{sb} = 0.6$, arbitrarily low firing frequencies with long delays to spike can be evoked, indicating type I dynamics. Current pulses with an amplitude of $0.8\,\text{nA}$ elicit a single spike and subsequent low amplitude oscillations. Although the transition from rest to spiking occurs via different bifurcations, similar firing patterns are elicited with $\widetilde{g}_{sb}$ values of 0.782 and 1.1347. In both cases a single spike can be elicited with small I_{app}, while slightly increased stimulus amplitudes induce repetitive spiking with relatively high frequencies, indicating type II dynamics. Furthermore the delay of spiking is small compared to observations when $\widetilde{g}_{sb} = 0.6$. In contrast to what was reported by Herrera-Valdez et al. (2012), the frequently observed pattern of a single spike with small and repetitive spiking with increased stimulus amplitudes in experiments can be generated with a system near a Hopf (Fig. 2.7,

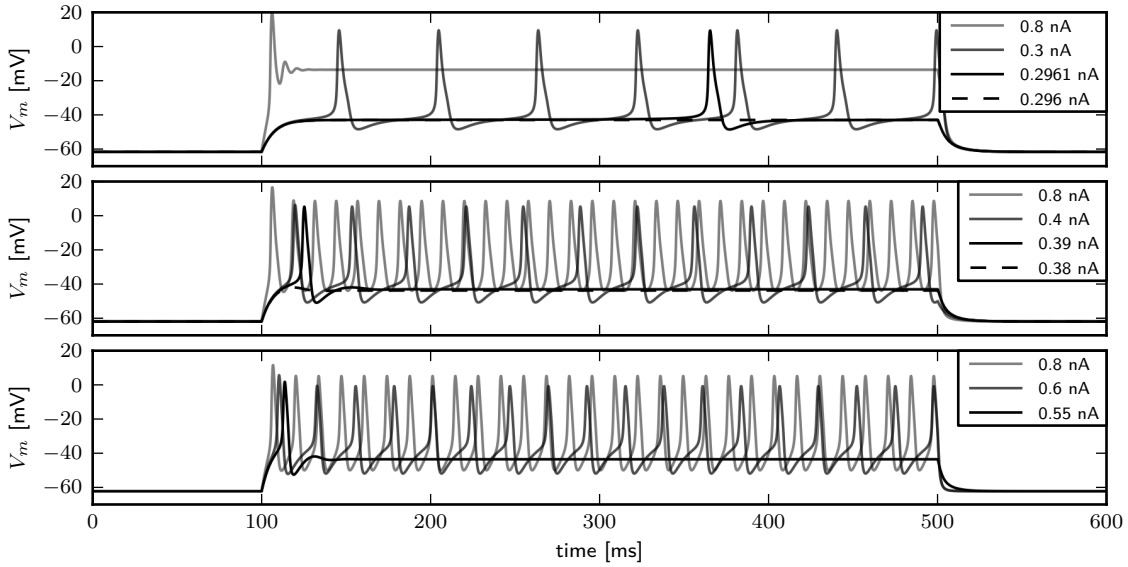

Figure 2.7 Firing behavior for different relative Shab densities in the two dimensional model. Responses to steady current injection, from top to bottom $\widetilde{g}_{sb}$: 0.6, 0.782, 1.1347 with R_{in} 70.2, 69.5, 65.4 and 59.4 MΩ.

bottom) as well as with a system near a saddle node bifurcation (Fig. 2.7, middle). Note however that the range of current amplitudes where a single spike is elicited is narrow.

2.3.3.4 Responses to Time Varying Input

These different bifurcation types imply different PRCs and different responses to periodic forcing. Therefore the next step is to calculate the PRCs and analyze the model behavior for periodic current stimulation.

We use periodic current injections with the shape of a sine wave with varying periods to assess the model response to periodic forcing and to find the preferred frequency of the model. The frequency sweeps from 0 to 30 Hz linearly over a time interval of 10 s. As expected, systems near a saddle node bifurcation with $\widetilde{g}_{sb}$ of 0.6 or 0.782 displays integrator properties, behaving as a low-pass filter of the input current (Fig. 2.8A top and middle panel). In both cases the amplitude of the membrane potential decreases with stimulus frequency. Current amplitudes above the respective bifurcation points are required to

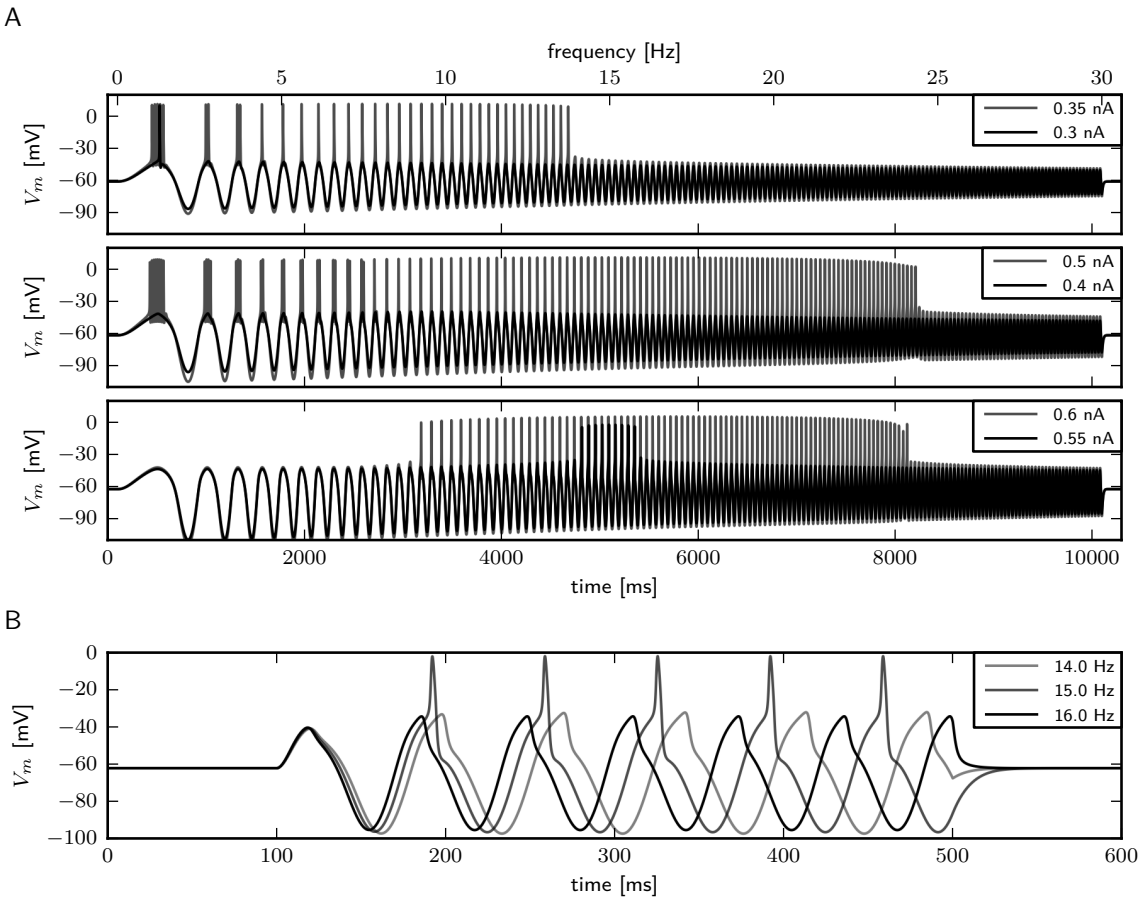

Figure 2.8 Firing behavior in response to periodic forcing for different relative Shab densities in the two dimensional model. A: Responses to swept sine current injection, with frequencies from 0 to 30 Hz. From top to bottom $\widetilde{g}_{sb}$: 0.6, 0.782, 1.1347. B: Responses of the model with $\widetilde{g}_{sb}$=1.1347 to sinusoidal forcing with three different frequencies.

induce APs even at low frequencies. With larger amplitudes repetitive firing is induced at low frequencies and the spike count per cycle declines with increasing frequency. In contrast, with $\widetilde{g}_{sb} = 1.1347$, the model exhibits resonator properties, acting as a band-pass filter of input current. Stimulation with low amplitude swept sine current injection reveals that frequencies around 15 Hz elicit APs, while higher and lower frequencies only cause graded responses (Fig. 2.8A, bottom panel). Upon increasing the stimulus amplitude, the frequency band that yields spiking becomes larger. Sinusoidal current injections confirm that with an amplitude of 0.55 nA a frequency of 15 Hz, but not 14 or 16 Hz re-

sults in the generation of APs (Fig. 2.8B). In summary, while the response properties to constant current injection with $\widetilde{g}_{sb}$ of 0.782 and 1.1347 are quite similar, the responses to periodic forcing are dramatically different.

How a rhythmically firing neuron responses to perturbations can be analyzed with the PRC. It provides a measure for the timing of the subsequent AP after a brief stimulus at a specific time during the spiking cycle. If a neuron spikes repetitively with a certain frequency with constant I_{app} or without a driving force, the state of the neuron can be expressed by a single phase variable. To obtain the phase, the time of a peak voltage equates to a phase of zero and subsequent times are divided by the spiking period to obtain the phase. The PRC gives the phase shift induced by a perturbation as a function of the phase at which the perturbation occurs. Positive values indicate a phase advance, which means the next AP will be sooner, while negative values indicate a phase delay, which means the next AP will be later than without perturbation. PRCs that are mostly positive are called type I, whereas PRCs that have a positive and a negative component are classified as type II. In order to classify PRCs as type I or type II, Tateno and Robinson (2007) introduced a r-value, the ratio of maximal phase delay and advance, of 0.175.

Fig. 2.9 shows the PRCs of the model for the different indicated $\widetilde{g}_{sb}$ values. With $\widetilde{g}_{sb} = 0.6$ the PRC can be classified as type I, with r-values of 0.01, 0.04 and 0.15. By increasing $\widetilde{g}_{sb}$ to 0.782, the PRC has small negative values for small phase values, but the r-values with 0.067, 0.064 and 0.14 still leads to a classification as type I. With a further increase of $\widetilde{g}_{sb}$ to 1.1347, the negative values in the early phase increase, for small baseline I_{app} of 0.596 and 0.6 nA the PRC is type II, with r-value of 0.192 and 0.179 bigger than 0.175. However, with a baseline I_{app} of 0.7 the r-value is 0.130. As can be seen by the bifurcation diagram in Fig. 2.5, although the stable fixed point loses stability via a Hopf bifurcation, there is also a saddle node bifurcation near $I_{app} = 0.7\,\text{nA}$, which might in-

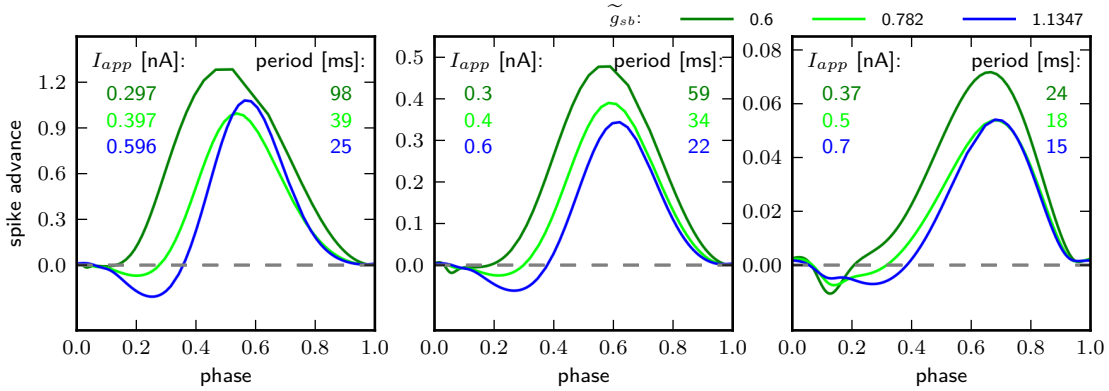

Figure 2.9 Phase response curves for different relative Shab densities (indicated by colors) and from left to right for increasing I_{app}, as indicated.

fluence the vector field in a way that the model exhibits a type I PRC. For higher baseline I_{app} the r-value increases and exhibits a PRC classified as type II (not shown). Also when increasing $\widetilde{g}_{sb}$ to 1.5 the PRC is classified type II for all probed stimulus amplitudes that elicit repetitive spiking (not shown).

The PRC corresponding to all three $\widetilde{g}_{sb}$ values have in common that they are relatively insensitive to perturbations at the beginning and the end of the cycle shortly before and after the peak of the AP. Further, the maximum of the PRC shifts to the right with higher baseline stimulation.

2.3.3.5 Small Parameter Changes Induce Delay to First Spike

The only firing profile that could not be reproduced by changing $\widetilde{g}_{sb}$ is an onset with a long delay and subsequent higher frequency. Usually a saddle small homoclinic bifurcation is responsible for such an behavior (Izhikevich, 2007). We explored the parameter space further in order to find a regime where the system undergoes this bifurcation. We set z^b to a constant value of 1.5 in order to obtain a better description of the Na^+ channel inactivation (see Section 2.3.1). Then we performed the fitting routine, resulting in the parameter set sb_z (see Tab. 2.1) with which that firing profile can be repro-

duced(Fig. 2.10C). The bifurcation diagram for $\widetilde{g}_{sb} = 1.35$ reveals that at $I_{app} \approx 0.1392$ the minimum on the periodic orbit colides with the saddle node and the coexisting stable fixed point is at a smaller V_m (Fig. 2.10A). By increasing $\widetilde{g}_{sb}$, the system exhibits the same bifurcation types as with the default parameters sb_{def}. With this set of parameter the $\widetilde{g}_{sb}$ has to be much higher for a model that displays the various firing patterns, as with the previously used parameters.

Phase plane analysis confirms that the underlying bifurcation when $\widetilde{g}_{sb} = 1.35$ is indeed a saddle small homoclinic bifurcation (Fig. 2.10B), where one stable and one unstable manifold collide and form a homoclinic orbit; the remaining two manifolds lie outside the homoclinic orbit. At low values of I_{app} one of the unstable manifolds connects to the less depolarized stable fixed point, traversing around the more depolarized stable fixed point, as well as, around the stable manifold that emerges from the unstable periodic orbit around that fixed point (Fig. 2.10B, left). Increasing I_{app} beyond the bifurcation point, the unstable manifold converges onto itself and the stable manifold is now on the outside of the resulting limit cycle (Fig. 2.10B, middle right). The saddle point stable node both remain, hence the model is bistable. A constant current pulse does not induce repetitive spiking, because the state of the system is not pushed beyond the stable manifold. However, applying an additional short pulse can push the system onto a trajectory that converges onto the periodic orbit (Fig. 2.10B, right and Fig. 2.10C, yellow line).

As expected for a system near a saddle node bifurcation, the model exhibits integrator properties, as revealed by swept sinusoidal current injection (Fig. 2.10D). The PRC is biphasic (Fig. 2.10E) with an r-value above 0.175, but differs from those shown in Fig. 2.9. A perturbation shortly before, during and after the peak of an AP results in a delay of the subsequent AP. For small I_{app}, the region where a perturbation causes the strongest

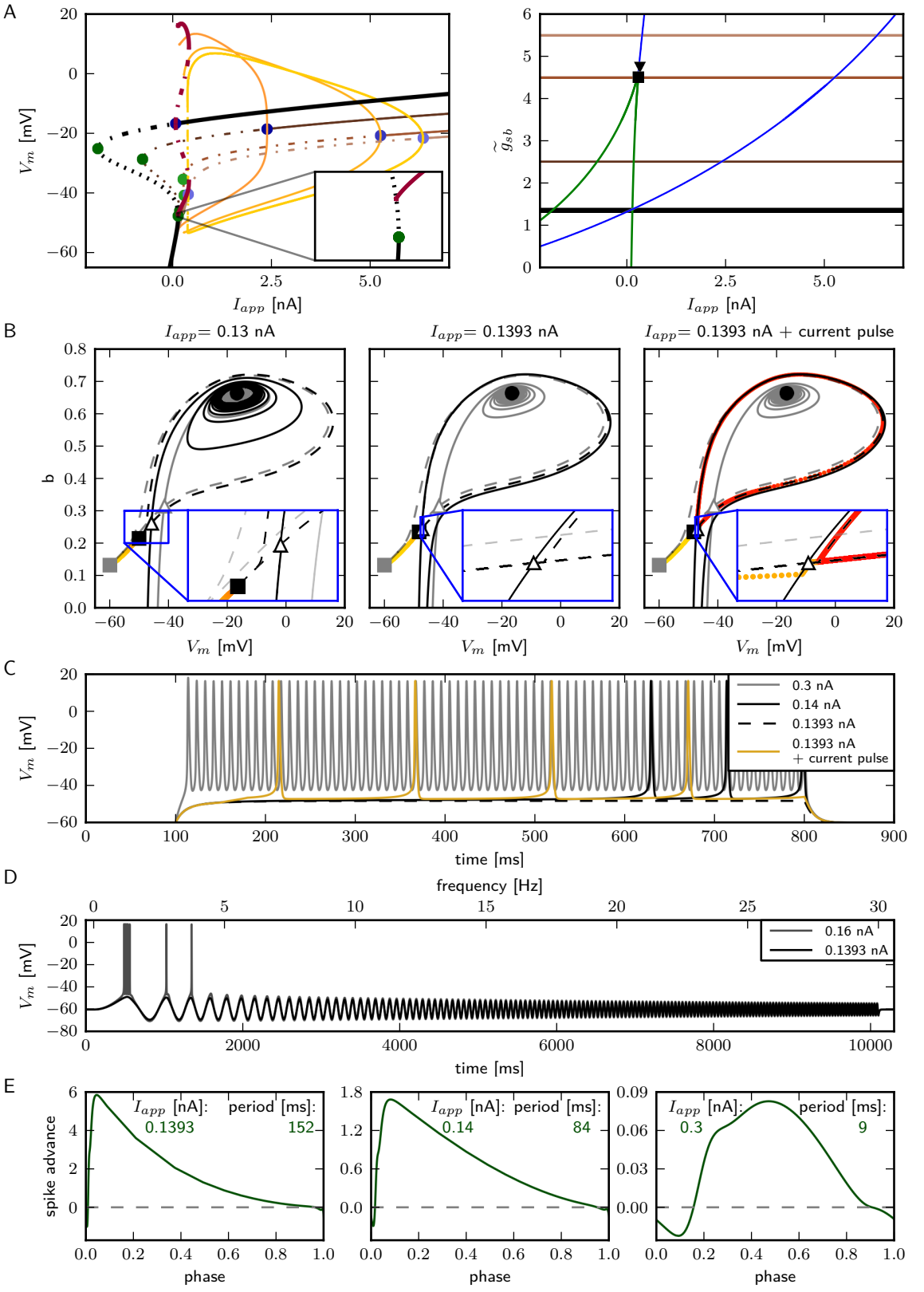
A
V_m [mV]
I_{app} [nA]
$\widetilde{g}_{sb}$
B
I_{app}= 0.13 nA
I_{app}= 0.1393 nA
I_{app}= 0.1393 nA + current pulse
b
V_m [mV]
C
0.3 nA
0.14 nA
0.1393 nA
0.1393 nA + current pulse
time [ms]
D
frequency [Hz]
0.16 nA
0.1393 nA
time [ms]
E
spike advance
I_{app} [nA]: period [ms]:
0.1393 152
0.14 84
0.3 9
phase

phase advance is shortly after the peak of the AP and much earlier during the spiking cycle at a phase of approximately 0.1. Increasing I_{app} to 0.3 nA, the peak of the phase advance shifts to the right, and the PRC has more resemblance to the ones shown in Fig. 2.9.

2.3.3.6 Impact of Leak Conductance

An estimate for input resistance (R_{in}) is obtained by applying Ohm's law to the steady state voltage response for small I_{app}. With the chosen value of 0.036 for $\widetilde{g}_L$, depending on the Shab density, R_{in} is between 59.4 and 70.2 MΩ (Fig. 2.11A top left). This is below the experimentally measured R_{in} in MN5 of 97±31 MΩ (Duch et al., 2008). However the amplitude of I_{app} for which the stable fixed point loses stability and/or a stable limit cycle emerges for small $\widetilde{g}_{sb}$ is below 0.4 nA (Fig. 2.11A middle, left), which is the typical amplitude that induces repetitive spiking in MN5. For higher $\widetilde{g}_{sb}$, on the other hand, the

Figure 2.10 *(preceding page)* Saddle small homoclinic bifurcation with changed Shab parameters. A: Right: Bifurcation diagram shows, that with $\widetilde{g}_{sb}$=1.35 a stable limit cycle (dark red) coincides with the curve of saddle nodes (black dots), while the stable fixed point vanishes via a saddle node bifurcation at a bigger I_{app}. Increasing $\widetilde{g}_{sb}$ (dark to lighter brown and orange for fixed points and periodic solutions) changes the transition from rest into spiking from a saddle node (green points) to a Hopf (blue points) bifurcation. Dashed and solid lines mark stability (solid: stable; dashed unstable). Left: Two parameter bifurcation diagram indicating the location of Hopf points (blue) and saddle nodes (green) as well as the Bogdanov-Takens (square) and cusp (triangle) points with respect to $\widetilde{g}_{sb}$ B: Changes of fixed point types and trajectories with increased current injection in phase space. Fixed points (gray/black), unstable manifolds (dashed) and stable manifolds (solid) at rest (gray) and for current injections as indicated (black). Fixed points are marked as follows: saddle (triangle), stable focus (filled circle), unstable focus (unfilled circle), stable node (filled square) and unstable node (unfilled square). Trajectories corresponding to initial conditions of the steady state without current injection are color coded from yellow (t=t_0) to red (t=t_{max}). C: Responses to steady current injection. The stimulus inducing the response shown in green exhibits an additional 30 ms and 0.01 nA current step at t=150 ms. D: Responses to swept sine current injection, with frequencies from 0 to 30 Hz. E: PRCs for increasing I_{app}, as indicated.

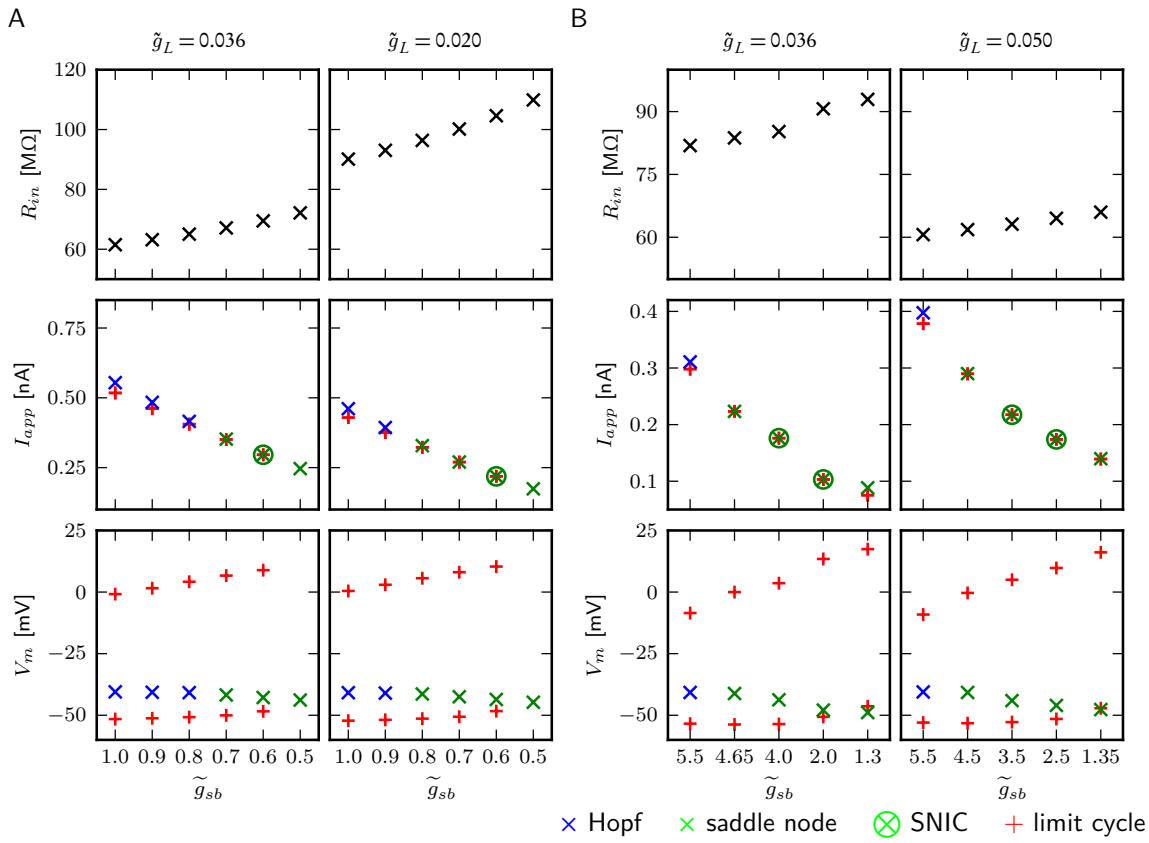

Figure 2.11 Small changes of $\widetilde{g}_L$ adjust for R_{in}, but have no influence on bifurcation types the system can exhibit. Different aspects of the model behavior as function of $\widetilde{g}_{sb}$ for two different $\widetilde{g}_L$. In A and B the default and changed Shab channel models are used, respectively. Top panels show R_{in} measured with small current injections. Middle panels show the minimal amplitudes of I_{app} for which a stable limit cycle emerges (red pluses) and the fixed point loses stability (blue and green crosses). Bottom panels show V_m of the fixed points near the bifurcation (blue and green crosses) and the minimum and maximum of the limit cycles (red pluses).

spiking threshold is too high. R_{in} and the inversely related amplitude of I_{app} that elicits APs can be adjusted by changing $\widetilde{g}_L$. We decrease $\widetilde{g}_L$ to 0.02 and investigate whether this changes the bifurcations the system exhibits. As before, $\widetilde{g}_{sb}$ was set to different values and the fixed points, periodic solutions and bifurcations that occur as I_{app} is changed are determined using numerical continuation. To resolve whether a limit cycle occurs via a SNIC or homoclinic bifurcation, we compare the minimal I_{app} for which a periodic

solution was found with I_{app} of the saddle node bifurcation (Fig. 2.11A and B, middle). If amplitudes of I_{app} are equal it indicates a SNIC otherwise a saddle homoclinic bifurcation. To further distinguish between a small and big homoclinic bifurcation, the value of V_m at the fixed point and at the minimum of the periodic orbit are compared (Fig. 2.11A and B, bottom). This analysis reveals that with increased $\widetilde{g}_L$, the same bifurcation types can be elicited by changing $\widetilde{g}_{sb}$. The change between bifurcations may occur at different $\widetilde{g}_{sb}$ levels; i.e. with $\widetilde{g}_{sb} = 0.8$ stability is lost via Hopf bifurcation when $\widetilde{g}_L = 0.036$, while it is lost via a saddle node bifurcation when $\widetilde{g}_L = 0.02$. However, increasing $\widetilde{g}_L$ leads to spiking onset in response to smaller I_{app} (Fig. 2.11A, middle) and decreasing $\widetilde{g}_L$ further ultimately would result an unstable steady state without current injection, with small $\widetilde{g}_{sb}$. Therefore a loss of stability via a Hopf bifurcation would be the only possibility for a model that is quiescent with I_{app}=0 nA. Also, it can not be excluded that there exists a $\widetilde{g}_{sb}$ value, for which the model exhibits a saddle small homoclinic bifurcation resulting in the appearance of a stable limit cycle, but that this value was not found.

With the changed Shab parameters, the default value of $\widetilde{g}_L$ with 0.036 results in higher R_{in}, but in turn, the bifurcations occur at rather small values of I_{app}. Therefore $\widetilde{g}_L$ is increased to 0.05. Fig. 2.11B demonstrates that the change in $\widetilde{g}_L$ is not the cause of the saddle small homoclinic bifurcation resulting in the appearance of a stable limit cycle.

The chosen default value for the leak conductance is a compromise in the attempt to match sensitivity to current injection and input resistance with experimental data. The apparent missmatch might be a consequence of the fact that the model incorporates only two channel types.

2.3.4 Independent Na^+ Channel Inactivation

To further investigate whether the changed bifurcation structure found with the changed parameter set sb_z is a consequence of altering the activation of the Shab current, the inactivation of the Na^+ current or whether it is necessary to alter both channels, we introduce a further variable representing the Na^+ channels inactivation. This allows for a better fit of the Na^+ inactivation as has been demonstrated in the Section 2.3.1 . Increasing the gating charge results in a good match to the inactivation curve derived by Olson et al. (2008) (Fig. 2.1D). However the time constants are not available from this data. Using the same values as before, the model exhibits APs with a peak of $-10\,\mathrm{mV}$ and the maximal $\mathrm{d}V_m/\mathrm{d}t$ is below $20\,\mathrm{mV/ms}$. This is adjusted by decreasing r^m to $1.5\,\mathrm{ms}^{-1}$ and increasing $\overline{g}_{Na}$ to $20\,\mu\mathrm{S}$.

With the 3-dimensional formulation, similarly to the 2-dimensional model, high Shab densities result in a Hopf bifurcation, while low densities result in a saddle node bifurcation (Fig. 2.12). Firing patterns similar to those observed with the two dimensional model are generated. With very low $\widetilde{g}_{sb}$ levels, the branch of the minimas of the periodic solution coincides with the unstable branch of saddle points (Fig. 2.12A and C, left). The minimum of the periodic orbit is therefore above the stable fixed point, which coexists at the stimulus amplitude where the limit cycle emerges. In the two dimensional model, this was due to a saddle small homoclinic bifurcation (see Section 2.3.3.5). As in the two dimensional case, the membrane responds with a long delay to first spike and subsequent higher firing frequency to small square pulse current injections (Fig. 2.13A, first panel), the model acts as low-pass filter (Fig. 2.13B, first panel) and the PRC is biphasic displaying a phase delay shortly before and after an AP. A phase advance occurs at <0.1 and >0.9 of the phase; systems with other bifurcation structures display only weak responsiveness to perturbations at this time within the cycle (Fig. 2.13C). Increasing $\widetilde{g}_{sb}$ to 0.4,

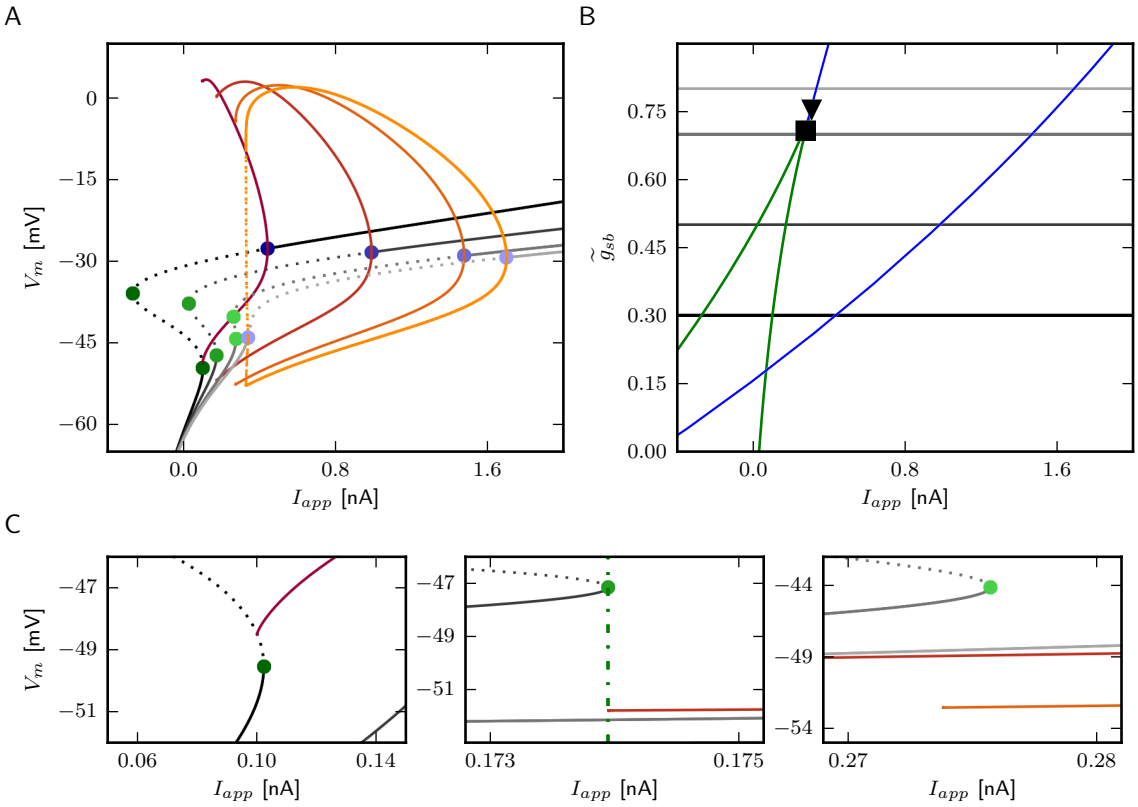

Figure 2.12 Bifurcation structure for different Shab channel densities in the three dimensional model. A: Bifurcation diagram shows that increasing $\widetilde{g}_{sb}$ changes the transition from rest into spiking from a saddle node bifurcation (blue points) to a Hopf bifurcation (green points). Fixed points are drawn in black to gray and the minimum and maximum of the periodic solutions shown in red to yellow for $\widetilde{g}_{sb}$: 0.2, 0.4, 0.6 and 0.8. Dashed and solid lines mark stability (solid: stable; dashed unstable). B: Two parameter bifurcation diagram indicating the location of Hopf points (blue) and saddle nodes (green) as well as the Bogdanov-Takens (square) and cusp (triangle) points with respect to $\widetilde{g}_{sb}$. C: Magnification of selected areas in A.

stability is lost via a SNIC bifurcation (Fig. 2.12A and C, middle). The model exhibits infinitely low frequency and a delay to first spike with the same duration as the following ISI (Fig. 2.13A second panel), low-pass filter (Fig. 2.13B, second panel) properties, and a type I PRC (Fig. 2.13C). With $\widetilde{g}_{sb} = 0.6$ the stable fixed point still loses stability via a saddle node bifurcation; however, a periodic orbit emerges before that point (Fig. 2.12A and C, right), with the minimal value of V_m smaller than for the stable fixed point. In

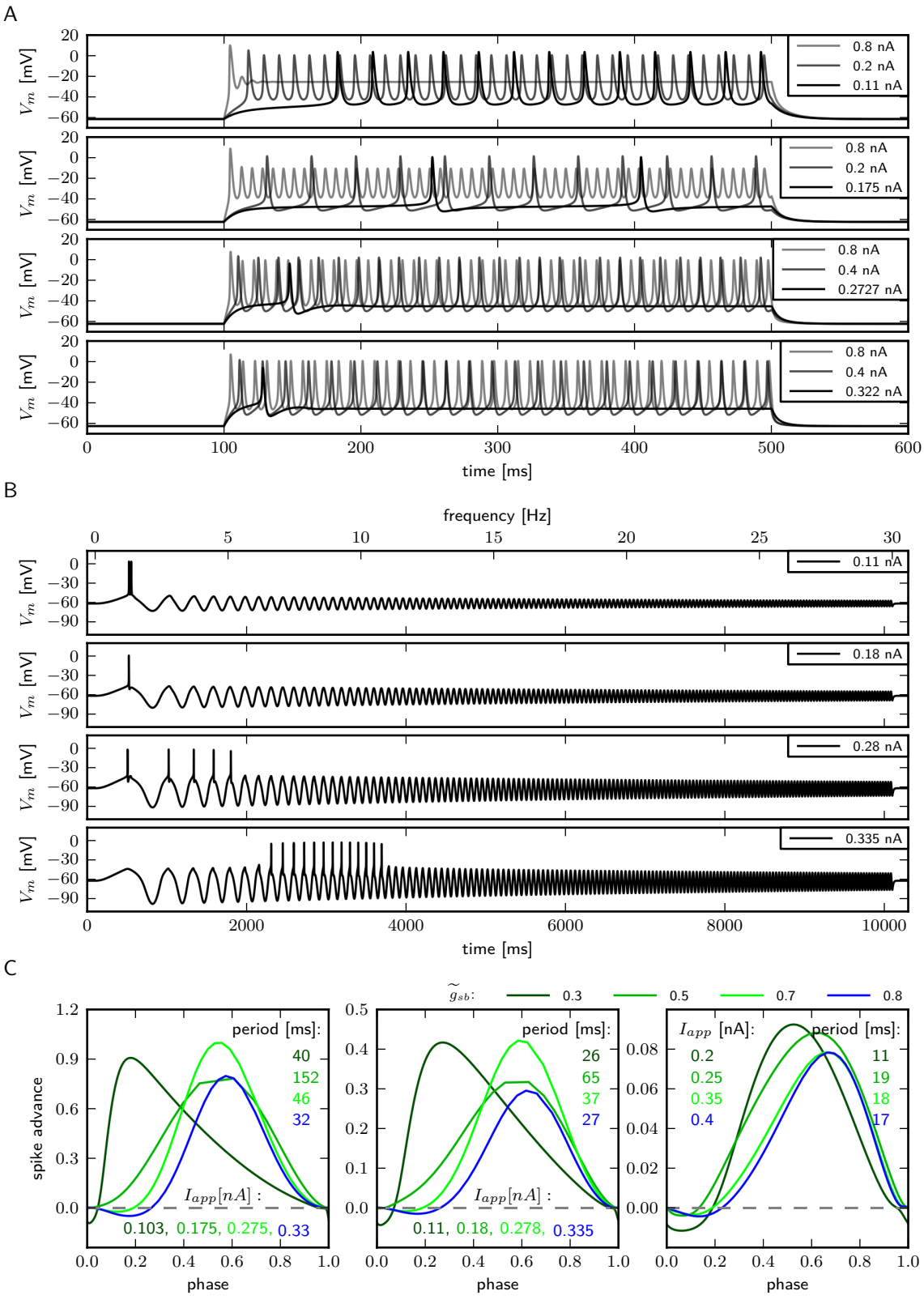
A
V_m [mV]
0.8 nA
0.2 nA
0.11 nA
0.175 nA
0.4 nA
0.2727 nA
0.322 nA
time [ms]
B
frequency [Hz]
0.18 nA
0.28 nA
0.335 nA
C
$\widetilde{g}_{sb}$:
0.3
0.5
0.7
0.8
spike advance
period [ms]:
40
152
46
32
$I_{app}[nA]$:
0.103, 0.175, 0.275, 0.33
26
65
37
27
0.11, 0.18, 0.278, 0.335
I_{app} [nA]:
0.2
0.25
0.35
0.4
11
19
18
17
phase

the two dimensional model phase plane analysis revealed that this is due to a saddle big homoclinic bifurcation. With $\widetilde{g}_{sb}$ 0.6 and 0.8, a single spike is induced for sufficiently low current stimulation. With higher current injection, a shorter delay to first spike than the following ISI (Fig. 2.13A third and fourth panel) is seen. The PRCs are similar as well (Fig. 2.13C), but the model shows resonator properties only when stability is lost via a Hopf bifurcation with $\widetilde{g}_{sb} = 0.8$, (Fig. 2.13B).

With this model, smaller current injection leads to repetitive spiking, and the changes between bifurcation types occur for smaller $\widetilde{g}_{sb}$. Furthermore increasing the stimulus amplitude results in spikes with smaller amplitude, and the transition out of spiking at high current levels occurs via a subcritical Hopf bifurcation.

In summary, as with the changed parameters for the Shab channels (sb_z), the three dimensional model displays four types of bifurcations when varying the Shab channel density by a factor of 4. This demonstrates that the additional bifurcation due to changed parameters in the two dimensional model (see Section 2.3.3.5) can be achieved by simply adjusting the Na^+ channel inactivation kinetics.

2.4 Discussion

In this Chapter, we first developed a two-dimensional excitable membrane model with currents based on biophysical parameters of *Drosophila* Shab and $DmNa_v29$ channels. This model was used to assess which features of experimentally observed firing behavior can be produced by varying only the Shab channel density. Using phase plane and bifurcation analysis, the model was investigated and tuned to reproduce experimentally

Figure 2.13 *(preceding page)* Firing behavior and PRC for different Shab channel densities in the three dimensional model. Responses to steady (A) and swept sine (B, frequencies 0 to 30 Hz) current injection for (from top to bottom) $\widetilde{g}_{sb}$: 0.2, 0.4, 0.6, 0.8; with R_{in} 94.5, 82.7, 75.1 and 72.1 MΩ. C: PRCs for increasing I_{app}, as indicated.

observed firing patterns. The bifurcation types the models undergo as current is injected was assessed with respect to varying channel densities using stability analysis. The two-dimensional model was then extended to a three-dimensional model in order to include independent Na^+ inactivation.

In preliminary studies, we investigated the influence of A-type channels on *Drosophila* MN5 firing behavior and found that, in accordance with experimental results, Shal and Shaker can influence the firing patterns and bifurcation structure of a neuron differently (Herrera-Valdez et al., 2009; Herrera-Valdez et al., 2010). However, in order to determine for which behaviors the incorporation of potassium channels with voltage dependent inactivation kinetics are necessary, we first need to know whether those properties can be induced without those channels.

We find that a wide array of firing patterns can be generated with only two currents. Specifically, properties like the long delay to first spike and slow firing frequencies, that were thought to be unique features induced by incorporating A-type channels (Choi et al., 2004; Ping et al., 2011; Schaefer et al., 2010), can be induced in our model.

2.4.1 Minimal Excitable Membrane Model

We developed a minimal model consisting of one regenerative current that amplifies changes and one restorative current that counteracts changes of V_m. The regenerative current is a Na^+ current; the restorative current is a delayed rectifier K^+ current based on channels encoded by *shab*. In *Drosophila* there are only four genes, *shaw*, *shab*, *shal* and *shaker*, that encode voltage gated K^+ channels. Shab channels were chosen because it has been shown that they provide delayed rectification in *Drosophila* and are required to induce repetitive firing. This can also be inferred by the different dynamics of the channels. Shaw channel have a very low voltage sensitivity and mediate a leak current. Shaker

and Shal channels mediate transient A-type current, where their steady state activation curves are more hyperpolarized than the one from Shab channels, and they express fast inactivation kinetics. This indicates that they play a role in regulating spike initiation and repetitive firing patterns but do not play a major part in inducing repetitive firing. This goes in line with experimental findings, Shaker mutants display broader APs and higher firing frequencies, while Shal has been reported to increase the spiking threshold and to induce a delay to first spike (Choi et al., 2004; Ping et al., 2011).

In the model, $\overline{g}_{Na}$ was assigned by comparing the wave forms in response to current injection of the *in situ* measured membrane potential at the soma of MN5 and the model. We did not aim to reproduce the shape of the APs exactly, since we only incorporate a small subset of channels in our models and it is likely that the shape measured in MN5 is influenced by additional channels. Instead the maximal $\mathrm{d}V_m/\mathrm{d}t$ was compared. However, it is not clear whether the depolarization observed at the soma results from passive spread of APs, whether there is an additional spike generating zone close by or at the soma, or whether active properties at the soma boost the AP generated at the SIZ. When the SIZ is far away from the soma it is possible that the shape of APs observed at the soma, is attenuated and broader than at the SIZ due to the filtering properties of passive structures. The maximal $\mathrm{d}V_m/\mathrm{d}t$ measured from recordings of MN5 is small compared to values reported in other preparations, where it is about 100 and $300\,\mathrm{mV/ms}$ in neurons of the cat visual cortex *in vivo* and *in vitro* (Naundorf et al., 2006) or about $200\,\mathrm{mV/ms}$ in ganglion cells from the tiger salamander (Fohlmeister and Miller, 1997). This means that the maximal $\mathrm{d}V_m/\mathrm{d}t$ at the SIZ, and thus $\overline{g}_{Na}$ may be higher.

2.4.2 Relation of Channel Density and Firing Patterns

Our results demonstrate that small changes in $\widetilde{g}_{sb}$ are sufficient to produce different firing patterns that relate to those observed experimentally. The differences can be linked to a change in the underlying mathematical structure of the system, yielding qualitatively different transitions between rest and spiking. The differences in observed firing behaviors of MN5 *in situ* indicate that the neuron might be close to a bifurcation with co-dimension greater than one, where such a change of the bifurcation type with respect to I_{app} occurs. However, MNs are required to exhibit reliable outputs during behavior since they are the final processing station, and alternating input-output behavior cannot be adjusted by network properties. Therefore, the observed differences could be due to different modulatory states that tune the neurons' output for specific needs. For example, biogenic amines like octopamine and tyramine influence the take-off likelihood and flight maintenance significantly (Brembs et al., 2007). Further, MN5 exhibits tonic firing during flight, only single APs and no doublets or triplets are observed; during male courtship song, pulse firing is shown. Although this could be due to different input, the different firing patterns may also be supported by differences in the intrinsic excitability and thus the modulatory state.

In the model, low shab concentrations induce behavior thought to be induced by A-type channels. However, at small $\widetilde{g}_{sb}$, the range of stimulus amplitudes for which a stable periodic solution exists is rather narrow. In the three-dimensional model and the model with altered channels kinetics, the AP amplitude increases drastically with increased current.

Some experimentally observed features of the firing patterns could not be reproduced well by this model. Further channels may be necessary to support some behavior combinations like integrator properties together with a higher input resistance and a higher

firing threshold. Additionally, having more channels that in different combinations produce a similar behavior, can add to the robustness of the system and provides a way to adjust for natural variability. Furthermore, adaptation could not be generated, since it requires a third time scale, and therefore a further variable (Guckenheimer et al., 1997).

Bistability occurs in the model for a very specific combination of constant stimulus amplitude and timing of pulse stimulation. Although bistability has not been reported for experimental studies, the model results suggest that it is unlikely this phenomenon would be observed. If observed, the neuron might be rejected and assessed as being not intact. Further, a long delay to first spike with subsequent ISI of similar duration, as typical for a system close to a SNIC bifurcation was not reported as an observed firing pattern in Herrera-Valdez et al. (2012). However this firing pattern was recorded at least once in *eag* and *shaker* double knock downs, as shown by Duch et al. (2008) in Fig.2C. It must be noted that the quantification of firing patterns of wild type MN5 as reported in Duch et al. (2008) and Herrera-Valdez et al. (2012) is different. Maybe the recording conditions changed between these sets of experiments.

2.4.3 Variability in Ion Channel Density

It has been shown that ion channel expression, as well as the maximal conductances of ion currents in neurons, can be extremely variable. *Shab* mRNA in MNs of the crustacean stomatogastric nervous system vary two to four fold (Schulz et al., 2006; Schulz et al., 2007) and four fold in gastric mill neurons. In *Drosophila* MN5, voltage clamp recordings reveal that the peak of the total K^+ current can vary by a factor of about four (Ryglewski and Duch, 2009). In our models a variation of up to four-fold is sufficient to produce the different firing patterns and bifurcation structures. However, it has also been shown that the expression patterns of certain ion channel combinations are coordinated,

where the specific combinations depend on the cell type. In gastric mill neurons Na^+ and Shab channels are correlated, but in all other investigated cells, the mRNA abundance of the genes encoding these two channels are independent.

2.4.4 Influence of Phasic Input on Output Behavior

During flight, the firing frequency of the MNs is modulated simultaneously (Levine and Wyman, 1973) and studies support the idea that the firing frequency is an inherent property of the neurons (Harcombe and Wyman, 1977), which is changed when the required power output is changed (Gordon and Dickson 2006). Together with the observation that two MNs never fire in a time window of about 5 ms, it was concluded that all MNs receive common excitatory input and that the MNs interact reciprocally (Harcombe and Wyman, 1977). In other words, the common excitatory input induce periodic spiking of the units, and the reciprocal interactions cause a perturbation of the period depending on the phase when the input is received. An analysis of how a neuron responds to phasic input while firing repetitively is measured with PRCs. The claim of Harcombe and Wyman (1977) and Koenig and Ikeda (1983) that there is a strong interaction if one MN fires simultaneously or shortly before another MN, requires a PRC with large phase shifts at the very beginning and end of the period, as observed in models close to a saddle small homoclinic circle. Those models also display a long delay to first spike with shorter ISIs to constant current injection, a firing pattern that is often observed in neurons at larval stage, but rather seldom in adult MN5s. However, in our model, this pattern corresponds to current injections very close to the spiking threshold. Therefore it could also mean that this pattern manifests at stimulus amplitudes that fall between the probed current steps.

In the two dimensional model with the default channel kinetics the delay to first spike could not be reproduced. We have shown with the electro-diffusion model, that this does not require the introduction of a further variable (Herrera-Valdez et al., 2012) rather a change of z^b in combination with a low $\widetilde{g}_{sb}$ value elicits this behavior. In the model investigated here, a simple change of z^b is not sufficient to produce this profile. However it is produced by models with moderate changes in more than one parameter and more importantly, after incorporating independent Na^+ inactivation dynamics.

2.4.5 Comparison to Other Excitable Membrane Models

Various minimal conductance based models have been employed in previous studies, in order to analyze the electrical behavior of neurons. For example Prescott et al. (2008) employed a two dimensional model based on the Morris-Lecar-model (Morris and Lecar, 1981; Rinzel and Ermentrout, 1998) and showed that all three types of excitability could be reproduced with that model. However, here we show that a neuron model based on more realistic ion channel mechanisms can also exhibit all three types of firing behavior. Zeberg et al. (2010) used models in which diverse potassium current were combined as one recovery variable and found that the variation of channel densities can switch the model from resonator to integrator. This study demonstrates that incorporating only one delayed rectifier K^+ channel in the model and varying its density is sufficient to induce this switch.

In another modeling effort, a electro-diffusion model was developed based on MN5 (Herrera-Valdez et al., 2012), but this model falls short in reproducing the Na^+ channel kinetics. It is not clear whether the theoretical improvement of the model is indeed that substantial to justify the accompanied increasing complexity of the model, or whether instead, simplifications made elsewhere have a more appreciable influence on the accuracy

of the model, like the simplified model of the gating mechanism. Herrera-Valdez (2012) state that a big advantage of the electo diffusion model is that the maximal currents can be fitted directly to electrophysiological data. However, electrophysiological data are often preprocessed under the assumption of a linear current-voltage relationship, for example when leak currents are subtracted from the traces. This model also fails in generating spikes on elevated potentials as observed experimentally. This, however, can also emerge because the recording site is far away from the SIZ.

In another recent study, a model of *Drosophila* third-instar larval motoneuron was developed in order to investigate the impact of alternative splicing of Na^+ channels. (Lin et al., 2012). In that model the sodium channels have activation kinetics as in the classical Hodgkin-Huxley model formalism. The time constant is based on electrophysiological recordings in embryonic *Drosophila* motoneuron (O'Dowd and Aldrich, 1988). The measured Na^+ current is possibly a combination of currents mediated by different splice variants of the $DmNa_v29$ gen, that is specific to embryonic neurons. Here, we use instantaneous activation of sodium channels for two reasons: first due to the advantage of reducing the model to only two dimensions and second because there are no data for the time course of specific splice variants available.

CHAPTER 3

MORPHOLOGICALLY REALISTIC MULTICOMPARTMENT MODEL

3.1 Introduction

Extensive spatial geometry of dendritic trees can prevent neurons from being electrotonically compact, which affects signal propagation, spatiotemporal synaptic integration and thus, the dynamics of the neuron. It follows that neuronal behavior cannot be captured entirely by single-compartment models. The intrinsic passive electrical properties can be seen as the linear backbone for cellular computation. Although the implementation of active properties will change the computational properties of a neuronal model, it will be influenced by these properties. In this chapter we analyze the properties of passive, morphologically realistic multicompartment models of *Drosophila* MN5. MN5 has a monopolar structure, with a main neurite giving rise to the axon and distinct highly branched dendritic subtrees. Understanding the characteristics of a passive model provides important insight about the neuron dynamics and information processing provided by the dendritic structure. Furthermore, the impact of geometry and passive electrical parameters (the membrane resistance (R_m) , the axial resistance (R_a) and the membrane capacitance (C_m) on signal attenuation and filtering properties will serve as a basis for examining the influence of channel distributions and constraining the model parameters in later chapters.

3.1.1 Electrotonic Structure

Since the membrane is permeable to ions to a certain extent, current flows not only along the dendrite but also through the membrane, leading to a current loss while propagating along the dendrite. In order to assess the degree of coupling or the efficiency between two points of a neuron, usually the SIZ and synaptic input site, it is helpful to express the structure of a dendritic tree in terms of electrotonus. The electrotonic length

L is classically defined as $L = {}^{l}/_{\lambda}$, where l is the physical length and $\lambda = \sqrt{{}^{R_m d}/_{4R_a}}$ is the length constant of an infinite cable. This is because the steady state voltage distribution in an infinite cable is $V_m(x) = V_0 \exp({}^{-x}/_{\lambda})$. In an arbitrary dendritic trees, there are diverse ways to assess electrical distance between two points s and i. One approach to estimate the electrotonic distance is to generalize the definition of electrotonic length by integrating along the direct path from s to i or vice versa , yielding $L_{s,i} = L_{i,s} = \int_s^i \frac{\mathrm{d}x}{\lambda(x)}$, or in the case where the dendritic tree is discretized into cylinders, $L_{i,s} = \sum_i^s \frac{l_i}{\lambda_i}$. However, this measure has no direct relation to the passive spread of charge (electrotonus) in a dendritic tree.

A measure that is often used to describe electrotonus is the voltage attenuation from location i to j, which is defined as $A_{i,\,j} = {}^{V_i}/_{V_j}$ (Rall and Rinzel, 1973). In general $A_{i,j}$ is not identical to $A_{j,i}$, yet it is identical to current attenuation in the opposite direction. Other measures which are sometimes used are the inverse of current and voltage attenuation, which gives voltage and current transfer. Obviously, voltage transfer in one direction is identical to the current transfer in the opposite direction. However, those measures are not suited to visualize the structure of a complex dendritic tree, because the triangle inequality is not fulfilled.

In an infinite cylinder there is a simple exponential relationship between $L_{i,j}$ and $A_{i,j}$. Therefore a pseudo attenuation quasimetric was introduced, by defining electrotonic distance as $\widetilde{L}_{i,j} = \ln(A_{i,j})$ (Zador et al., 1995; Brown et al., 1992). Note that this measure is in general not symmetric but direction dependent; therefore it is a quasimetric. For passive membranes, these measures can be generalized to incorporate the frequency dependence of voltage spread.

3.1.2 Synaptic Efficacy

Signals generated by synaptic input or current injection located on the dendritic tree will decrease along the way to the SIZ. Therefore synapses farther away from the SIZ can have less effect on cell excitability than more proximal synapses. The 'phenomenon' where the effects of a synapse are independent of location has been described as dendritic democracy (Häusser, 2001).

For estimation of synaptic efficacy, current or voltage transfer can be employed. Voltage transfer is the ratio of the change in membrane potential (V_m) at the SIZ and the stimulus location (V_{soma}/V_{syn})) (Carnevale and Johnston, 1982). In contrast, current transfer is the ratio of two measurements at the soma, first in response to a stimulus at the SIZ and second in response to the same stimulus at the synaptic site (Jaffe and Carnevale, 1999). The choice of the measure that is best suited to assess synaptic efficacy depends on whether the synapse acts primarily as a voltage source or approximates a current source.

Often, the maximal conductance of a single synapse is small enough that postsynaptic potentials scale linearly with small changes of the maximal conductance and can be thought of as a current source. In a passive dendritic tree, optimal current transfer occurs if the steady state voltage transfer ratio is proportional to the inverse of R_{in}. Current and voltage transfer are assessed in terms of the maximal steady state responses to a constant stimulus. However, in a linear system those measures are equal to the respective ratios of the time integrals of transient signals. Therefore, if the efficiency of a stimulus is determined by the integral of the depolarization rather then the peak depolarization, then the steady state transfer functions are valid measures for synaptic efficacy. This in turn depends on the voltage dependent membrane dynamics and the underling bifurcation structure that determines AP initiation (see Chapter 2).

3.1.3 Synaptic Input

The electrotonic structure of a neuron provides the basis for synaptic integration and current spread. However, synaptic currents are mediated by local conductance changes for specific ion channels and therefore depend on V_m and the reversal potential (V_{syn}). For this reason, synaptic inputs do not sum linearly. In order to address this issue, synaptic input onto the dendritic tree was modeled.

When considering how cells process synaptic inputs, it is useful to consider two extremes: (i) coincidence detection and (ii) integration of synaptic inputs. MN5 exhibits firing frequencies between 5 and 20 Hz during flight (Gordon and Dickinson, 2006; Dickinson and Tu, 1997). To achieve this through coincidence detection, enough synapses must be activated in a narrow time window to bring V_m beyond the firing threshold. For integration, in contrast, asynchronous and repetitive synaptic input results in a depolarization that induces repetitive firing of the desired frequency.

The spatiotemporal pattern of the synaptic drive of MN5 is not known. However, during behavior, MN5 mostly likely is exposed to multiple cholinergic inputs that may not occur fully synchronized but instead with a temporal jitter. Each input will alter R_{in} locally, possibly resulting in a nonlinear summation of the resulting EPSPs. Experimental studies reveal that cholinergic input is not constrained to particular dendritic subdomains but distributed through most dendrites (Kühn and Duch, 2013). How many synapses are needed to affect V_m in a relevant manner and how sensitive is MN5 to the exact locations of synaptic inputs? To address these questions, passive models were equipped with cholinergic synaptic input.

Table 3.1 Genotype of reconstructions.

genotype	number	color
C380 x w1118	4	
C380 x WT Berlin	2	
D42 x WT Berlin	1	
P103.3 x UAS-Dα7-GFP	1	

3.2 Methods

3.2.1 Experimental Data

All experimental raw data used in this work were provided by the Duch lab. Morphologically realistic multicompartment models were obtained from three-dimensional reconstructions of *Drosophila* MN5s (Vonhoff and Duch, 2010; Duch et al., 2008; Kühn and Duch, 2013) as summarized in Tab. 3.1. The data come from confocal image stacks that were processed with Amira-4.1 software (TGS) and plug-ins to reconstruct dendritic segments (Schmitt et al., 2004; Evers et al., 2005). Electrophysiological data used for the fitting of passive electrical properties were obtained from current clamp recordings from the soma of MN5 (Ryglewski and Duch, 2009). The traces consist of the average of five sweeps during which a current pulse of 0.1 nA was injected for 400 ms. Baseline was estimated by the mean of V_m for the last 50 ms of the recording and subtracted from the data. Data from two cells are used labeled as Dataset 1 and Dataset 2.

3.2.2 Software

Passive multicompartment models from detailed dendritic branching structures of the *Drosophila* MN5 were constructed to characterize the relationship between dendritic

geometry and signal propagation. Simulations of the morphologically realistic multicompartment models were performed using the neuronal simulation environment NEURON (Hines and Carnevale, 2001; Hines and Carnevale, 1997). Geometric reconstructions were imported to NEURON as a Python module (Hines et al., 2009). Since the soma is not spherical and is considered to be isopotential, it was usually not reconstructed. To model the soma, we appended a section that matches the surface area of MN5 of about 900 μm^2 (personal communication Claudia Kuehn). Length and diameter of the soma section was set to 17 μm resulting in a surface area of 908 μm^2.

Software tools were created in Python to refine the hoc-files created with AMIRA (Mercury) (Evers et al., 2005) and to handle the monopolar structure of MNs. These tools allow for the combined analysis of morphological and electrical features with respect to a particular SIZ or subtree. In addition, synaptic input can be placed randomly over the entire structure or restricted to particular areas based on morphological rules or predefined locations. The synaptic locations can then be transferred back to AMIRA for visualization.

3.2.3 Fitting the Model to Electrophysiological Data

To determine the intrinsic passive electrical parameters, namely R_a, R_m and C_m, the voltage response of the different compartmental models were fitted to current clamp electrophysiological data. The electrical parameters are assumed to be uniform across the cell. To produce the best match to the data, the parameters were set using the Brent's Principal Axis (PRAXIS) method, a derivative-free minimization algorithm which is provided in NEURON 7.1. The number of segments was assigned according to the "d_lambda rule" (Hines and Carnevale, 2001), which uses the length constant for a certain frequency. The chosen frequency must be high enough that the transmembrane current is primarily

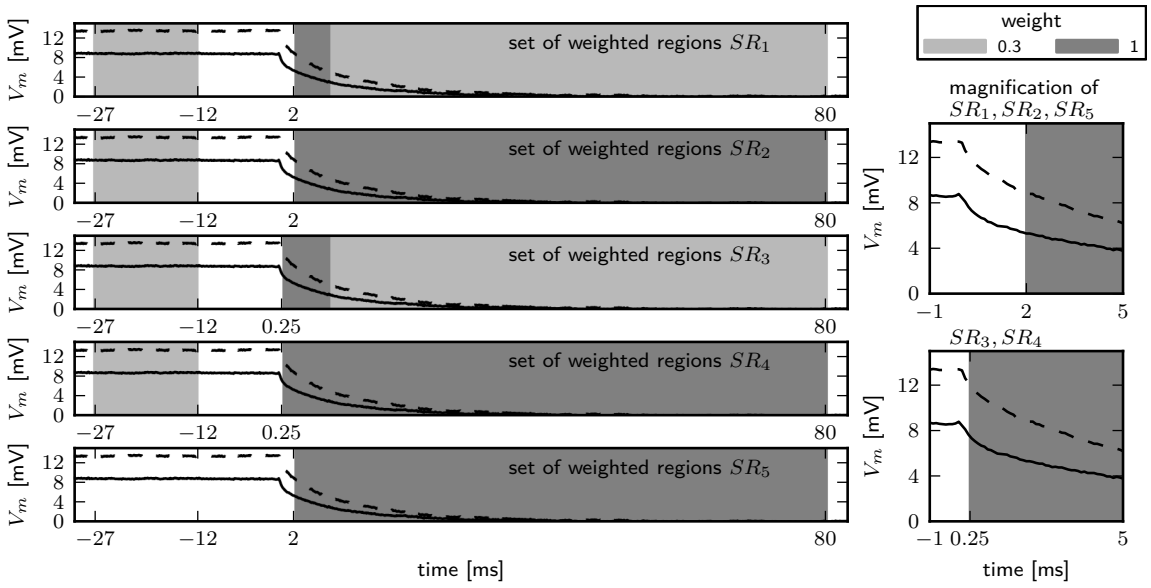

Figure 3.1 Different sets of regions used for fitting of the passive electrical properties. Experimental voltage clamp recordings (Dataset 1 solid lines; Dataset 2 dashed lines). The shaded light and dark grey areas indicate the regions weighted with 0.3 and 1 respectively. Left panels show magnification of the right panels as indicated.

capacitive, so that R_m has little effect on the propagation. We used the default values implemented in NEURON, which is a fraction of 0.1 of the length constant at 100 Hz and has been found to be adequate for membranes with $\tau_m \geq 8$ ms. The length constants were calculated using $R_a = 600\,\Omega$cm, $R_m = 2000\,\Omega\text{cm}^2$, $C_m = 3\,\mu\text{F/cm}^2$, in order to ensure that the electrotonic lengths were shorter than in the final model. Simulations were performed with a fixed time step of 0.01 ms.

For the PRAXIS method, the error function that measures the deviation of the model's predictions from the data points is the weighted sum of the square difference over a number of specified regions, where each is assigned a weight between 0 and 1. The default set of regions (SR_1) consists of three regions, as shown in the top panel in Fig. 3.1. The first region chosen is 15 ms during the depolarized steady state to adjust for the R_{in} and is weighted 0.3. Since it is important to capture the transients of the response, this interval is kept short and is weighted less. The second interval starts 2 ms after the stim-

ulus offset to avoid pipette artifacts (Major et al., 1994) and lasts until 7.25 ms after the offset with an associated weight of 1. This starting point has often been used for passive fitting (Major et al., 1994; Gouwens and Wilson, 2009). The endpoint was set to capture the time of the steepest decay. The last interval directly follows the previous interval and lasts until V_m returns to the clamp potential, from 7.25 to 80 ms after stimulus offset. It is weighted by the factor 0.3 in order to put more emphasize on the interval with the fast time constants, which is more sensitive to R_a. Multiple initial guesses where used to prevent the model from being trapped into local minima; however, all attempts converged to the same values.

3.2.4 Electrotonic Structure

Voltage and current transfer were calculated using NEURON's impedance class, which returns input impedance for a certain location s, transfer impedance between s and all sites on the dendritic tree i, and voltage transfer from i to s for a specific frequency. Here, the frequency was set to zero, which corresponds to constant current injection. To obtain current transfer from i to s, the transfer impedance was divided by the input impedance. This also provides current and voltage transfer in the opposite direction, since voltage transfer from one location to another is the same as current transfer in the opposite direction. $A_{i,j}$ is simply the inverse of voltage transfer. The difference of current transfer in the two opposite directions is defined as the absolute value of the difference. This yields values between 0 %, if the transfer is symmetrical, and 100 % for asymmetric transfer.

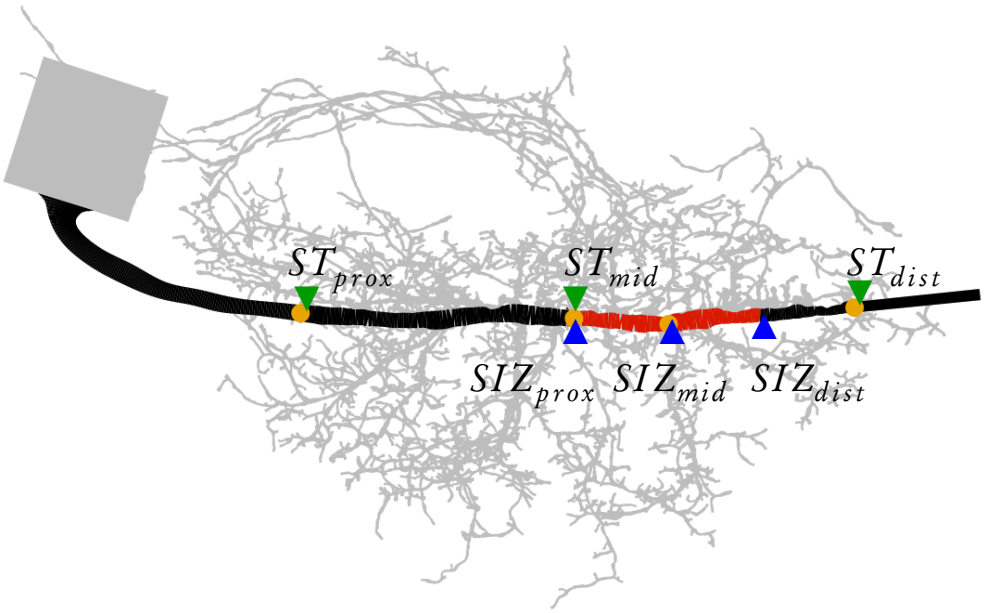

Figure 3.2 Location of reference points. Green and blue triangles indicate locations that are determined by the entire branching part of the primary neurite and by the experimentally predicted location of the SIZ. Region of putative SIZ is depicted in red.

3.2.5 Reference Points

Since the exact location of the SIZ is not known, we chose six different reference locations along the primary neurite for analyses. Three locations were selected according to the positions of the subtrees, and three more were determined by the experimentally predicted putative SIZ (Kühn and Duch, 2013). The first three are the points where the first (ST_{prox}), the last (ST_{dist}), and the middle (ST_{mid}) subtrees branch off the primary neurite with respect to the soma (Fig. 3.2, green triangles). The second set of points are determined using the most posterior dorsal subtree (SIZ_{mid}) and the two points 12 µm distant from this location, proximal (SIZ_{prox}) and distal (SIZ_{dist}) to the soma (Fig. 3.2, blue triangles). In this region a sudden sodium channel increase occurs, therefore it was assumed that the SIZ is located there (Kühn and Duch, 2013).

Table 3.2 Synapse parameters

synapse type	V_{syn} [mV]	τ_{rise} [ms]	τ_{decay} [ms]	$\overline{g}_{syn}$ [µS]
GABA	-85.0	0.3	3.20	3.60×10^{-5}
ACh	-8.9	0.2	1.25	1.21×10^{-4}

3.2.6 Synaptic Input

Models were equipped with either cholinergic or GABAergic synaptic inputs. Synapses were modeled using the Exp2 mechanism of NEURON that describes synaptic conductance changes as a sum of two exponentials, with parameters V_{syn}, rise time (τ_{rise}), decay time (τ_{decay}), and maximum synaptic conductance ($\overline{g}_{syn}$) as summarized in Tab. 3.2. The parameters for cholinergic synapses are based on published data of *Drosophila* central cholinergic synapses (Su and O'Dowd, 2003) and are similar to those previously used in models of central *Drosophila* neurons (Gouwens and Wilson, 2009). GABAergic synapse parameters V_{syn}, τ_{rise}, τ_{decay} are based on data from Su and O'Dowd (2003) and $\overline{g}_{syn}$ on data from Grolleau and Sattelle (2000). The synapses are distributed on the entire dendritic tree or on subtrees revealing a high density of putative GABAergic synapses (Kühn and Duch, 2013). Four different sets of branches where synapses are placed (T_{all}, T_1, T_2 and T_3) are defined as shown in Fig. 3.3. T_{all} consists of the entire dendritic tree. T_1 and T_2 consists of one of two different subtrees close to the putative SIZ. T_3 consists of a subset of branches of the subtree that projects in an arc from the SIZ to the soma. This subset consists of the branches with a distance to the primary neurite greater than 80 % of the longest path of the respective subtree.

The locations of the synapses on T_γ were determined by using a random number generator to pick n uniformly distributed numbers between 0 and L_γ, where n is the number of synapses, $L_\gamma = \sum_{j=1}^{k} l_{\gamma_j}$ is the total length of all branches $B_{\gamma_1} \ldots B_{\gamma_k}$ in T_γ, and l_{γ_j} is the length of of B_{γ_j}. Let P_i be the i-th number and m such that $\sum_{j=1}^{m} l_{\gamma_j} \geqslant P_i > \sum_{j=1}^{m+1} l_{\gamma_j}$,

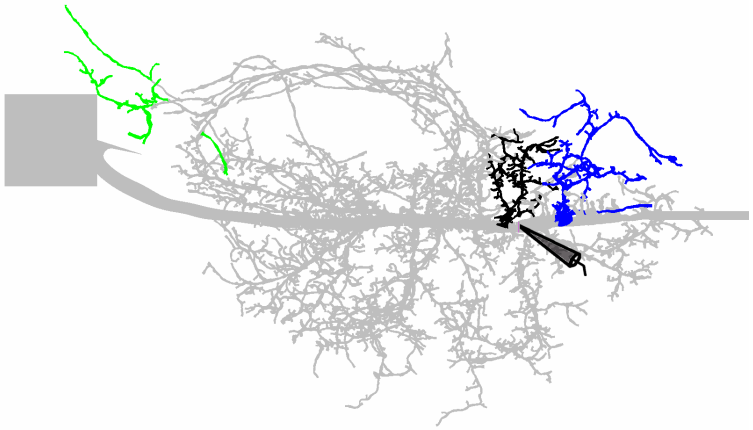

Figure 3.3 Schematic of MN5 model synapse placement. Colors represent the different sets of branches on which synapses are placed: T_1 (blue), T_2 (black) and T_3 (green).

then the p-th synapse is placed on branch B_{γ_m} with distance $P_p - \sum_{j=1}^{m} l_{\gamma_j}$ from the parent branch. From 10 to 5000 synapses were successively activated, either once or repetitively where the onset time of each synapse follows an exponential distribution with the same mean frequency. For single simulation of synapses times for each synapse are chosen from a normal distribution with mean 100 ms. Three different variance (σ^2) values are investigated: 0, 6 and 50 ms^2 (standard deviation (SD) ca. 0, 2.5 and 7.2 ms, respectively). For each T_γ this procedure was repeated with 31 different streams of random seeds for synapse locations.

Simulations with repetitive synapse onset were performed only for cholinergic synapses distributed through T_{all}. From 50 to 500 synapses were activated with the same mean frequency f_{mean} during a simulation. The synapse onsets are determined by the distribution $f_{mean}/N_f \exp(-f_{mean}/N_f(t - I_{fixed})$, where N_f is a noise term that takes numbers between 0 and 1 and determines a fixed interval of $I_{fixed} = {}^{1-N_f}/_{f_{mean}}$ between the spikes. The distribution corresponds to the sum of an exponential distribution with mean duration ${}^{N_f}/_{f_{mean}}$ and a fixed duration of I_{fixed}.

3.3 Results

3.3.1 Passive Electrical Properties

We use two approches to estimate the passive electrical properties. First, we use the experimentally measured values for whole cell capacitance ($127 \pm 16\,\mathrm{pF}$, Ryglewski and Duch, 2009), R_{in} ($97 \pm 31\,\mathrm{M\Omega}$, Duch et al., 2008), τ_m (about 10 ms, personal communication C. Duch). Second, the models are directly fitted to current clamp recordings.

3.3.1.1 Estimates From the Input Resistance at the Soma

First we determine reasonable pairs of R_m and R_a values, because the steady state behavior of a passive cell is independent of the capacitance. In the multicompartment models we vary R_m and R_a over the range of 500 to $30\,000\,\Omega\mathrm{cm}^2$ and 30 to $800\,\Omega\mathrm{cm}$, respectively and measure R_{in}. For a given R_{in}, R_a and R_m are inversely related and increasing either one increases the input resistance, as can be seen by the level lines for R_{in} of 66, 97, 128 and $159\,\mathrm{M\Omega}$ (Fig. 3.4), which correspond to the experimentally observed mean value, one SD above and below and two SD above the mean. Results show a considerable variation between different reconstructions. For a given R_a and $R_{in} = 97\,\mathrm{M\Omega}$, the differences between the extreme values of R_m are about $2000\,\Omega\mathrm{cm}^2$. For a given R_m the values of R_a differ by around $200\,\Omega\mathrm{cm}$. This in turn implies that differences in R_{in} may be due to differences in morphology. Changing the soma area results in a left and right shift when decreasing and increasing the area, respectively (Fig. 3.4).

Taking the surface area and the whole cell capacitance of MN5 into account (values from Ryglewski and Duch, 2009) would result in $C_m \approx 1.5\,\mu\mathrm{F/cm}^2$ in an isopotential cell. For $\tau_m = 9\,\mathrm{ms}$, the value for R_m becomes 6000 ms. These values correspond to those used to model MN5 of *Manduca sexta* (Meseke et al., 2009). The mean and SD of R_a for all reconstructions corresponding to the experimentally observed mean of R_{in} and

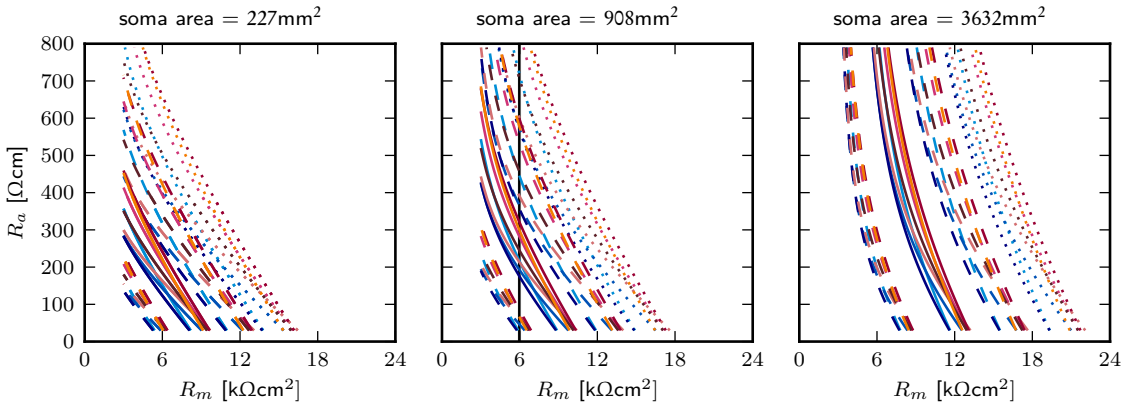

Figure 3.4 R_{in} as function of R_m and R_a. Level lines of input resistances (solid: 97 MΩ; dashed: 66 and 128 MΩ; dotted: 159 MΩ) values for all reconstructions (different colors). From left to right soma area 227, 908 and 3632 μm^2, respectively. Black line in the middle plane indicates the default R_m value.

$R_m = 6000$ ms is 242 ± 49 Ωcm. However, R_a values corresponding to a R_{in} value that is one SD below the mean R_{in} can be smaller than 30 Ωcm. For an R_{in} of one SD above the mean, R_a is 464 ± 88 Ωcm. Most reconstructions must have R_a above 790 Ωcm to exhibit an R_{in} two SDs from the mean. Interestingly, the values between one SD above and below the mean fall exactly into the parameter range that has been reported for various species (Borst and Haag, 1996).

3.3.1.2 Fitting to Experimental Data

The intrinsic passive electrical properties were fitted to experimental data using the NEURON simulation environment. The fitting routine converged to the same data for multiple initial guesses giving the best fit to the data (Fig. 3.5). The voltage response of the different models are very similar. Considering just the regions used for fitting, the residual errors of the models for the first trace and the data appear to be distributed evenly around zero. The fit to the second trace captures the time course between 10 to 50 ms of the experimental data poorly. In both cases, there is a peak directly after stimulus offset, which very likely reflects the pipette artifact. However, due to the large noise in

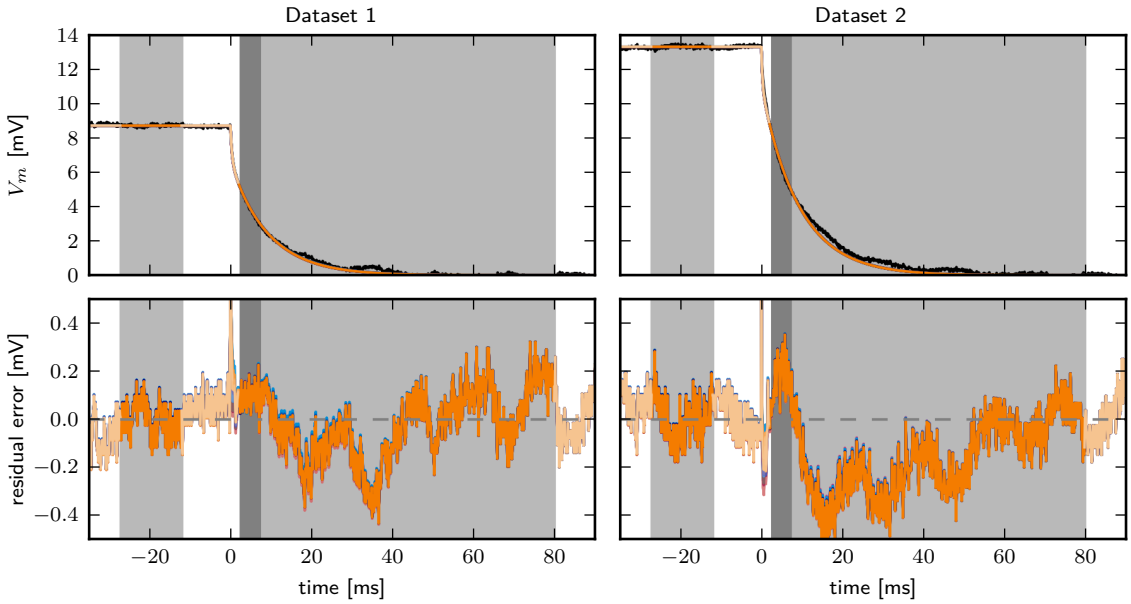

Figure 3.5 Fitting the electrophysiological properties of the models. Top row: membrane potential responses (averages of 5 sweeps, black) of two cells (left and right pannel) to current pulses and the responses of the best fit models (colored lines). Colors represent models corresponding to different reconstructions as in Tab. 3.1. Responses of the different models superimpose so well, that they are not distinguishable. Models were fitted to the set of regions SR_1 as indicated by shaded areas (light and dark grey areas correspond to a weight of 0.3 and 1, respectively). Bottom row: residual error between the data and the model responses.

the recording and since the variance of the traces is not known, further statistical analysis is not feasible.

The results for R_a obtained from fittings to the two different experimental traces show stronger variation between reconstructions then between the two traces, with 121 ± 22 and 130 ± 23, for data sets 1 and 2. (Fig. 3.6, bottom). On the other hand, C_m and R_m show a stronger variation between the two traces than between the reconstructions (Fig. 3.6, top and middle row). The value of R_m is $7024 \pm 439\,\Omega\text{cm}^2$ for the first trace (data set 1) and $11\,735 \pm 706\,\Omega\text{cm}^2$ for the second trace (data set 2). C_m values are $1.35 \pm 0.09\,\mu\text{F/cm}^2$ and $0.80 \pm 0.05\,\mu\text{F/cm}^2$ for the first and second trace. However, R_m and C_m are inversely correlated (coefficient of correlation -0.99), so that the resulting

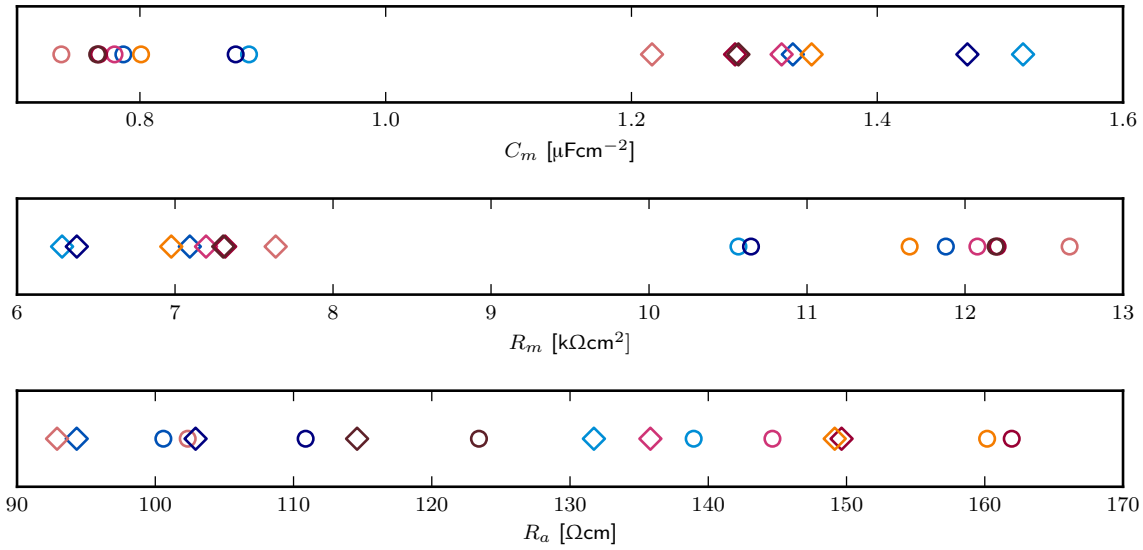

Figure 3.6 Passive membrane parameters as obtained from fits to SR_1 for the two sets of experimental data (Dataset 1: diamonds; Dataset 2: circles). Colors indicate different reconstructions as in Tab. 3.1.

Table 3.3 Labeling for different soma areas and axon lengths and their combinations.

soma area	axon length µm: axon1 ≙ 100	axon2 ≙ 500
soma1 ≙ 908 µm^2	$sa_{1,1}$	$sa_{1,2}$
soma2 ≙ 3632 µm^2	$sa_{2,1}$	$sa_{2,2}$

τ_m is similar for both traces and is between 9.3 to 9.5 ms.

3.3.1.3 Fitting Results under Different Conditions

The fitting procedure has been recast with modified weights and regions as shown in Fig. 3.1. Furthermore, to determine how the results depend on the soma area and axon length, these values were also varied. Four combinations of soma area and axon length were used as summarized in Tab. 3.3. The increase in the axon length resulted in an area change from $379 \pm 64\,\mu m^2$ to $1892 \pm 320\,\mu m^2$. In Fig. 3.7 and Tab. 3.4 the results of all combinations are shown together; all values fall into the physiological range.

Table 3.4 Overview of fitting results of passive electrical parameter. Mean and SD over all reconstructions, as obtained from fits to all chosen set of regions SR_1- SR_5 and all soma/axon combinations of the two sets of experimental data.

parameter	Dataset	soma/axon combination	SR_1	SR_2	SR_3	SR_4	SR_5
C_m [μFcm]	1	$sa_{1,1}$	1.35 ± 0.09	1.46 ± 0.01	1.31 ± 0.11	1.43 ± 0.12	1.62 ± 0.06
		$sa_{1,2}$	1.26 ± 0.09	1.35 ± 0.01	1.21 ± 0.11	1.31 ± 0.12	1.49 ± 0.09
		$sa_{2,1}$	1.14 ± 0.02	1.23 ± 0.03	0.97 ± 0.03	1.06 ± 0.03	1.36 ± 0.07
		$sa_{2,2}$	1.12 ± 0.03	1.18 ± 0.04	0.93 ± 0.03	1.01 ± 0.03	1.33 ± 0.05
	2	$sa_{1,1}$	0.81 ± 0.05	0.92 ± 0.06	0.71 ± 0.05	0.82 ± 0.06	1.14 ± 0.04
		$sa_{1,2}$	0.73 ± 0.05	0.82 ± 0.05	0.64 ± 0.04	0.72 ± 0.05	1.12 ± 0.05
		$sa_{2,1}$	0.98 ± 0.01	0.99 ± 0.01	0.77 ± 0.02	0.85 ± 0.02	1.04 ± 0.04
		$sa_{2,2}$	0.98 ± 0.02	0.98 ± 0.02	0.73 ± 0.02	0.81 ± 0.02	0.99 ± 0.04
R_m [kΩcm]	1	$sa_{1,1}$	7.02 ± 0.44	6.84 ± 0.43	7.13 ± 0.48	6.93 ± 0.47	6.61 ± 0.21
		$sa_{1,2}$	7.74 ± 0.49	7.57 ± 0.48	7.89 ± 0.54	7.68 ± 0.54	7.22 ± 0.34
		$sa_{2,1}$	8.29 ± 0.33	8.03 ± 0.32	8.82 ± 0.39	8.56 ± 0.37	7.93 ± 0.28
		$sa_{2,2}$	8.85 ± 0.36	8.56 ± 0.37	9.52 ± 0.42	9.23 ± 0.41	8.34 ± 0.25
	2	$sa_{1,1}$	11.73 ± 0.71	11.32 ± 0.69	12.31 ± 0.76	11.91 ± 0.76	10.26 ± 0.35
		$sa_{1,2}$	13.13 ± 0.80	12.64 ± 0.76	13.84 ± 0.84	13.35 ± 0.84	10.89 ± 0.39
		$sa_{2,1}$	11.83 ± 0.30	11.80 ± 0.35	13.38 ± 0.51	12.85 ± 0.55	11.71 ± 0.37
		$sa_{2,2}$	12.35 ± 0.33	12.36 ± 0.36	14.48 ± 0.63	13.78 ± 0.60	12.46 ± 0.42
R_a [Ωcm]	1	$sa_{1,1}$	121 ± 21	131 ± 23	117 ± 21	129 ± 23	272 ± 41
		$sa_{1,2}$	114 ± 20	122 ± 21	109 ± 19	119 ± 20	244 ± 52
		$sa_{2,1}$	212 ± 38	233 ± 41	158 ± 28	175 ± 31	214 ± 39
		$sa_{2,2}$	198 ± 34	217 ± 37	147 ± 26	162 ± 28	216 ± 33
	2	$sa_{1,1}$	130 ± 23	152 ± 27	102 ± 18	124 ± 22	498 ± 76
		$sa_{1,2}$	120 ± 20	140 ± 24	93 ± 16	113 ± 20	488 ± 75
		$sa_{2,1}$	403 ± 73	405 ± 71	265 ± 44	305 ± 54	452 ± 74
		$sa_{2,2}$	393 ± 72	392 ± 68	243 ± 42	284 ± 50	430 ± 70

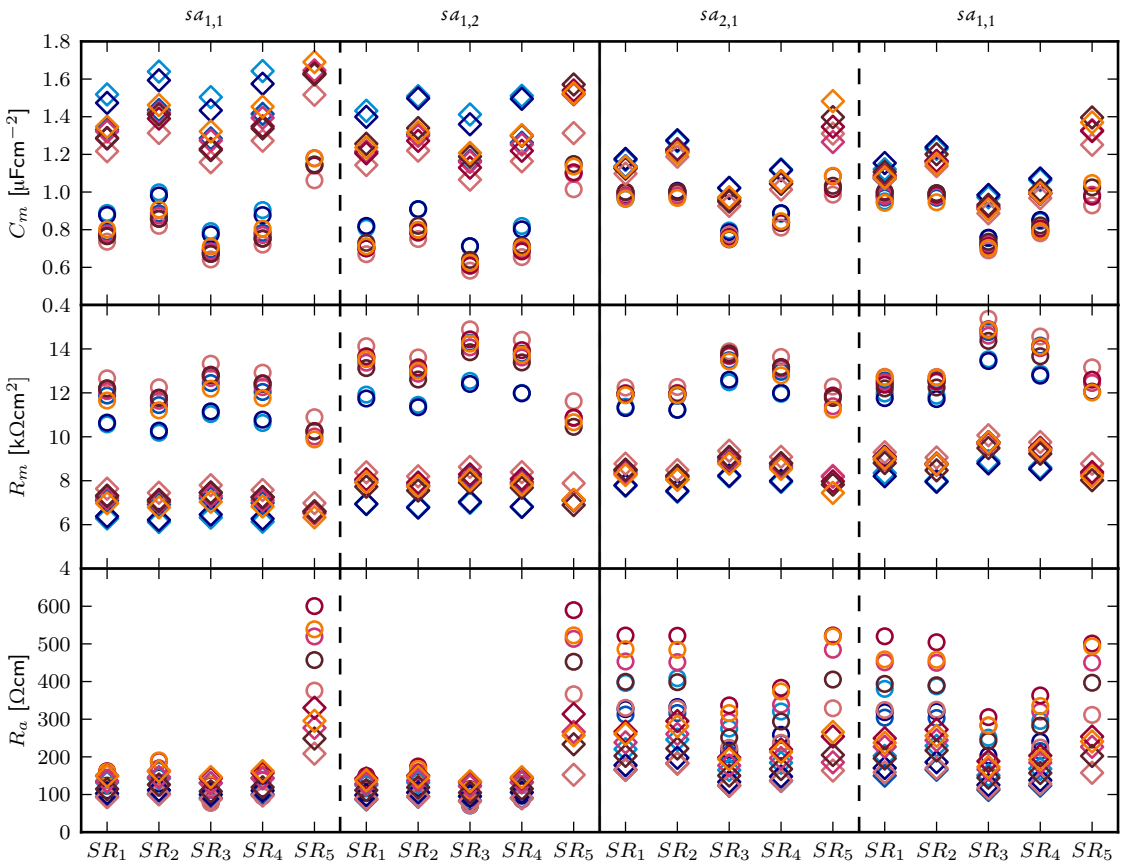

Figure 3.7 Overview of passive electrical parameters as obtained from fits to all chosen SR_i and all soma/axon combinations of the two sets of experimental data (Dataset 1: diamonds; Dataset 2: circles). Colors indicate different reconstructions as in Tab. 3.1.

3.3.1.3.1 Effects of Different Sets of Regions

First the different sets of regions are compared for the default soma area and axon length. The first modification, yielding set of regions SR_2, was to set the weight of the last interval to 1, which results in one single interval after stimulus offset with uniform weights. This makes the choice of a time for the partitioning obsolete, but puts more emphasis on the later response. This led to a slight decrease of R_m and an increase of C_m and R_a in both data sets (Fig. 3.7, left column). Setting the weight of the last interval to 0, which is the same as excluding the interval, leads to bad fits (visually judged) and in non-unique results when using different initial conditions. This choice was not recorded.

Table 3.5 Differences between the results of fittings to the set of regions SR_1 to SR_4

parameter	Dataset	SR_1/SR_2	SR_3/SR_4	SR_1/SR_3	SR_2/SR_4
C_m [µFcm]	1	-7.6 ± 0.5	-8.8 ± 0.2	3.5 ± 1.4	2.1 ± 1.7
	2	-10.9 ± 0.4	-11.4 ± 0.5	13.5 ± 0.8	12.9 ± 1.1
R_m [Ωcm]	1	2.7 ± 0.2	3.0 ± 0.1	-1.5 ± 0.5	-1.2 ± 0.6
	2	3.7 ± 0.2	3.4 ± 0.2	-4.6 ± 0.2	-4.9 ± 0.3
R_a [Ωcm]	1	-7.8 ± 0.6	-9.3 ± 0.3	3.8 ± 1.6	2.1 ± 1.9
	2	-14.7 ± 0.7	-18.3 ± 0.8	27.9 ± 2.1	22.5 ± 2.6

In two further sets (SR_3 and SR_4), the start for the second region was set to 0.25 ms, because Major et al. (1994) found that with optimal capacitance compensation, the electrode artifact disappears within this time. The two sets differ in the weight of the last interval as with SR_1 and SR_2. The weight of the last interval had the same effect on the results as before. The difference between SR_3 and SR_4 is comparable to the difference between SR_1 and SR_2 (Tab. 3.5). The pairs SR_1, SR_3 and SR_2, SR_4, on the other hand, differ only in the start time of the second interval. This change had a similar effect on the results as well (Tab. 3.5). However the differences on the fitting results are small.

We relate the differences of the fitting results between regions to the variability between the reconstructions (Fig. 3.8). For each region the coefficient of variation (CV) was calculated and averaged, resulting in mean CV_{cell} as a measure for the variability between cells. Likewise, for each cell the CV was calculated and averaged, giving CV_{SR} used as a measure of the impact of the regions. Except for R_a of the second data set, the variation between the single reconstructions is higher then between the different SR_i (Tab. 3.6).

In the last set of regions (SR_5), the weight for the first interval was set to 0 in order to exclude this interval completely, and the last interval was weighted by 1. It was only used for a subset of cells. This modification led to an increased C_m as compared to the other SR_i, but had little effect on R_m. The biggest ramification can be observed with regard

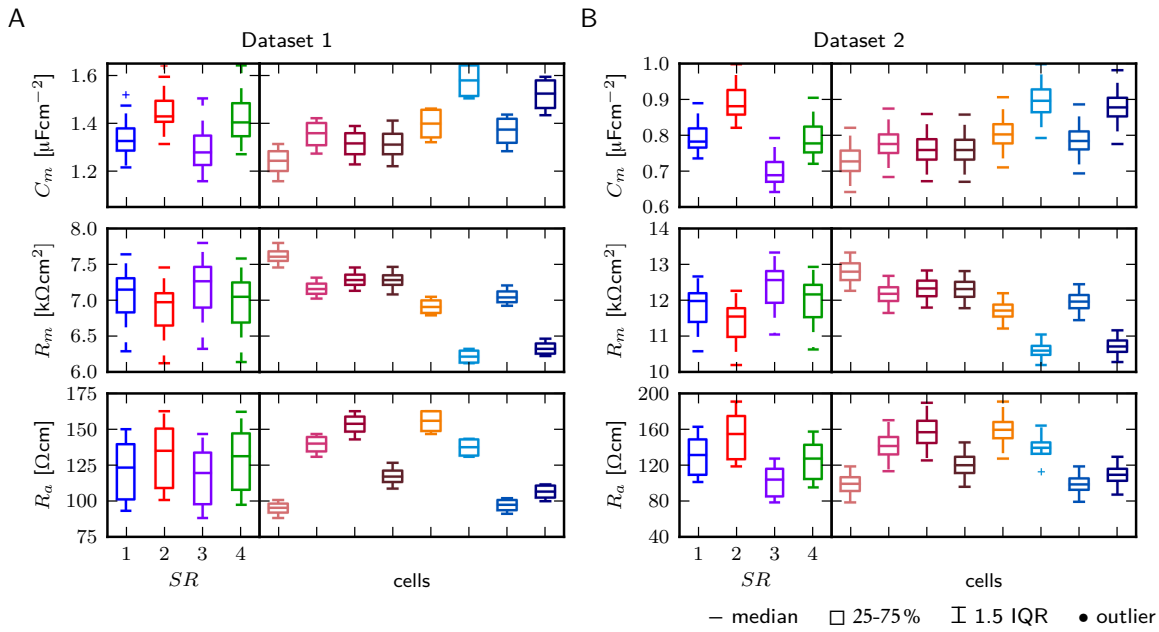

Figure 3.8 Variation between the different reconstructions is higher than between SR_i. For the two data sets (A: Dataset 1; B: Dataset 2) the median and quantiles among the different reconstructions (left part in A and B) and among the different SR_i (right part in A and B) are plotted.

Table 3.6 Average coefficient of variation (CV) of the results for all reconstructions and between SR_1 - SR_4. A ratio above 1 indicates a higher variability between the individual reconstructions than caused by different SR_i and vice versa for a ratio below 1.

		mean CV_{cells}	mean CV_{SR}	mean CV_{SR}/mean CV_{cells}
C_m [µFcm]	1	0.045	0.075	1.657
	2	0.085	0.068	0.801
R_m [Ωcm]	1	0.015	0.065	4.109
	2	0.030	0.062	2.06
R_a [Ωcm]	1	0.048	0.18	3.823
	2	0.142	0.180	1.268

to R_a, where its value more than doubled. For data set 2 the mean is above 400 Ωcm, which is the highest value reported in the literature. If in addition the weight of the last interval was set to 0.3, the fitting procedure returned different results for different initial conditions; the values were not recorded.

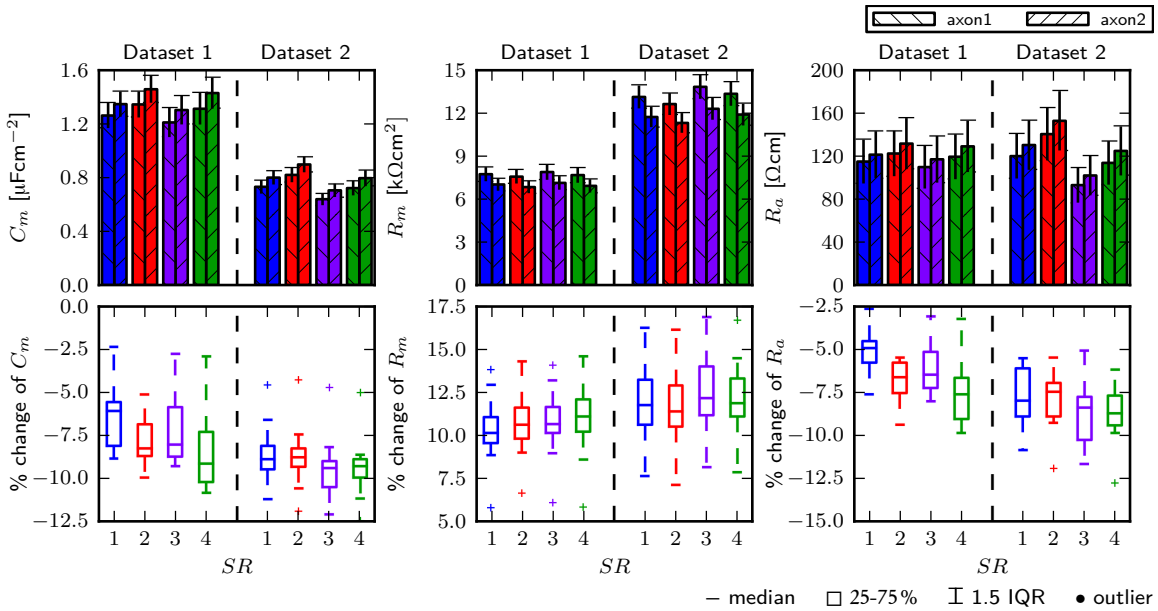

Figure 3.9 Comparison of the resulting passive electrical parameters obtained with two different axon length (axon1 and axon2 are 100 and 500 µm, respectively. Top row mean and standard deviation, bottom row percentual changes due to increasing the axonal length. Different colors indicate different set of regions $SR1$ -SR_4.

3.3.1.3.2 Effect of changing Axon Length and Soma Area

We used an axon length of 100 µm as the axon was reconstructed to this length in most cells. However, the axon of MN5 is longer so the axon length was set to 500 µm by changing the NEURON section parameter L (length of a section) of the axonal section. This causes a change to the 3d-points. Subsequently the length and diameter are updated accordingly. The change in the axon length has a similar effect on fittings to the first and second trace. C_m and R_a decreased by 2.0 to 11.0 %, whereas R_m increased by 6.0 to 16.0 %. Fittings to the different regions SR_1-SR_4 had only a small influence on the results (Fig. 3.9). Since the soma area was not measured in individual cells, we wanted to determine whether soma size affects the fitting results. The area was increased from 908 µm^2 to 3632 µm^2 in order to explore the influence of the soma size. Quadrupling the area is a much higher increase than what is likely to be observed; accordingly the effect should be stronger than the impact of the true soma size on the results. In Fig. 3.10 the

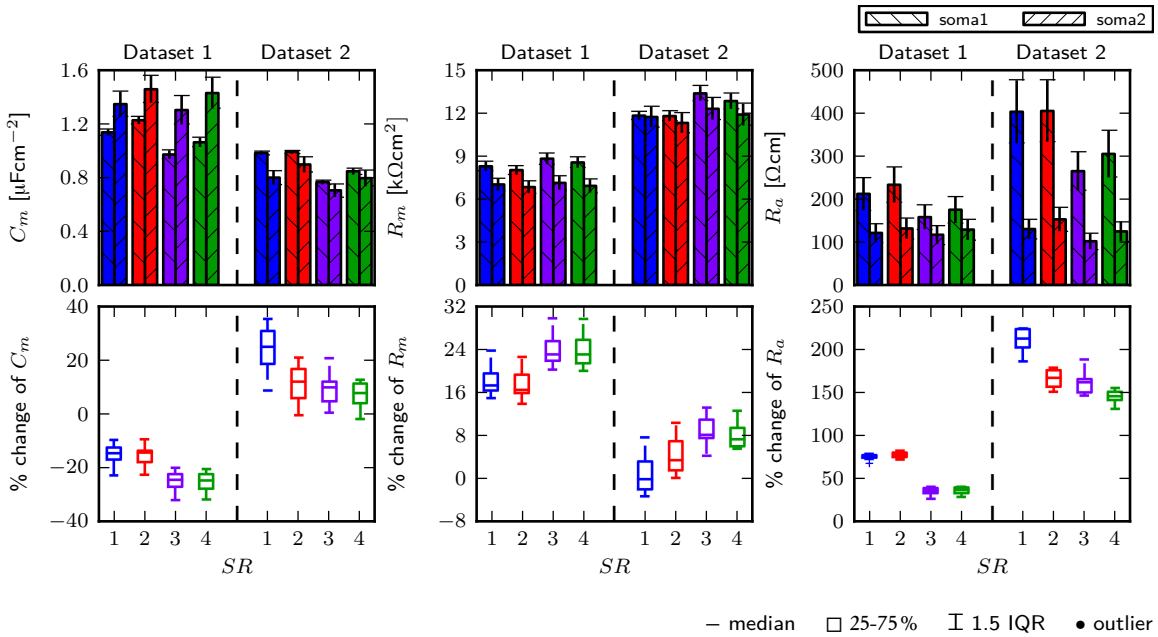

Figure 3.10 Comparison of the resulting passive electrical parameters obtained with two different soma areas (soma1 and soma2 are 908 and 3632 µm^2, respectively). Top row mean and standard deviation, bottom row percentual changes due to increasing the soma area. Different colors indicate different set of regions $SR1$ -SR_4.

effects of changing the soma area on the fittings to the different regions SR_1-SR_4 for both traces are summarized. Fittings to the first trace result in a decrease of C_m by 10 to 23 %, while R_m increases by 15 to 24 %. On the other hand, when fitting the second trace, C_m increases by 15 to 24 % and R_m either increases or decreases, where the change of the value is between −3 and 8 %. The soma area has a stronger influence on R_a. The values increase between 67 and 78 % and 185 to 224 % in the first and second trace, respectively. Fitting to the different regions yield similar results.

3.3.1.3.3 Residual Error Under Different Conditions

In Fig. 3.11 the residual errors of the different axon/soma combinations are overlaid in order to compare the impact of these changes on the fitting error. With the large soma, fitting fails for the early responses for both traces and all SR_i. This indicates that the soma size cannot be set arbitrarily. The residual errors of the fittings with different axon

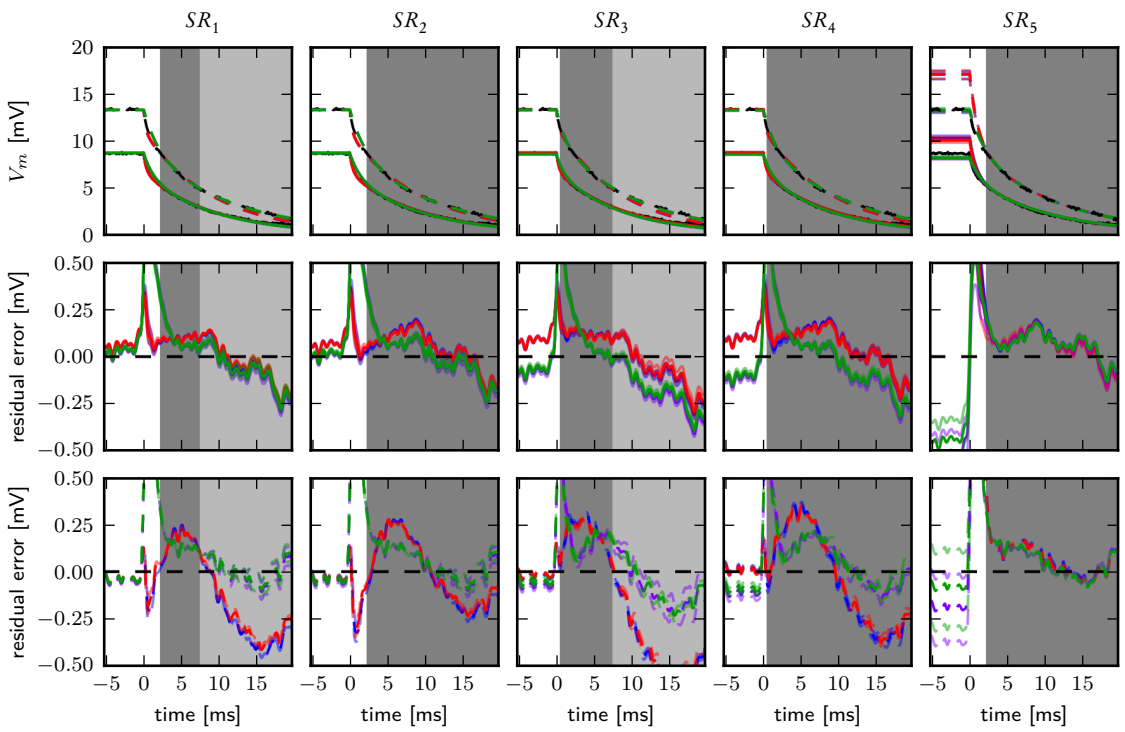

Figure 3.11 Comparison of fitting results for the different SR_i. From left to right results for the regions $SR_1 - SR_5$ are shown. Top row: Membrane potential responses of the two experimental measured traces and the mean, maximum and minimum response of the best fits to the different morphologies are overlayed. Middle and bottom row: residual error of fitting to the first and second trace respectively. The mean of all reconstructions, as well as, the minimum and maximum to show the maximal difference between reconstructions are drawn. Colors represent different soma/axon combinations (as summarized in Tab. 3.3): blue: $sa_{1,1}$; red: $sa_{1,2}$; purple: $sa_{2,1}$; green: $sa_{2,2}$.

lengths differ only slightly for all SR_i and both soma areas. A comparison of the residual error for the different weights is shown in Fig. 3.12. The residual error of the fittings to the regions SR_5 is best, if solely considering the voltage decay. However, the steady state response has a rather large deviation. For the models of the first trace and the reported soma area, the residual errors of the fittings to the other regions SR_1 - SR_4 are similar during the time of the last interval. For the models of the second trace and the regular soma, the residual error falls only in the negative range and is not evenly distributed around zero when fitting to the regions SR_1 - SR_4. On the other hand, contemplating

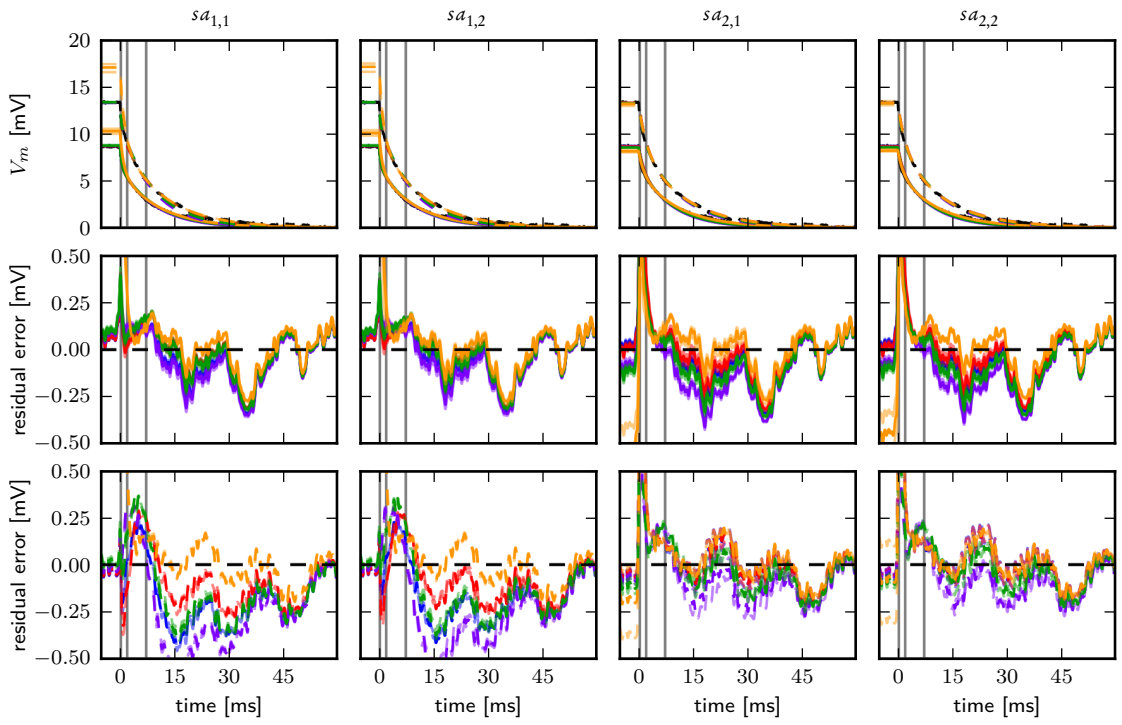

Figure 3.12 Comparison of fitting results for the different axon-soma combinations. From left to right results for the different axon/soma combinations $sa_{i,j}$ are shown (see Tab.). Top row: Membrane potential responses of the two experimental measured traces and the responses mean, maximum and minimum response of the best fits to the different morphologies are overlayed. Middle and bottom row: residual error of fitting to the first and second trace respectively. The mean of all reconstructions as well as the minimum and maximum to show the maximal difference between reconstructions are drawn. Colors represent different weighted fitting regions $SR_1 - SR_5$, red, blue, green, purple, yellow

the large soma, the overall residual error is better for the second trace while it is worse for the first trace as compared to the small soma. However, as mentioned before the models fail to capture the early decay.

3.3.2 Electrotonic Structure

The integration of electrical signals is influenced by dendritic geometry; this influence increases as dendritic branching complexity increases. One question of interest is

whether the complexity of dendritic trees in *Drosophila* influences signal propagation in a significant manner, or instead, are the cells electronically compact since the animal is so small? This same question was asked by Gouwens and Wilson (2009), with the conclusion that at least for olfactory projection neurons, there is considerable attenuation.

3.3.2.1 Contributions of Morphology to Synaptic Efficacy

Previous studies found that several mechanisms can lead to equalization of synaptic efficacy (for reviews see Häusser, 2001; London and Häusser, 2005). In brief, these mechanisms are synaptic scaling (Magee and Cook, 2000), amplification of distal synaptic inputs by voltage-gated channels (Häusser et al., 2000), as well as dendritic morphology (Jaffe and Carnevale, 1999; Poznanski, 1991). Particularly, diameter tapering results in an increase of R_{in} which can contribute to enhanced synaptic efficacy at the SIZ. Analyses of different simplified branching trees, as well as morphologically realistic neurons, reveals that a quadratic diameter tapering and a symmetric branching structure optimize current transfer (Cuntz et al., 2007). Especially, they found that the diameters of terminal branches are independent of branch order.

To determine the tapering of the branching dendritic tree in MN5, the lengths of all paths in the morphological reconstructions were normalized and then averaged. The mean tapering was determined with respect to six different points along the primary neurite and a quadratic function was fitted.

First, ST_{prox}, ST_{mid} and ST_{dist}, the three points taking all the subtrees into account (see Section 3.2.5), were chosen. To assess the goodness of the fit, the sum of squared residuals were compared to the ones for a linear fit, an exponential fit, as well as, to the sum of squared differences between the fitted functions. For all but one cell, either a linear function provided the best fit or the two fitted function showed more resemblance with

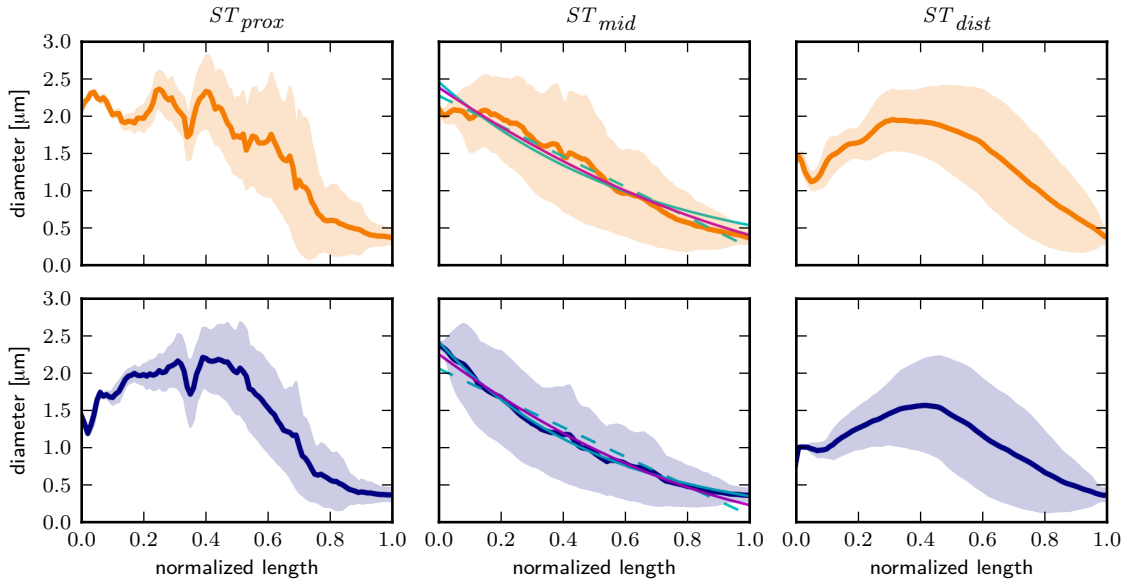

Figure 3.13 Diameter tapering of two reconstructions with respect to different reference points. Thick lines are the average diameter tapering and transparent patch outlines 1 standard deviation from the mean. Colors represent cells as in Tab. 3.1. From left to right the tapering is shown with respect to the location of the first, middle and last subtree. In the middle column, the quadratic (magenta), linear (dashed cyan) and exponential (solid cyan) fits are superimposed. In the top middle panel, the linear function provide the best fit, and in the bottom middle panel the exponential function provides the best fit.

each other than with the data. In the remaining one the exponential function resulted in a better fit when tapering was assessed with respect to the middle point (Fig. 3.13).

Next, SIZ_{prox}, SIZ_{mid} and SIZ_{dist}, the three points determined by the location of the putative SIZ (see Section 3.2.5), were chosen. In three cells the quadratic function provided a better fit when tapering was assessed with respect SIZ_{prox} and in one of these cells the quadratic function provided a better fit with respect to SIZ_{mid} as well (Fig. 3.14).

Cuntz et al. (2007) also examined different binary branching structures and found that the best current transfer was achieved in trees with the most branching, which is a tree where all subtrees are symmetric. The symmetry of a binary tree can be measured with the asymmetry index (Van Pelt et al., 1992). However, *Drosophila* MN5 is not a binary tree and therefore this measure cannot be applied.

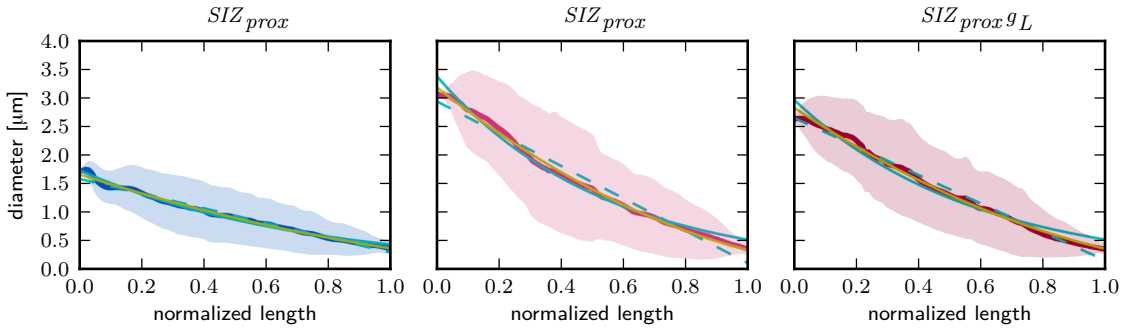

Figure 3.14 Quadratic diameter tapering with respect to SIZ_{prox} is found in 3 cells. Thick lines are the average diameter tapering and transparent patch outlines 1 standard deviation from the mean. Colors represent cells as in Tab. 3.1. The quadratic (yellow), linear (dashed cyan) and exponential (solid cyan) fits are superimposed.

3.3.2.2 Estimation of Synaptic Efficacy From Steady State Behavior

The voltage response at the SIZ to a current injection into each dendrite is independent of the dendritic location if voltage transfer is inversely proportional to R_{in} for each location. If differences in R_{in} through all dendrites vary inversely proportional to the amount of voltage attenuation from every dendrite to the SIZ, then at least in steady state, current injections into each dendrite result in similar depolarizations at the SIZ. Under these circumstances the geometry of the dendritic tree strongly equalize the current transfer from each dendritic location to the SIZ (Cuntz et al., 2007).

To match the R_{in} of the models with the experimentally measured value, we can vary both R_a and R_m. However, the value of R_a is often underestimated (De Schutter, 2002). Therefore we focus on the impact of different R_a values, in order to infer the consequences of choosing an incorrect value. Furthermore, while R_m changes when including active properties and is therefore more likely to be different between animals, R_a is uniform. Additionally, it is tempting to use the values previously used in MN5 models of *Manduca sexta* (Meseke et al., 2009); however, in this work the value R_a was on the lower

end of values obtained by matching the R_{in} of MN5 and of the range that were experimentally observed (Borst and Haag, 1996).

As a first step, we used the same passive electrical properties as previously used in a model of *Manduca sexta* MN5, namely $R_a = 45\,\Omega$cm and $R_m = 6000\,\Omega\text{cm}^2$. Although $Ra = 45\,\Omega$cm is at the lower end of the acceptable parameter space, these values of R_a and R_m result in values of R_{in} at the soma that match experimental data. R_{in}, as well as, voltage and current transfer to the SIZ were assessed in all compartments of the model and plotted for every dendrite as a color code with blue depicting low and red depicting high values (Fig. 3.15A). R_{in} ranged between 40 and 400 MΩ and increased strongly towards distal dendrites (Fig. 3.15A, left). Visual comparison indicates that the distribution of R_{in} mirrors the distribution of voltage transfer (Fig. 3.15A, left and middle) and that the current transfer is between 95 and 100 % (Fig. 3.15A, right). Therefore effective current transfer to the SIZ is similar for all dendritic locations. Quantification reveals a mostly linear relationship between voltage transfer to the SIZ and the inverse of R_{in} for all dendritic locations (Fig. 3.15C, left panel).

Next, we increase R_a to 150 Ωcm, which matches the values derived from the fits to recordings from MN5 very well and is well within the range commonly used in other passive *Drosophila* neuron models (Gouwens and Wilson, 2009). Here, the range of current transfer for most parts of the cell is between 77 to 100 %. The most anterior dendrites, which project in an arch from the SIZ to the cell body (Fig. 3.3), show lower current transfer values (Fig. 3.15B, values between 69 to 77 %). These dendrites are mostly devoid of cholinergic inputs and instead are targeted by GABAergic synapses (Kühn and Duch, 2013). The only other area that consistently showed low densities of cholinergic and high densities of GABAegic inputs across preparations (Fig. 3.3) showed high current transfer values (Fig. 3.15B, values between 92 and 100 %).

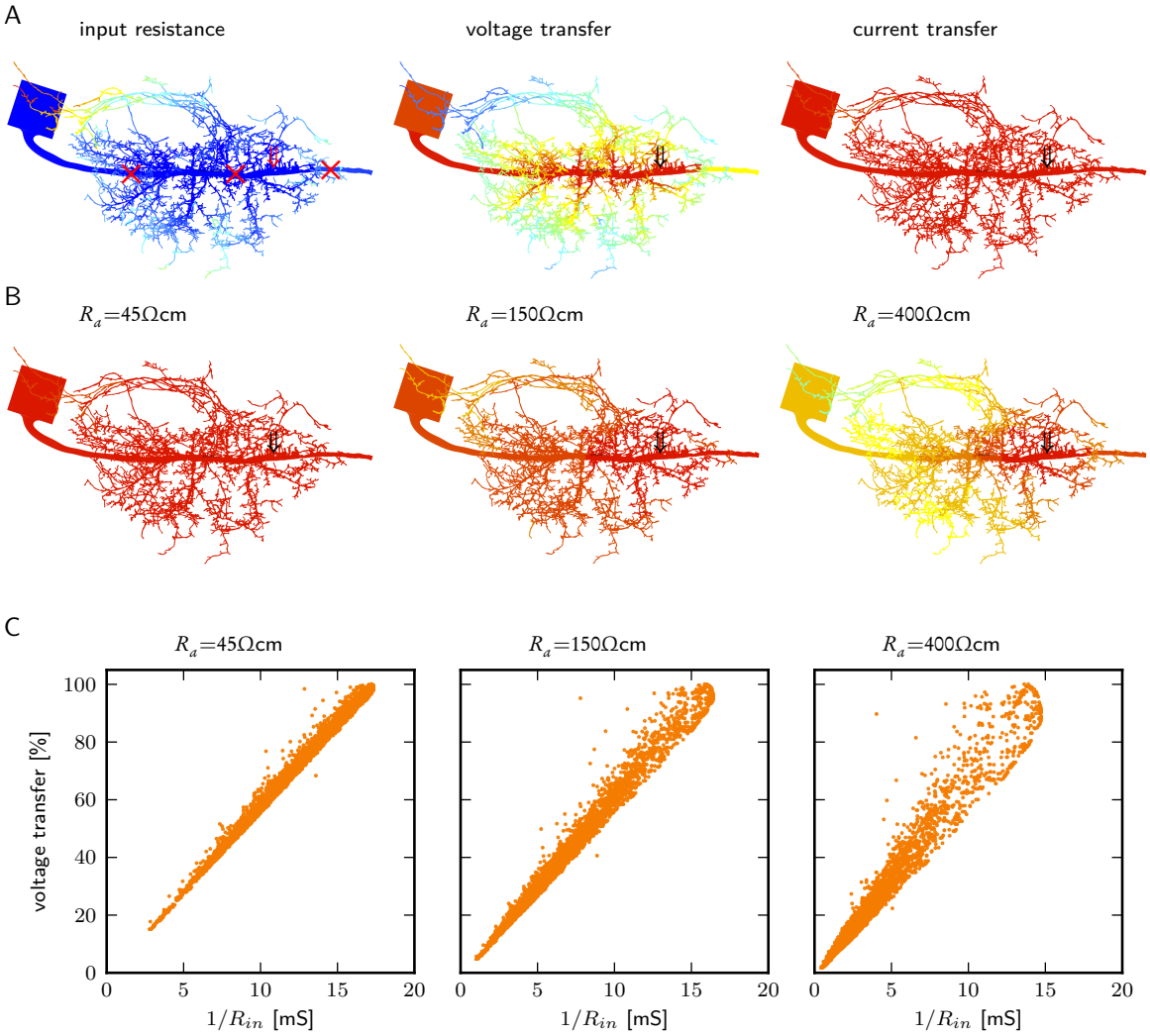

Figure 3.15 Dendritic democracy for small values of R_a is lost when values are increased. A: The local input resistance and the voltage and current transfer to SIZ_{mid} (arrow) are calculated for every dendritic location and mapped onto the dendritic tree of a representative cell using a color code (top row). B: Current transfer to SIZ_{mid} (arrow) for different R_a. C: Voltage transfer to SIZ_{mid} vs the inverse input resistance for respectively 45, 150 and 400 Ωcm from left to right. Each dot represents a branch, where colors indicate different cells.

We cannot exclude the possibility that realistic values for R_a may be higher. Clearly, dendritic democracy is lost when increasing R_a to 400 Ωcm (Fig. 3.15B, C). Current transfer values then range from 38 to 100 % and the relationship between voltage transfer and the inverse of R_{in} shows severe deviations from a straight line.

In order to assess the impact of the location of the SIZ in the different reconstructions, current transfer was calculated with respect to three reference points ST_{prox}, ST_{mid} and ST_{dist} (see Section 3.2.5). Again, R_a was varied with values 45, 150 and 400 Ωcm (Fig. 3.16). With $R_a = 45\,\Omega$cm, voltage transfer and the inverse of R_{in} display a strictly linear relationship for ST_{mid} and a mostly linear relationship for ST_{prox} and ST_{dist}. This indicates a high level of current transfer for all dendrites, independent of the location of the reference point (Fig. 3.16, top row). Using ST_{prox} and ST_{dist} (the two outmost branching points) as reference points and $R_a = 150\,\Omega$cm, dendritic democracy is lost, while voltage transfer and the inverse of R_{in} still display a mostly linear relationship using ST_{mid} as a reference point (Fig. 3.16, middle row). With 400 Ωcm, the linear relationship starts vanishing as well when considering the middle section as a reference point (Fig. 3.16, bottom row). All reconstructions yield qualitatively similar results, although there are differences in the steepness of the curves, revealing overall differences of R_{in}.

In summary, inferring the passive electrical properties from R_{in} and τ_m results in a large range of possible parameters. Assessing the synaptic efficacy over this range of values ranges from a totally democratic dendritic tree, independent of the location of the SIZ, to a dendritic tree that is only democratic for certain SIZ locations. As expected, the impact of the location of the SIZ on the location dependence of the input site increases with increasing R_a. Interestingly, the values for the electrical parameters found with the fitting routine fall within the range in which synapse efficacy begins to be dependent on location for certain sites along the primary neurite and correspondingly, the location of the reference point has a larger impact.

3.3.2.3 Electrotonic Structure Differs Between Reconstructions

Next we compare the electronic structure of the different reconstructions. The passive electrical properties of each cell correspond to the values that were found by the

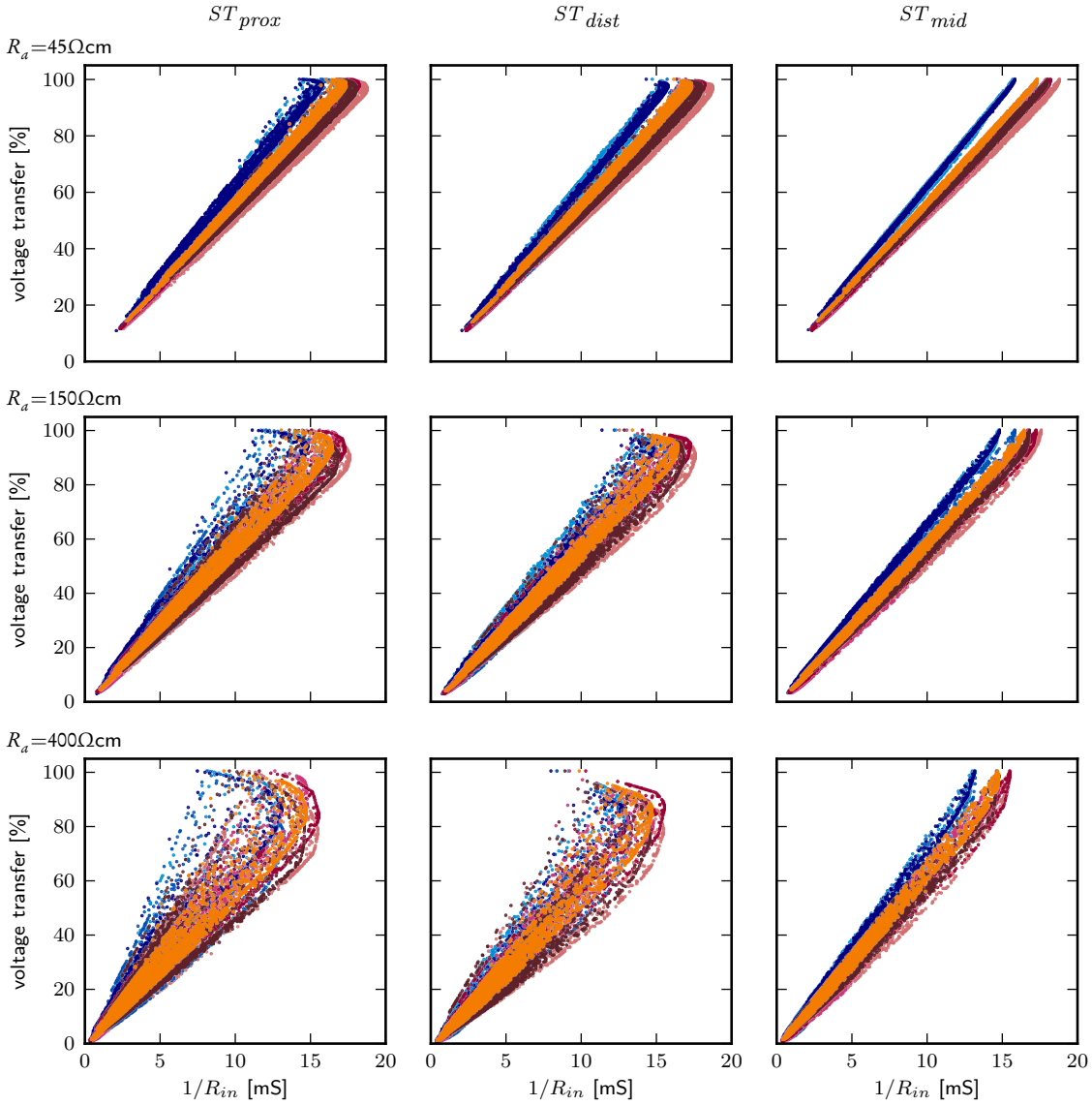

Figure 3.16 Impact of the reference point on dendritic democracy for different R_a. Dendritic democracy is lost at certain reference points when R_a is increased. Voltage transfer vs the inverse input resistance for respectively ST_{prox}, ST_{dist} and ST_{mid} from left to right. From top to bottom R_a is set to 45, 150 and 400 Ωcm, respectively. Each dot represents a branch, where colors indicate different cells.

fitting for the individual cell. Using individual parameters should compensate for some differences resulting from variations in morphology. For every section i, electrotonic distance ($\widetilde{L}_{SIZ_{mid},i}$) was calculated and plotted as a function of physical length (Fig. 3.17A)

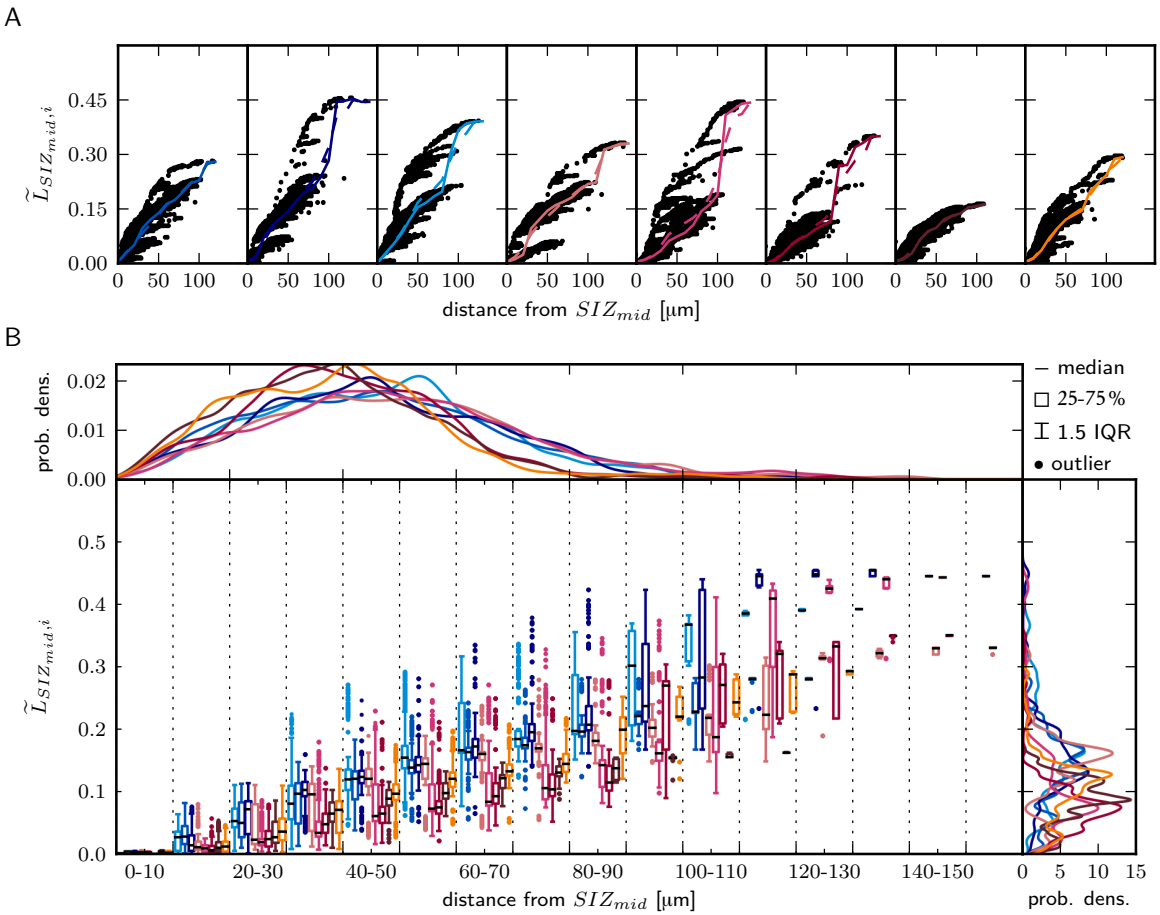

Figure 3.17 Electrotonic distance with respect to physical length. A: Electrotonic distance of individual branches to SIZ_{mid} (black dots) across all reconstruction (from left to right). Colored lines indicate the median (solid) and mean (dashed). B: Juxtaposition of the electrotonic distances binned according to physical distances. At the margins, probability density functions of the electrotonic and physical distance are plotted. Electrotonic distance is evaluated every 0.1 µm and then binned with a width of 10 µm. Colors indicate reconstruction as in Tab. 3.1.

for all reconstructions. Visual comparison reveals some differences between the reconstructions. However, the biggest disparities come from the single subtrees that project from the SIZ back toward the soma (see Fig. 3.15B). Quantification and juxtaposition of the data demonstrates that there are also differences through the entire dendritic trees (Fig. 3.17B). Discrepancies between reconstructions can be seen regarding the variation of the electrotonic distance with respect to physical distance, as well as, considering the

overall probability distribution of the electrotonic distance (Fig. 3.17B, center and right margin). The probability distributions of the physical distance between all locations throughout the dendritic tree and SIZ_{mid}, on the other hand, are quite similar (Fig. 3.17B, top margin).

The putative SIZ is found within a range of 24 µm around the most posterior dorsal subtree (Kühn and Duch, 2013). Within that range the location most proximal to the soma, SIZ_{prox}, is close to ST_{mid}, while the most distal location, SIZ_{dist}, is close to or sometimes even beyond the last subtree, ST_{dist}, with respect to the soma (Fig. 3.18A). The shape of the curves of median electrotonic distance $\widetilde{L}_{SIZ,i}$ as a function of physical distance are, in most reconstructions, different for different locations of the SIZ, as can be seen when superimposing them (Fig. 3.18B). The locations ST_{mid} and SIZ_{prox} are similar in all reconstructions. Only one reconstruction (fifth from left in Fig. 3.18B) shows almost no differences for all four evaluated reference points. In two reconstructions only, SIZ_{dist} is different from the other locations. In the remaining five, both SIZ_{mid} and SIZ_{dist} reveal an increasing slope. Using the values obtained from the fit to data set 2 reduces the electrotonic distance, but the relationship between the curves remains qualitatively similar. Fig. 3.18C shows an overlay of the mean current transfer to the respective reference points for the different reconstructions. The trajectories of $\widetilde{L}_{i,SIZ_{prox}}$ and $\widetilde{L}_{i,SIZ_{mid}}$ are similar in all reconstructions. Moving the location more distally to SIZ_{mid} and SIZ_{dist} reveals an increasing difference between the traces. $\widetilde{L}_{SIZ,terminals}$ follows a unimodal distribution in all reconstructions and for all chosen SIZ locations (Fig. 3.18D). As before the differences between reconstructions decrease when moving the SIZ towards the middle of the primary neurite and the peak of the distribution shifts to smaller values of electrotonic distance. In contrast, the distribution of $\widetilde{L}_{terminal,SIZ}$

for all chosen SIZ locations is similar among reconstructions (Fig. 3.18E). Also, the SIZ location has only a minor impact on the distribution.

3.3.2.4 Electrotonic Structure of the Subtrees

An eye-catching property of MN5, yet rather common in invertebrate neurons, is that the primary neurite gives rise to distinct subtrees. For morphometric analysis, the primary neurite is often collapsed to a point, since the exact location of the SIZ is not known (Meseke et al., 2009; Duch et al., 2008). Furthermore, the individual subtrees of *Drosophila* MN5 have been studied morphometrically (Vonhoff and Duch, 2010).

We ask how current transfer behaves when considering single subtrees. As before, the relationship between voltage transfer and the inverse of R_{in} is assessed as an indication of location independence of current transfer. Different colors are used to represent the different subtrees. Fig. 3.19 shows one representative reconstruction with $R_a = 400\,\Omega\text{cm}$, which is the upper limit of acceptable values. Differences between the single subtrees are revealed. Those are strongest for reference points at the outermost ends of the branching part of the primary neurite, SIZ_{dist} and SIZ_{prox} (Fig. 3.19 left and middle; see Section 3.2.5 for locations), while there are only slight differences between subtrees for SIZ_{mid} (Fig. 3.19 right). However, for all reference points, most subtrees show a strictly linear relationship between voltage transfer and inverse R_{in}. This indicates that, at least for single square pulse current injections into MN5 dendrites, the resulting steady state voltage at the SIZ is independent of the exact input location on a specified subtree. Next we examine the electrotonic structure of the different subtrees in the different reconstructions. In the following, the reference point pn_{ST} for a subset of branches i_{ST} belonging to a certain subtree ST is the location where ST branches off the primary neurite. As Vonhoff and Duch (2010), we exclude small subtrees from the analysis. Here, we consider only the subtrees with a maximum branch order of six resulting in 20 to 29 subtrees

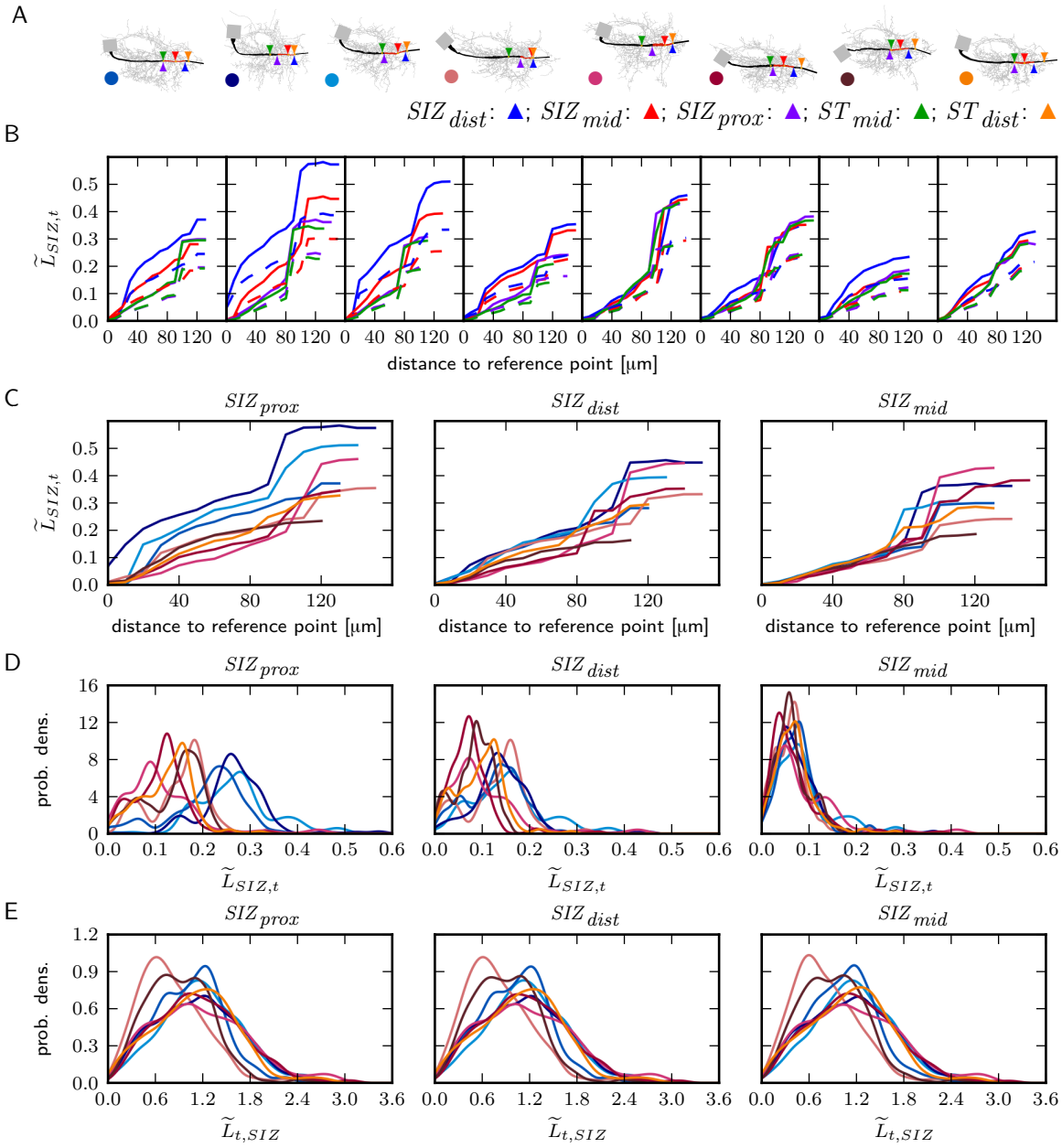

Figure 3.18 Electrotonic distance to different SIZ locations. A: Locations of the SIZ (triangles) in all reconstructions (indicated by colored bullets as in Tab. 3.1). B and C: Medians of electrotonic distance as a function of physical distance to SIZ. Passive membrane parameters from Dataset 1 and 2 (solid and dashed line; left to right different reconstructions). B: Superposition of the functions for different SIZ locations (colors as indicated by triangles in A); from left to right different reconstructions. C: Superposition of the functions for different reconstructions; from left to right different SIZ locations. D and E: Probability density of electrotonic distances between terminals and SIZ locations. Colors in C-E represent reconstructions as indicated by circles in A.

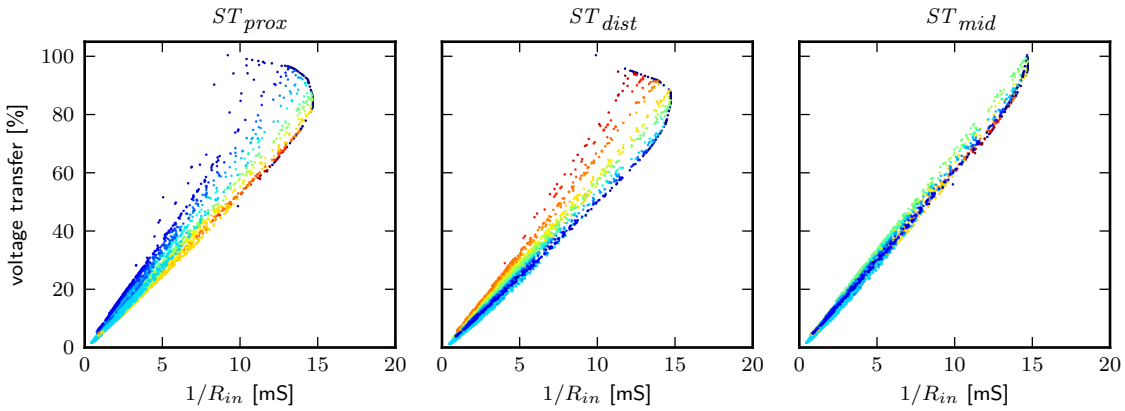

Figure 3.19 Subtrees remain democratic. Different colors represent different subtrees. Voltage transfer vs the inverse input resistance for three reference locations (as in 3.15).

per reconstruction. To compare the reconstructions the distributions of the distances of the longest path per subtree, as well as, the distributions of the mean path length are examined (Fig. 3.20). For four measures, including the three electrotonic measures $L_{pn,t}$, $\widetilde{L}_{pn,t}$ and $\widetilde{L}_{t,pn}$ and the physical distance, the distributions show variations between the reconstructions. The variations in the physical length are in concordance with the results that identified subtrees of different preparations have variable total length and number of branches (Vonhoff and Duch, 2010). The variations also manifest in the distribution of the maximal and mean electrotonic length of the subtrees from different reconstructions.

Note especially that distributions of $\widetilde{L}_{t,\,pn}$ show variability (Fig. 3.20, third column) in contrast to the similarity of the distributions of $\widetilde{L}_{t,SIZ}$ (Fig. 3.18E). In all but one (maroon) reconstruction, the distributions of $\widetilde{L}_{SIZ,t}$ display one subtree that has a considerable larger maximal and mean $\widetilde{L}_{SIZ,t}$ than the other subtrees. The longest path in that subtree is more then twice as long as other subtrees. This corresponds to the subtree that projects in an arch back to the SIZ. In most reconstructions this subtree is the only outlier, with $\widetilde{L}_{SIZ,t}$ >1.5 IQR. $\widetilde{L}_{SIZ,t}$ of the longest path of the remaining subtrees are below 1.8, and the mean path length to terminals is below 0.1. This agrees with the requirements for democratic subtrees.

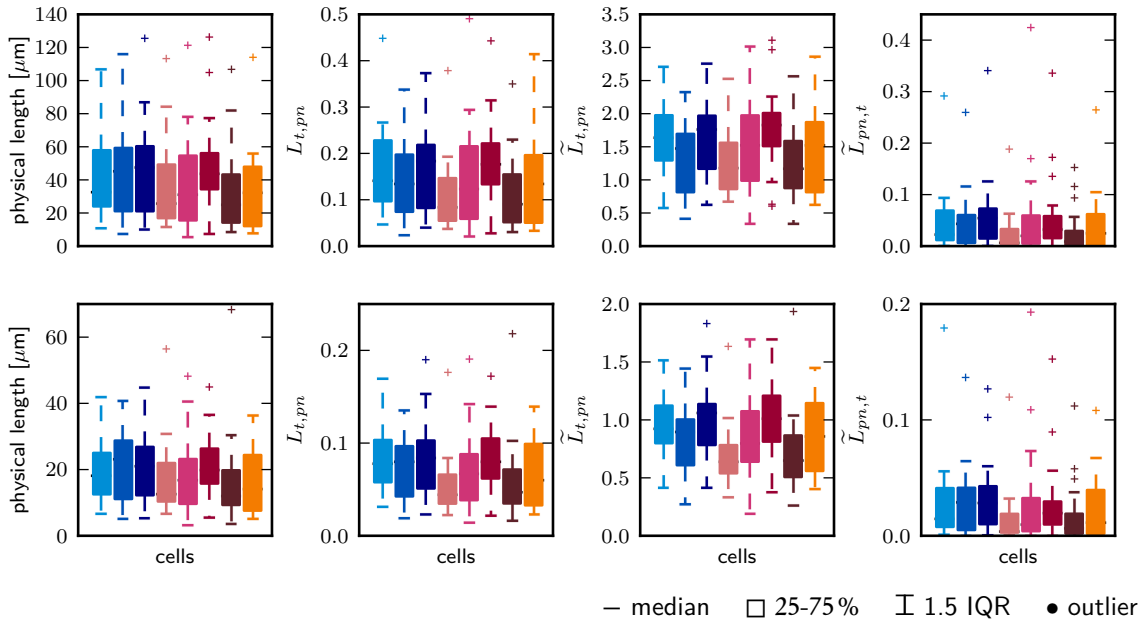

Figure 3.20 Quantification of subtree path length. Distribution of the maximum (top row) and mean (bottom row) path length for each subtree. Path length is assessed as physical length, electrotonic length L, $\widetilde{L}_{t,pn}$ and $\widetilde{L}_{pn,t}$ from left to right. Colors indicate different reconstructions as in Tab. 3.1.

3.3.2.5 Connections Between Subtrees

For input processing, the relationship between dendritic subtrees is of interest. We calculate the current transfer between all pairs of sections and examine four groups comprising pairs belonging to (i) the same subtree, (ii) different subtrees, (iii) the primary neurite and (iv) pairs of dendritic and primary neurite sections. The difference of current transfer in the two directions is assessed (see Section 3.2.4). Fig. 3.21 displays the relative frequencies of current transfer and its difference between section pairs. Sections belonging to the same subtree reveal a strong asymmetry of current transfer, with high values in the direction towards the primary neurite and low values in the opposite direction. Therefore, the frequency plot has two peaks: one at a current transfer of around 20 % and the other at 90 %, with both in the high difference range (Fig. 3.21, left). In contrast, sections from different subtrees cluster at low values of difference and current transfer of

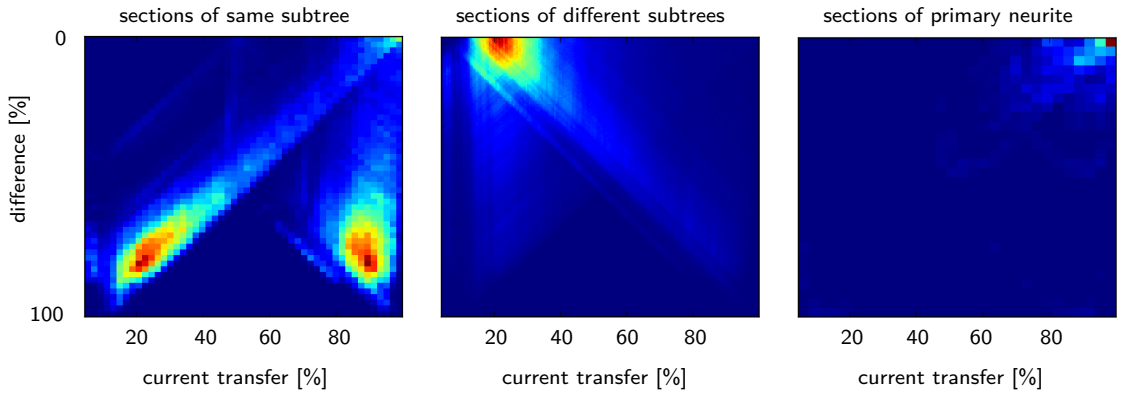

Figure 3.21 Connection strength between pairs of branches. Relative frequency of current transfer and the difference between both directions for branch pairs belonging to the same subtree (left) to different subtrees (middle) and the primary neurite (right). Warmer colors indicate high cooler colors low frequencies.

about 25 % (Fig. 3.21, middle); therefore, current transfer is small in both directions. This indicates that the subtrees are electrically distant from each other and can operate rather independently.

3.3.2.6 Electrotonic Distance Along Primary Neurite

The distribution for the sections of the primary neurite (i_{pn}) peak at high current transfer values with a small difference (Fig. 3.21, right). To further examine how voltage spread along the primary neurite behaves, the electrotonic distance along the primary neurite was assessed. First, we consider the case where each reconstruction has individual passive electrical parameters as obtained from fitting to data set 1 (Fig. 3.22, solid lines). The electrotonic distance $\widetilde{L}_{ST_{dist},i_{pn}}$ is different between reconstructions and varies between 0.15 and 0.32. The biggest differences occur prior to progressing 30 % along the path towards the soma. On the other hand, $\widetilde{L}_{soma,ST_{dist}}$ is similar between reconstructions with values between 0.28 and 0.32. Due to the experimental conditions (electrophysiological data are obtained from the soma), the electrotonic distance $\widetilde{L}_{SIZ,soma}$ is of particular

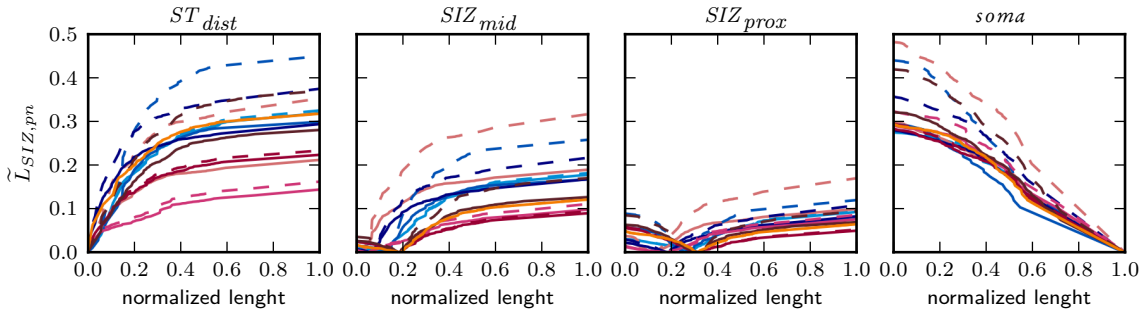

Figure 3.22 Electrotonic distance $\widetilde{L}_{SIZ,i_{pn}}$ as a function of normalized physical length between ST_{dist}=0 and the soma=1. $\widetilde{L}_{SIZ,i_{pn}}$ is assessed from four SIZ locations, from left to right ST_{dist}, SIZ_{mid}, SIZ_{prox}, $soma$. Different sets of passive electrical parameters were used represented by the solid lines (individual parameter for each reconstruction obtained from fitting to Dataset 1) and dashed lines (R_a=150 Ωcm, R_m=7000 Ωcm^2).

interest. SIZ_{mid} is located at 5 to 20% along the primary neurite and $\widetilde{L}_{SIZ_{mid},soma}$ is between 0.1 and 0.2. $\widetilde{L}_{SIZ_{prox},soma}$ is reduced by half, taking values between 0.05 and 0.1 and is at 15 to 30% along the primary neurite.

Using the same electrical parameters for all cells results in larger differences between the reconstructions (Fig. 3.22, dashed lines). Especially, under this condition also $\widetilde{L}_{soma,ST_{dist}}$ varies between reconstructions.

3.3.3 Synaptic Input

To examine how synaptic input is integrated in the passive dendritic tree, one reconstruction was endowed with either cholinergic or GABAergic synapses. (For model parameters see Section 3.2.6.)

3.3.3.1 Single Synchronized Onset of Cholinergic Synapses

We first test whether coinciding synaptic input would be sufficient to drive the cell with a single activation of cholinergic synaptic input. Different numbers of cholinergic input synapses are placed randomly over the entire dendritic tree (T_{all}, see Section 3.2.6

and Fig. 3.3), activated, and the resulting voltage response at the SIZ is recorded (Fig. 3.23A, left, red trace). The amplitude of the postsynaptic potential at the SIZ is analyzed as a function of the number of active synapses. Simultaneous activation of 10 cholinergic synapses causes a maximum depolarization at the SIZ of about 4 mV. The response amplitude increases steeply with the number of activated synapses between 50 and 2000 synapses (Fig. 3.23B, left, red trace). Activation of more than 2000 synapses does not yield much stronger depolarizations at the SIZ, as saturation occurs while approaching the synapse reversal potential of −8.9 mV (Fig. 3.23B, left, red trace). Therefore, in a solely passive MN5 dendritic tree with simultaneous synapse activation, the dynamic range for different depolarization amplitudes at the SIZ is between 50 and 2000 cholinergic inputs. However, the spiking threshold of MN5 is -19.7 ± 10.9 mV, as assessed by current injection measurements (Duch et al., 2008). Between 500 and 1000 cholinergic synapses are required to be simultaneously active in order to depolarize the cell above −30 mV, and between 1000 and 2000 are needed for a depolarization to −20 mV. The exact synapse location does not have much impact on results, as the relative SD (the absolute value of the CV expressed in percent) is 7.9 % with 10 synapses (and a net difference of 0.04 mV) and decreases monotonically to 0.2 % with 5000 synapses (and a net difference of 0.09 mV) (Fig. 3.23B, left, red trace). To assess the time course of the postsynaptic potential at the SIZ, the time to half maximal depolarization, as well as, to the maximal depolarization is analyzed (Fig. 3.23D, left, red trace). Different randomly chosen synapse distributions have no effect on the time course of the postsynaptic potential at the SIZ when all synapses are activated simultaneously.

Next, the placement of cholinergic synapses was limited to single subtrees. (See Section 3.2.6 and Fig. 3.3.) We chose the subtrees that are predominately targeted by GABAergic synapses, because (i) those are close to the putative SIZ and (ii) in order to

compare the results with subsequent simulations using GABAergic synapses. With up to 100 synapses activated simultaneously, the depolarization is larger when the synapses are placed either on T_1 or T_2 when compared to distributions over T_{all}. However, saturation of the voltage response occurs well below $-10\,\mathrm{mV}$ (Fig. 3.23B, left), and with more than 100 synapses, the distributions over T_{all} is more effective (Fig. 3.23C, left). This indicates that the depolarization of the subtree interferes with the synaptic efficacy due to a reduced driving force.

This assumption is further supported by inspecting the change of depolarization with increasing synapse numbers. With up to 50 synapses, the depolarization scales linearly with synapse numbers if they are distributed over the entire dendritic tree. Whereas if the synapses are placed only on subtree 1 or 2 the change of depolarization between 20 and 30 synapses is less than the change between 10 and 20 synapses. Therefore with at least 30 synapses, linearity is not longer given. When distributed over T_{all}, the driving force is not reduced in this manner, because the different subtrees are electrotonically distant from each other (see Fig. 3.21). Even if a fraction of the synaptic locations are electrotonically farther away, they take advantage of the less reduced driving force.

If synapses are distributed over T_3, which is the set of the most anterior branches belonging to the subtree that projects in an arch from the SIZ to the cell body, the amplitude is strongly reduced independent of the number of synapses. This is expected because the electrotonic distance of those locations is high (see Fig. 3.15B).

3.3.3.2 Single De-synchronized Cholinergic Synapse Activation

During normal MN5 operation, it is likely that not all synapses are activated synchronously. Therefore, the simulations were repeated with de-synchronized synapse activation. Incorporating a temporal jitter following a Gaussian distribution with a variance $\sigma^2 = 50\,\mathrm{ms}^2$ yielded smaller and broader depolarization at the SIZ as expected (Fig. 3.23A

and Fig. 3.23B, right). The maximal depolarization is reduced by up to $48 \pm 3\,\%$ with 100 synapses, and more than 2000 cholinergic synapses are required to depolarize the cell above $-30\,\mathrm{mV}$. The different sets of random synapse distributions (Fig. 3.23B) yield only minor differences for higher synapse numbers. For small synapse numbers, differences occur with respect to the time course and the amplitude of the voltage response at the SIZ. However, the observed differences are below 1 mV in amplitude. It remains unclear whether these differences would be of functional relevance for synaptic input integration. In summary, at least in a passive model, the amplitude and shape of postsynaptic potentials at the SIZ are not influenced in a physiological meaningful range by the distribution of cholinergic inputs throughout MN5.

In our simulations with an onset σ^2 of $50\,\mathrm{ms}^2$, no EPSP occurs more than 25 ms before or 50 ms after the mean onset. Therefore repetitive synaptic activation with a mean frequency of up to 13 Hz does not lead to summation of postsynaptic potentials, and background activity is needed.

3.3.3.3 Single Onset of GABAergic Synapses

Next we implement GABAergic synapses. The single onset simulations examine whether there are qualitative differences in the dynamic range and the sensitivity to onset jitter between the two types of synapses. Furthermore, as mentioned previously Kühn and Duch (2013) found specific rules for the distribution of GABAergic synapses on the dendritic tree. The function of synaptic inhibition is usually to regulate excitatory input. In order to account for the depolarization caused by excitatory input, V_m of the model was clamped to $-30\,\mathrm{mV}$ during simulations. Fig. 3.24 shows the results for different random synapse distribution over the branch sets T_{all}, T_1, T_2 and T_3, with synchronized as well as de-synchronized onset. The results are qualitatively similar to those found with

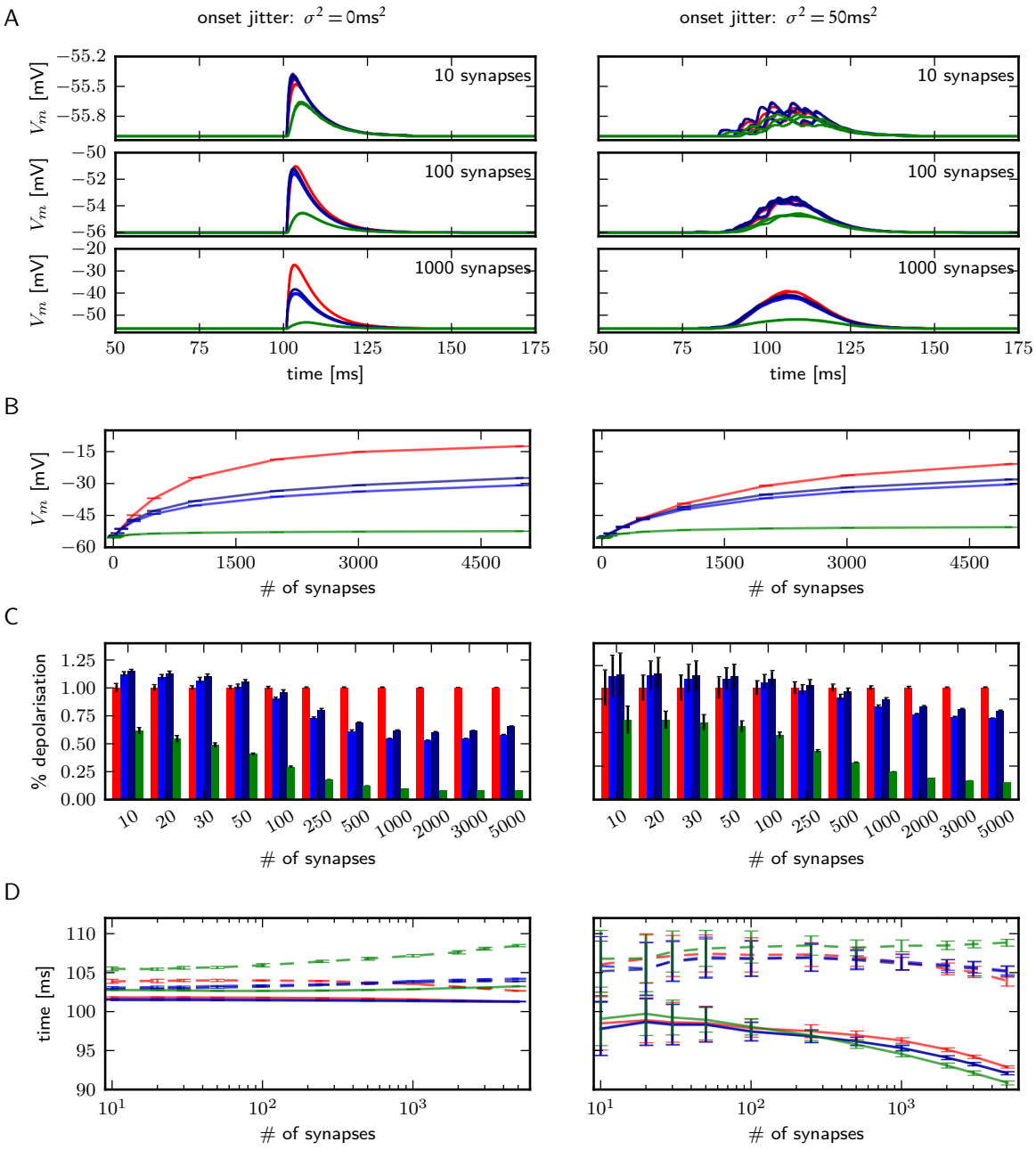

Figure 3.23 Single onset of cholinergic synapses. Left and right panels show results for onset variances of 0 and 50 ms^2, respectively. Synapses were distributed randomly on the branch subsets T_{all} (red), T_1 (blue), T_2 (dark blue) and T_3 (green) (see Fig. 3.3). A: EPSPs from three different seeds per distribution for 10, 100 and 1000 synapses. B: Mean amplitude as function of synapse numbers. C: Amplitude normalized to mean amplitude obtained from synaptic distributions over T_{all}. D: Time to half maximal depolarization (solid) and time to peak of the EPSPs.

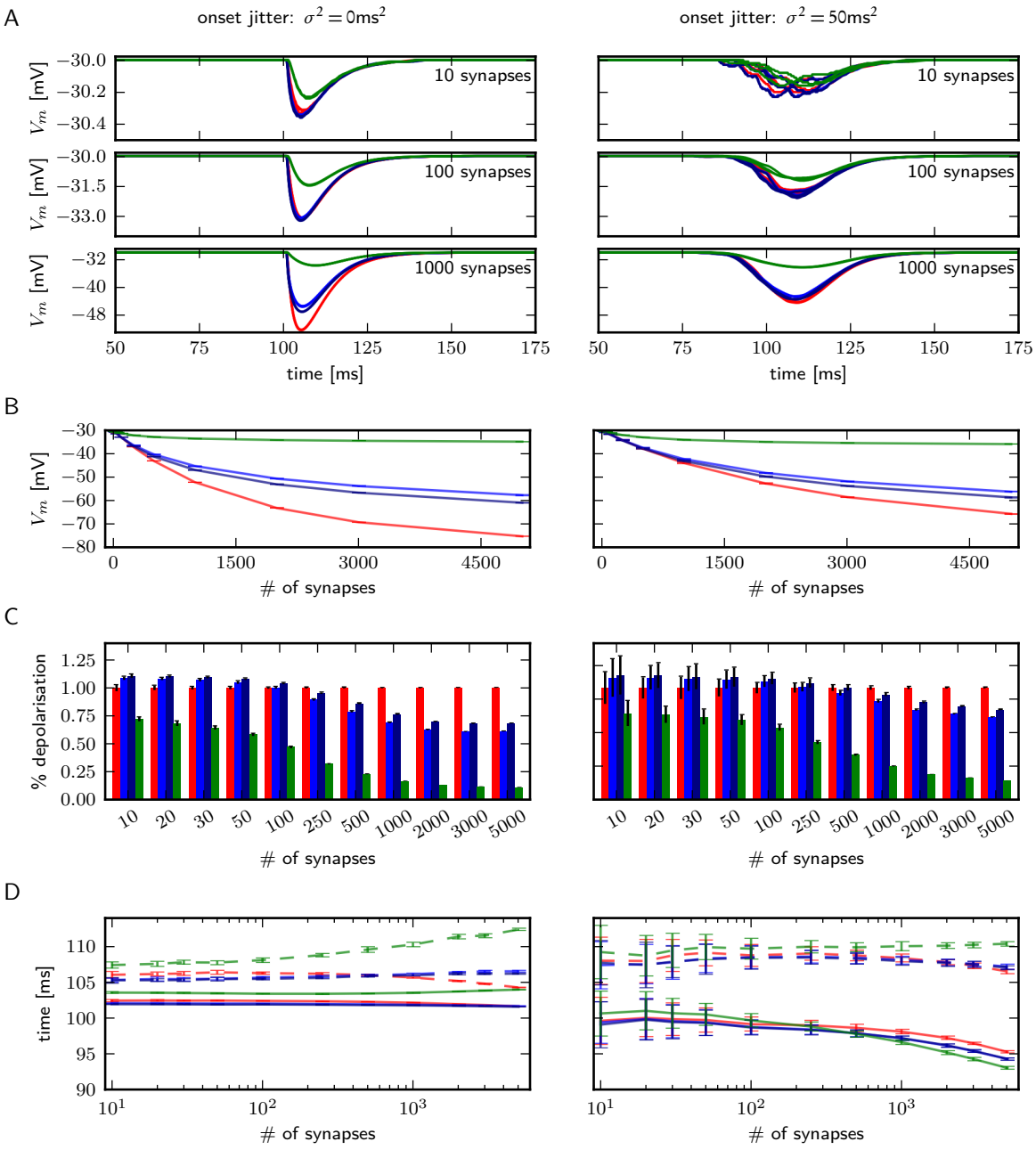

Figure 3.24 Single onset of GABAergic synapses. Left and right panels show results for onset variances of 0 and 50 ms^2, respectively. Synapses were distributed randomly on the branch subsets T_{all} (red), T_1 (blue), T_2 (dark blue) and T_3 (green) (see Fig. 3.3). A: EPSPs from three different seeds per distribution for 10, 100 and 1000 synapses. B: Mean amplitude as function of synapse numbers. C: Amplitude depolarization normalized to mean amplitude obtained from synaptic distributions over T_{all}. D: Time to half maximal depolarization (solid) and time to peak of the EPSPs.

cholinergic synapses (compare with Fig. 3.23), which shows that the specific parameters for the synapses do not have a major impact on the results.

3.3.3.4 Repetitive Onset of Cholinergic Synapses

During behavior synapses are usually activated repetitively. Depending on the ISI this may lead to temporal summation. It is likely that MN5 receives rhythmic input from sensory feedback neurons as well as from the other MNs participating in driving the flight power muscles. The MN firing frequency is between 5 and 20 Hz, while the wing beat frequency is about 200 Hz. Therefore synapses are turned on repetitively with frequencies between 5 and 200 Hz. Fig. 3.25A displays representative traces from two synapse distributions and different numbers of participating synapses (50, 100, 200 and 500). As with the single onset time simulations, the average response amplitude does not depend on the exact synapse locations as the median, the 25th and 75th percentile and the minimum and maximum V_m for the different distributions are similar (Fig. 3.25B).

500 synapses firing repetitively with a mean frequency of 200 Hz are required to bring V_m close to the firing threshold. In contrast, 500 synapses firing with a mean frequency of 5 Hz only induce a mean depolarization of about -55 mV, wich is only slightly higher than the mean depolarization of -56 mV induced by 50 synapses.

3.4 Discussion

In this Chapter, signal propagation and synaptic integration in passive morphologically realistic multicompartment models is analyzed. We use physiologically plausible passive membrane properties, that were estimated by comparing the model to electrophysiological data of MN5. Given those passive electrical parameters the model reveals

a large attenuation from the putative SIZ to the recording site, the soma. This has important implications for interpreting electrophysiological data and should be taken into consideration for the design of future experiments.

3.4.1 Passive Electrical Properties

The two experimentally obtained current clamp traces as well as the parameters obtained for the different reconstructions after fitting the traces reveal considerable variability. These differences can be due to animal-to-animal variations in the morphology, the electrical parameters, or both. It is known that ion channel expression can vary (see Chapter 2), and therefore it is likely that R_m varies. Recent studies also suggest that R_a can be altered by a cell and therefore also varies between cells (Li et al., 2004; Bekkers, 2011). Our results indicate that differences are at least in part due to variations in the electrical properties, because the parameters found for the two different traces differ more than the parameters found for the different reconstructions. Alternatively, the disparities could be a consequence of different soma sizes, which is major uncertainty since the soma is usually not reconstructed. Even a rather drastic increase of the soma size leads to fitting results in physiological ranges, where the influence on R_m and C_m is moderate. Adjusting the soma size in a more anatomically realistic range could possibly account for the differences found between cells. However, large changes in the soma size have a large influence on the mean value and the variability of R_a across reconstructions. The increase in net membrane, as a result of increasing the soma, requires an increase of either R_a or R_m in order to match R_{in}. Our results indicate that the uncertainty of the soma size has a major influence on the correct estimate of R_a. The influence of the soma size needs to be studied in greater detail, ideally in conjunction with experiments. Since it is not feasible to obtain electrophysiological recordings and the three dimensional reconstruction of the

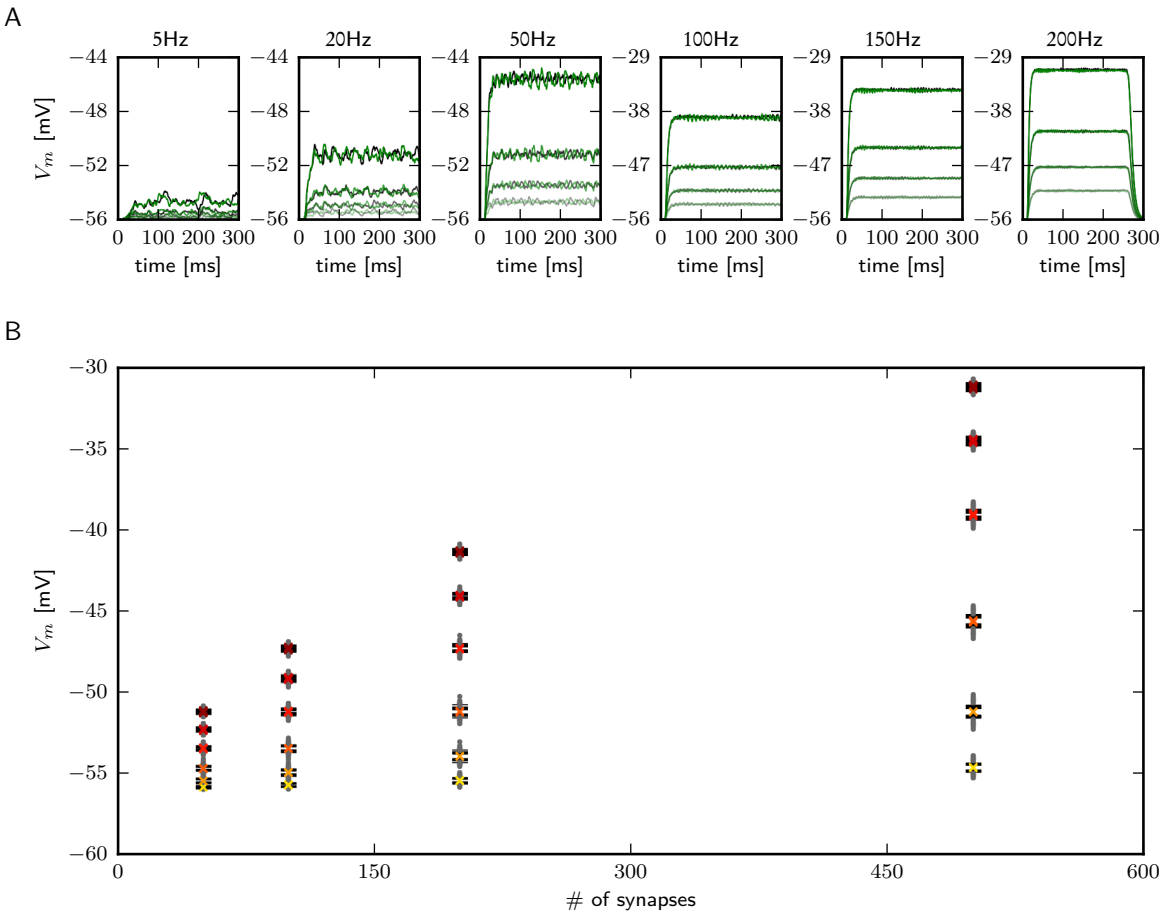

Figure 3.25 Multiple onset of cholinergic synapses. A: Response of two different sets (black and green) of randomly distributed synapses. Responses to repetitive onset of 50, 100, 200 and 500 synapses are indicated by light to dark colors. B: Median (yellow to red crosses for increasing synapse numbers), quantiles (black lines) and minima and maxima (gray dots) for all randomly chosen locations. Values of the different distributions are close and therefore superimpose.

morphology from the same cell, it is necessary to have a good estimate of the soma size from the recorded cell in order to achieve a more accurate estimate of R_a.

3.4.2 Electrotonic Structure

Based on the experimental studies, the range where the SIZ is likely to be located includes a region where the electrotonic structure ranges from rather compact to 'not as

compact'. However compared to other cell types MN5 is still rather compact as judged by electrotonic distance from the SIZ (Mainen et al., 1996; Stuart and Spruston, 1998). On the other hand the electrotonic distance from the dendritic terminals to the SIZ is rather high, as is the distance between the subtrees. Whether voltage attenuation or current transfer is the adequate measure to evaluate synaptic propagation and efficacy depends on whether synapses act more as a current or voltage source. We focus on current transfer since single synapses usually can be approximated by a current source. The simulations of synaptic input support this choice, because for small synapse numbers the response scales nearly linearly. Nonetheless, for larger synapse numbers linearity does not hold and voltage attenuation becomes a better measure to evaluate the impact of many synapses. In fact, the closer the local membrane potential is to V_{syn}, the more the synapse acts as a voltage source.

Different subtrees are electrotonically distant from each other suggesting that the subtrees may be able to act independently from each other. The results obtained with synaptic input support this, since synapse distributions over the entire dendritic tree cause a stronger depolarization than input constrained on a single subtree, even if the subtree is electronically closer to the SIZ than the majority of the other subtrees. This agrees with experimental studies that show that cholinergic input is distributed over the entire dendritic tree (Kühn and Duch, 2013). However, single subtrees are democratic which indicates that the exact synaptic location on a certain subtree does not matter, even though it is rather important on which subtree it is located. This implies that during development, a presynaptic terminal must find the correct subtree but not a specific location on that subtree.

In the direction from the SIZ to dendritic locations, it is useful to consider voltage attenuation, since APs that spread passively into the dendrites have a fixed amplitude.

The voltage attenuation from the primary neurite to the dendritic regions is rather small, which suggests that APs influence dendritic computation in the subtrees. But it has to be noted that we only considere steady state attenuation. To draw more accurate conclusions about broadening and attenuation of the amplitude of backward spreading APs, the frequency dependence of voltage attenuation has to be taken into account.

The soma is rather distant from the rest of the cell. However, since the putative SIZ is not close to the soma, the membrane potential at the soma may not be as important with respect to the computational properties of the cell during behavior. Also the soma has no direct impact on the propagation of synaptic inputs to the SIZ, since it is not on the direct path. However, since electrophysiological recordings are carried out at the soma, the electrotonic distance of the SIZ from and to the soma has an impact on the response properties, and the recordings need to be contemplated with regard to this issue.

3.4.3 Variation of Axial Resistance

From the fitting conditions (see above) and also due to electrophysiological recording conditions (see below), we must consider that the estimate for R_a is not correct. This is why we explore a larger parameter space within the range of values found in other preparations (summarized by Borst and Haag (1996)). In general it has been shown that R_a is more likely to be underestimated (Major et al., 1994). Interestingly, the different subtrees remain democratic even for high values of R_a. The higher R_a, the stronger is the influence of the SIZ on overall transfer properties. While the current transfer with respect to a SIZ location proximal to the soma remains high, the current transfer with respect to a SIZ location distal to the soma reveals strong location dependent differences. In the unlikely case of an overestimation of R_a, the entire neuron is compact. As a consequence,

the independence of different subtrees will be lost and synapses on different subtrees influence each other much more.

3.4.4 Morphological Variability

As many invertebrate neurons *Drosophila* MN5 is individually identifiable. In contrast to other invertebrate neurons, like neurons of the crustacean stomatogastric ganglion that differ strongly in shape (Bucher et al., 2007; Marder, 2011), morphometric analysis of MN5 reveals a rather stereotyped morphology. Yet, there are still differences between animals, and it is not clear to what extent those differences have functional implications. Assigning individual passive parameter values to the different reconstructions results in almost similar responses to current injection at the soma, indicating that adjusting the electrical parameters can adjust for morphological differences at least to a certain extent. Using the individually fitted electrical parameters and assessing voltage attenuation along the primary neurite reveals that attenuation from the soma is similar between reconstructions, while there are differences between reconstructions considering attenuation from all other points along the primary neurite. This points to overfitting of the data, possibly due to a missmatch between the morphology of the reconstructed cells and the cell where the electrophysiological recording was carried out, indicating that morphological differences matter. To further investigate whether differences in morphology have an influence on the electrical behavior, we used individual electrical parameters for each cell. The rationale is that this leads at most to an underestimation of the influence of morphology. Yet, even under these conditions, we found differences between reconstructions. Consequently, variation in morphology cannot be ruled out when analyzing cell-to-cell variability of electrophysiological responses, even if morphometric analysis indicates little differences.

3.4.5 Model Predictions for Synaptic Input During Behavior

The results from simulation of synaptic input indicate that, at least in a passive dendritic tree, some restrictions apply to the spatio-temporal input in order to depolarize MN5 close to the firing threshold. The spiking threshold is barely reached if input is restricted to single trees, even if close to the SIZ. It is advantageous to have more subtrees with synaptic locations electrically farther away from the SIZ, which introduces more 'space' between synapses in order to achieve better summation. This is due to sublinear summation of the PSPs caused by clustering of the synapses (Segev et al., 1995). However, if synapses are placed on T_1 and T_2, small synapse numbers would cause stronger depolarization than distribution over T_{all}. Additional subtrees close to the SIZ could be considered. However it is not very likely that this would increase the depolarization with respect to synapse numbers in a physiological meaningful manner.

Regarding the temporal pattern, we found two ways to bring the cell close to the spiking threshold. One possibility is that some higher frequency synaptic input drives the neuron providing a rather steady depolarization. The high frequency synaptic input could also bring the neuron close to the threshold, with additional low frequency input driving the neuron to firing. Another possible but rather unlikely scenario is that more than 2000-3000 synapses distributed over the entire tree are activated almost simultaneously in order to depolarize the cell enough to induce spiking. However, it is known that voltage dependent channels at dendritic locations have an impact on synaptic integration (reviewed in Häusser et al., 2000). Furthermore the results strongly depend on synaptic parameters.

3.4.6 Inhibition

Our results give no conclusive answer regarding a functional relevance of the observed distribution of inhibitory synapses. Those close to the SIZ potentially induce shunting inhibition by clamping V_m to potentials below spiking threshold (reviewed in Silver, 2010). Yet, the function of inhibitory synapses at the most distal end of the subtree remains in question. Distal inhibitory input is thought to cause relative inhibition. It has been shown that inhibitory synapses may be more efficient in affecting excitatory impact if they do not lie on the direct path between the synapse location and SIZ, but instead are distal from the synapse (Gidon and Segev, 2012). However, in MN5 the inhibitory synapses are predominantly located on different subtrees than the excitatory synapses.

Potential problems with respect to the interpretation may arise from clamping of the membrane potential to mimic depolarization from excitatory input, since it was reported that the majority of putative cholinergic and GABAergic synapses are located on different subtrees (Kühn and Duch, 2013), and we find that the subtrees are electrotonically distant from each other. Hence, it is not clear whether especially the most distal branches comprising T_3 will be depolarized much during normal flight. To gain further insight into the possible functionality of GABAergic synapse location, the combined activation of cholinergic and GABAergic synapses is necessary. However the exclusive activation of only one type of synapse is necessary in order to distinguish between behavior caused by either type of synapse.

3.4.7 Limitations of Fitting

There are several issues that potentially lead to wrong estimates of the electrical properties. The electrophysiological recording conditions have a major impact. The models are fitted to long current pulses. Fits to short current pulses of 0.5 ms are preferable to

steady state responses in non-isopotential cells (Major et al., 1994). Brief current pulses emphasize the high frequency components in the voltage response. Due to the charge redistribution, R_a has a stronger effect on the transient response whereas the steady-state R_{in} is relatively insensitive to the value of R_a (Rall, 1962a). Additionally, the reliability of the steady state R_{in} is restricted as a result of electrode artifacts (Wilson and Park, 1989). Furthermore, only the average of the sweeps was recorded; assessing the variability between sweeps would be important to evaluate the goodness of the fits. No channels blockers were used in the experiments, and the current steps are assumed to be small enough to not open any voltage dependent channels.

In order to reduce the error due to pipette artifacts, a series resistance and capacitor can be included into the model that represents the recording pipette as well as a circuit for its compensation. Preferable, however, is the use of recordings without compensation. Furthermore the external low-pass filtering of the recording setup can be simulated by convolving the model response with an adequate filter kernel. This, however, would be more critical if a current injection protocol with added noise or with other high frequency patterns was used. More accurate model parameters, particularly R_a, can be achieved by simultaneously recording from two locations (Stuart and Spruston, 1998; Roth and Häusser, 2001).

Another problem is incorrect model assumptions. We assume that the passive electrical properties are uniform. Otherwise, it would require constraining additional parameters that determine the location dependent change of the electrical parameters. We use multicompartment models based on core conductor theory. This means the three dimensional structure of a dendrite is reduced to a one dimensional structure under the assumption that radial charge flow is negligible. However, this is not given if the dendrite is not cylindrical.

Finally reconstruction errors have to be considered, including errors in dendritic diameters, omitted small branches and tissue shrinkage that can have a dramatic impact on the electrical parameters (Steuber et al., 2004).

CHAPTER 4

CONTINUUM BRANCH MODEL

4.1 Introduction

Morphologically realistic multicompartment models with a detailed branching structure are not ideal for systematically investigating the contribution of structural properties and membrane nonlinearities to neuronal output properties. Using structurally reduced models allows for a systematic analysis of the impact of geometrical features like diameter, dendritic length, and simple branching patterns in combination with ion channel distributions. In many modeling studies the dendritic tree is represented either by a single compartment or a single cable (Crook et al., 1998; Goldberg et al., 2007; Remme et al., 2009; Remme and Rinzel, 2010) in order to use an analytically treatable model. These formulations cannot account for independently operating branches or subtrees. Here we derive a new cable theoretic model that incorporates branches emerging from the primary neurite by treating the branches as a continuum. The model is an extension of the continuum spine model derived by Baer and Rinzel (1991), and like that model, there is no direct interaction between branches. Instead, all interactions occur through the primary neurite.

In the continuum spine model the interaction between spines and the dendritic base is described with a continuum of spines, where the spines are assumed to be isopotential and connected to the dendrite via a spine stem resistance. Here branches described with the one dimensional cable equation replace the spines. We assume the primary neurite can be represented by a passive cable with uniform diameter and membrane properties, from which dendritic branches emerge with a density $\overline{n}(x)$ per unit electrotonic length.

For a passive membrane, this formulation provides analytic estimates of electrical parameters, such as the input resistance. Transforming the equations to the frequency domain, the steady state response properties to periodic forcing can be accessed, giving the

input impedance and transfer properties like transfer impedance as a measure of filtering properties and the phase shift at different locations.

The output of the model was studied, both analytically and computationally, and compared to a corresponding multicompartment model with equally spaced discrete branches implemented in NEURON (Hines and Carnevale, 2001). We also test the approach by comparing to a morphologically realistic multicompartment model of the Drosophila MN5 implemented in NEURON.

4.2 Methods

4.2.1 Continuum Approach and Cable Equation

In the continuum spine model (Baer and Rinzel, 1991) the interaction between spines and the dendritic base is described with a continuum of spines, where the spines are assumed to be isopotential and connected to the dendrite via a spine stem resistance. Here the spines are replaced by branches described with the one dimensional cable equation. We assume the primary neurite can be represented by a passive cable in x-direction with uniform diameter and membrane properties, from which dendritic branches emerge with a density $\overline{N}(x)$ per unit length Fig. 4.1A. The branches are represented by cylinders that extend in z-direction. We first derive the equations for one type of branches. However, the model can be extended to incorporate multiple branch types with densities $\overline{N}_1(x),\ldots,\overline{N}_k(x)$ per unit length.

In the continuum spine model the connections between the spines and the dendrite are modeled as ohmic resistors R_{SS}. Corresponding to this approach, we model the connection between the primary neurite and the branches as ohmic resistors. However, here we are only interested in the limiting case where the resistance is small ($R_{PB} \equiv \epsilon \to 0$), and the branches become directly connected to the primary neurite Fig. 4.1B. When current

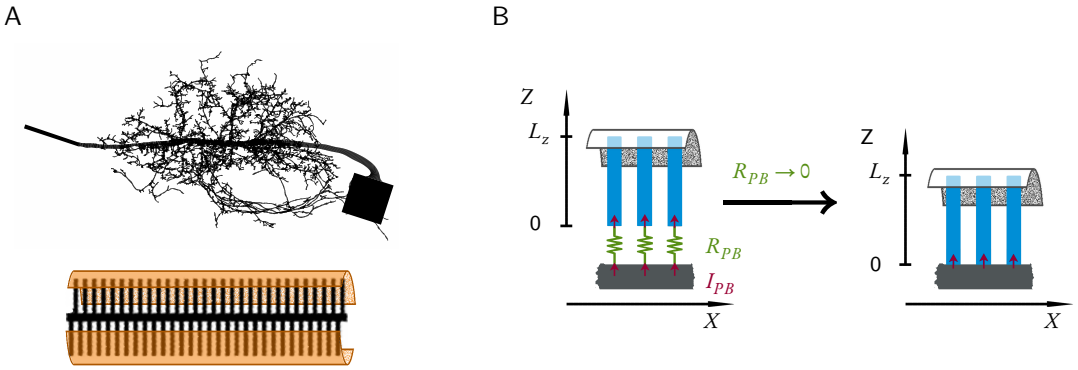

Figure 4.1 Conceptual model development. A: MN5 (top) subtrees emerging from the primary neurite are reduced to cylinders and treated as a continuum of branches indicated by the envelope (bottom). The branches interact only through the primary neurite. B: The model is developed by connecting the branches to the primary neurite via an ohmic resistor R_{PB} (green) and then considering the limiting case by letting $R_{PB} \to 0$.

is injected to one end of the primary neurite, current $I_{PB}(x)$ will flow into the branches. The membrane potential of the primary neurite ($V_P(x,t)$) and the branches ($V_B(x,z,t)$) are based on the cable equation so that

$$\pi d_p C_m \frac{\partial V_p}{\partial t} = \frac{\pi {d_p}^2}{4R_a} \frac{\partial^2 V_p}{\partial x^2} - \frac{\pi d_p}{R_m} V_P(x,t) - \overline{N} I_{PB} - I_{ion_P}(x,t), \tag{17a}$$

$$\pi d_b C_m \frac{\partial V_b}{\partial t} = \frac{\pi {d_b}^2}{4R_a} \frac{\partial^2 V_b}{\partial z^2} - \frac{\pi d_b}{R_m} V_B(x,z,t) - I_{ion_B}(x,z,t). \tag{17b}$$

Here, d_p and d_b are the diameter of the primary neurite and the branches, respectively, x is the location along the primary neurite and z the location along the branches. R_a, R_m and C_m are the membrane resistance, membrane capacitance and axial resistance per unit area. $I_{ion_P}(x,t)$ and $I_{ion_B}(x,z,t)$ are the sum of all membrane currents mediated by voltage-gated ion channels at the respective location ($I_{ion_{loc}} = \sum {}^{\pi d_{loc}}/_{R_i}(V - V_i)$, with $loc = \{P,B\}$) along the primary neurite and the branches.

Multiply both sides by ${}^{R_m}/_{\pi d_p}$ and ${}^{R_m}/_{\pi d_b}$, respectively and let $X = {}^{x}/_{\lambda_p}$, $Z = {}^{z}/_{\lambda_b}$, $T = {}^{t}/_{\tau_m}$, where λ_p, λ_b are the length constants and τ_m the time constant ($\lambda_{loc} = \sqrt{{}^{R_m d_{loc}}/_{4R_a}}, \tau_m = R_m R_a$). Furthermore, let $V_P(x,t) = W(X,T)$, $V_B(x,z,t) =$

$U(X,Z,T)$, $I_{ion_P}(x,t)=J_{VG_P}(X,T)$, $I_{ion_B}(x,z,t)=J_{VG_B}(X,Z,T)$, $I_{PB}(x,t)=J_{PB}(X,T)$. The cable equations can then be rewritten in the dimensionless form

$$\frac{\partial W}{\partial T}=\frac{\partial^2 W}{\partial X^2}-W-\overline{n}R_{P\infty}I_{PB}-\frac{R_m}{\pi d_p}J_{VG_P}, \tag{18a}$$

$$\frac{\partial U}{\partial T}=\frac{\partial^2 U}{\partial Z^2}-U-\frac{R_m}{\pi d_b}J_{VG_B}, \tag{18b}$$

where $R_{P\infty}$ is the input resistance of the primary neurite for the semi-infinite case ($R_{P\infty}={}^{R_m}/_{\pi\lambda_p d_p}=\lambda_p r_{a_p}$), and $\overline{n}(X)$ is the branch density per unit electrotonic length ($\overline{n}(X)=\lambda_p\overline{N}(x)$). Similarly, $R_{B\infty}=\lambda_b r_{a_b}$.

4.2.1.1 Boundary Conditions

In order to obtain unique solutions that satisfy Eqs. (18), boundary conditions are required, which determine the solution at the tips of the primary neurite ($X=0$ or $X=L_x$) and branches ($Z=0$ or $Z=L_z$), respectively. There are several boundary conditions that can be used. The ones that are employed in this study are demonstrated for the primary neurite at $X=0$, if they are the same for both sides, otherwise $X=L_x$ is also shown. If no current is flowing through a tip it is called 'sealed end' boundary condition and

$$\frac{\partial W}{\partial X}(0,T)=0. \tag{19}$$

If a steady current I_{app} is applied at a tip the boundary condition becomes

$$\frac{\partial W}{\partial X}(0,T)=-R_{P\infty}I_{app} \quad \text{or} \quad \frac{\partial W}{\partial X}(L_x,T)=R_{P\infty}I_{app}. \tag{20}$$

If the membrane potential is constant at a value V_{cl} at the tip, the boundary condition becomes

$$W(0,T)=V_{cl}. \tag{21}$$

Further more an attached soma to which a constant current I_{app} is applied can be modeled as boundary condition

$$-R_{P\infty}\frac{\pi d_s^2}{4R_m}\left(W(0,T)+\frac{\partial W}{\partial T}(0,T)\right)+\frac{\partial W}{\partial X}(0,T)=-R_{P\infty}I_{app} \tag{22}$$

4.2.1.2 Steady State Solution

Without the coupling ($I_{PB}\equiv 0$) Eqs. (18) reduce to the regular cable equation. In the case of a passive membrane ($J_{PB}\equiv 0$) and for constant current injection, the membrane potential approaches a new equilibrium for large T ($T\to\infty$); let $\lim_{T\to\infty} W(X,T)=W_{T_\infty}(X)$. The general solution of Eq. (42b) at steady state is

$$W_{T_\infty}(X)=D\cosh(X)+C\sinh(X), \tag{23}$$

D and C are constants that are determined by the boundary conditions.

4.2.2 Fourier Transformation

To analyze the response properties of the passive model in response to periodic stimulation, we use the Fourier transform, which transforms a function $F(x,t)$ from the time domain into the frequency domain,

$$\hat{F}(x,\omega)=\int F(x,t)\exp(-\mathrm{i}\omega t)\,\mathrm{d}t, \tag{24}$$

where $\omega=2\pi f$, with frequency f (in Hz). The amplitude of the resulting complex function $\hat{F}=a+b\mathrm{i}$ is given by its absolute value $|\hat{F}|=\sqrt{a^2+b^2}$, and the phase shift is given by the argument of $\hat{F}$, $\arg(\hat{F})=\arctan(\frac{b}{a})$. For the passive model ($J_{VG_P}\equiv_{VG_B}\equiv 0$), the Fourier transform of Eq. (18) results in ordinary differential equations,

$$\frac{\partial^2\hat{W}}{\partial X^2}=\gamma^2\hat{W}(X,\omega)+\overline{n}R_{P\infty}\hat{I}_{PB}, \tag{25a}$$

$$\frac{\partial^2 U}{\partial Z^2}=\gamma^2\hat{U}, \text{ with } \gamma=\sqrt{\mathrm{i}\omega+1}. \tag{25b}$$

A sinusoidal input current $I_{app} = \sin(at)$ has the Fourier transform $\hat{I}_{app} = -\mathrm{i}\frac{\delta(\omega+\frac{a}{2\pi})-\delta(\omega-\frac{a}{2\pi})}{2}$.

4.2.3 Finite Difference

In order to derive the solutions in the time domain, the equations are integrated using a finite-difference approximation. The center difference approximation to the second derivative of a function f is

$$f'(x_i) \approx \frac{f(x_{i+1}) - f(x_{i-1})}{2\Delta x}, \tag{26}$$

$$f''(x_i) \approx \frac{f(x_{i-1}) - 2f(x_i) + f(x_{i+1})}{(\Delta x)^2}. \tag{27}$$

For a one-sided approximation of $f'(x)$, second order accuracy is used so that

$$f'(x_i) \approx 3x_i - 4x_{i+1} + x_{i+2}. \tag{28}$$

We let $w_i = W(x_i, T)$, $u_{i,j} = U(x_i, z_i, T)$, $I_{PB}(x_i) = i_{pb_i}$, $\overline{n}(x_i) = \overline{\eta}_i$ and $J_{VG_P}(x_i) = i_{VG_i}$ and partition space in n parts of length Δz and m parts of length Δx. Using the above approximation, the cable equations for the branch and the primary neurite Eqs. (18) can be written as

$$\frac{\partial w_i}{\partial T} = \frac{w_{i+1} - 2w_i + w_{i-1}}{\Delta x^2} - w_i - \overline{\eta}_i R_{P\infty} i_{pb_i} - i_{VG_i}, \quad i \in \{0...m\}, \tag{29a}$$

$$\frac{\partial u_{i,j}}{\partial T} = \frac{u_{i,j+1} - 2u_{i,j} + u_{i,j-1}}{\Delta z^2} - u_{i,j}, \quad j \in \{0...n\}. \tag{29b}$$

From the boundary conditions follows

$$w_{-1} = w_1 \tag{30a}$$

$$w_{-1} = 2\Delta x I_{app} R_{P\infty} + w_1 \quad \text{or} \quad w_{n+1} = 2\Delta x I_{app} R_{P\infty} + w_1 \tag{30b}$$

$$w_0 = V_{cl}. \tag{30c}$$

Eqs. (29) can be written in vector form. With boundary conditions Eqs. (30a) or (30b) the vectors $\mathbf{w}$, $\mathbf{bc}_w$, $\mathbf{nipb}$, $\mathbf{ivg} \in \mathbb{R}^{m+1}$ and $\mathbf{u}$, $\mathbf{bc}_{ui} \in \mathbb{R}^{n+1}$ are introduced by setting

$$\begin{aligned} \mathbf{w} &= [w_0, \ldots, w_m]^T, \quad \mathbf{bc}_w = [w_{-1}, 0, \ldots, 0, w_{m+1}]^T, \\ \mathbf{nipb} &= R_{P\infty}[\overline{\eta}_0 i_{pb_o}, ..., \overline{\eta}_i i_{pb_m}]^T, \quad \mathbf{ivg} = [i_{VG_0}, ..., i_{VG_m}], \\ \mathbf{u}_i &= [u_{i,1}, \ldots, u_{i,n}]^T, \quad \mathbf{bc}_{ui} = [u_{i,-1}, 0, \ldots, 0, u_{i,n+1}]^T, \end{aligned} \tag{31}$$

so that

$$\frac{\partial \mathbf{w}}{\partial T} = \frac{1}{\Delta x^2}(\mathbf{A}_{m+1}\mathbf{w} + \mathbf{bc}_w) - \mathbf{w} - \mathbf{nipb} - \mathbf{ivg}, \tag{32a}$$

$$\frac{\partial \mathbf{u}_i}{\partial T} = \frac{1}{\Delta z^2}(\mathbf{A}_{n+1}\mathbf{u}_i + \mathbf{bc}_{ui}) - \mathbf{u}_i, \tag{32b}$$

where $\mathbf{A}_p$ is a the symmetric tridiagonal $p \times p$ matrix of the form

$$\mathbf{A}_p = \begin{pmatrix} -2 & 1 & 0 & \cdots & \cdots & 0 \\ 1 & -2 & 1 & \ddots & & \vdots \\ 0 & \ddots & \ddots & \ddots & \ddots & \vdots \\ \vdots & \ddots & \ddots & \ddots & \ddots & 0 \\ \vdots & & \ddots & 1 & -2 & 1 \\ 0 & \cdots & \cdots & 0 & 1 & -2 \end{pmatrix}.$$

With boundary condition Eq. (30c) the respective endpoint is removed from the vector and the size of $\mathbf{A}_p$ is reduced accordingly.

4.3 Results

4.3.1 Model Development

According to Ohm's Law the longitudinal current into the branches at location X ($I_{PB}(X,T)$) is proportional to the difference between the the potential of the primary

neurite at location X and the potential of the end of the branches ($Z = 0$) that connect to the primary neurite at location X so that

$$I_{PB}(X,T) = \frac{W(X,T) - U(X,0,T)}{\epsilon}. \tag{33}$$

Therefore the rate of change of the potential along the branches at location Z=0 is

$$\frac{\partial U}{\partial Z}(X,0,T) = -R_{B\infty}\frac{W(X,T) - U(X,0,T)}{\epsilon}. \tag{34}$$

For branches attaching directly to the primary neurite, the resistance connecting the branches and the primary neurite approaches 0. Since ϵ appears in the highest order term of Eq. (34), it cannot be well approximated by setting ϵ=0. Therefore for small resistance ($\epsilon \ll 1$), we may seek approximations of U, W and $\frac{\partial U}{\partial Z}$ of the form

$$U = u_0 + \epsilon u_1 + o(\epsilon), \tag{35}$$

$$W = w_0 + \epsilon w_1 + o(\epsilon), \tag{36}$$

$$\frac{\partial U}{\partial Z} = \frac{\partial u_0}{\partial Z} + \epsilon\frac{\partial u_1}{\partial Z} + o(\epsilon). \tag{37}$$

Substituting this into Eqs. (34) and (18a), we get

$$\epsilon\frac{\partial u_0}{\partial Z}(X,0,T) + ... = -R_{B\infty}\left(w_0 - u_0(X,0,T) + \epsilon\left(w_1 - u_1(X,0,T)\right) + ...\right), \tag{38}$$

$$\frac{\partial w_0}{\partial T} + \epsilon\frac{\partial w_1}{\partial T} = \frac{\partial^2 w_0}{\partial X^2} - w_0 - i\,p_0 - \overline{n}(X)\frac{R_{P\infty}}{\epsilon}\left(w_o - u_0(X,0,T)\right) \tag{39}$$

$$+\epsilon\left(\frac{\partial^2 w_1}{\partial X^2} - w_1 - i\,p_1 - \overline{n}\frac{R_{P\infty}}{\epsilon}\left(w_1 - u_1(X,0,T)\right)\right). \tag{40}$$

The first and second order terms of Eq. (38) are

$$O(1): \qquad u_0(X,0,T) = w_0(X,T), \tag{41a}$$

$$O(\epsilon): \qquad \frac{\partial u_0}{\partial Z}(X,0,T) = -R_{B\infty}(w_1(X,T) - u_1(X,0,T)). \tag{41b}$$

Substituting Eqs. (41) into Eq. (40) results in a regular perturbation problem, and neglecting terms involving ϵ yields

$$\frac{\partial w_0}{\partial T} = \frac{\partial^2 w_0}{\partial X^2} - w_0 + \overline{n}\frac{R_{P\infty}}{R_{B\infty}}\frac{\partial u_0}{\partial Z}(X,0,T) - i\,p_0. \tag{42a}$$

$$\frac{\partial u_0}{\partial T} = \frac{\partial^2 u_0}{\partial Z^2} - u_0 - i\,b_0. \tag{42b}$$

It follows that

$$I_{PB}(X,T) \approx -\frac{1}{R_{B\infty}}\frac{\partial u_0}{\partial Z}(X,0,T). \tag{43}$$

4.3.1.1 Boundary Conditions

At $Z = 0$, where the branches are connected to the primary neurite, a current $I_{PB}(X)$ is delivered to or flows out of the branches; the boundary condition is determined by Eq. (41a) . Further, we consider the terminals of the branches (at $Z = L_z$) and the end of the primary neurite (at $X = L_x$) to be 'sealed'and at $X = 0$ a current is applied to the primary neurite. The boundary conditions for the primary neurite and the branches are therefore

$$\frac{\partial w_0}{\partial X}(0,T) = -R_{P\infty} I_{app} \qquad \text{and} \qquad \frac{\partial w_0}{\partial X}(L_x,T) = 0, \tag{44a}$$

$$u_0(X,0,T) = w_0(X,T) \qquad \text{and} \qquad \frac{\partial u_0}{\partial Z}(X,L_z,T) = 0. \tag{44b}$$

4.3.1.2 Passive membrane

In the following, we assume a uniform distribution of branches ($\overline{n}(X)$ is constant) in order to derive analytical solutions. Considering passive membrane properties, analytical solutions can be found for certain scenarios. In this case all voltage dependent ion currents are zero ($I_{ion_B} \equiv 0$; $I_{ion_P} \equiv 0$).

4.3.1.2.1 Steady State Solution to Constant Current Injection

With boundary conditions from Eq. (44b), the steady-state voltage distribution of the branches is

$$u_0(X,Z) = w_0(X)(\cosh(Z) - \tanh(L_z)\sinh(Z)). \tag{45}$$

The first derivative evaluated at $Z = 0$

$$\frac{\partial u_0}{\partial Z}(X,0) = -w_0(X)\tanh(L_z) \tag{46}$$

can now be substituted into Eq. (42a), which gives

$$\frac{\partial^2 w_0}{\partial X^2} = w_0\left(1 + \overline{n}\frac{R_{P\infty}}{R_{B\infty}}\tanh(L_z)\right). \tag{47}$$

With boundary conditions from Eq. (44a), the steady-state voltage distribution of the branches is

$$w_0(X) = I_{app}\frac{R_{P\infty}}{k}\left(\frac{\cosh(kX)}{\tanh(kL_x)} - \sinh(kX)\right), \text{ with } k = \sqrt{1 + \overline{n}\frac{R_{P\infty}}{R_{B\infty}}\tanh(L_z)}. \tag{48}$$

4.3.1.2.2 Transfer Properties

The transformed equations Eqs. (18), from which the transfer properties can be obtained, are solved for the steady state case. With Fourier transformed boundary conditions from Eq. (44b), the steady-state voltage distribution of the branches is

$$\hat{u}_0 = \hat{w}_0\frac{\cosh(\gamma(Z - L_z))}{\cosh(\gamma L_z)}. \tag{49a}$$

Again, the first derivative evaluated at Z=0,

$$\frac{\partial \hat{u}_0}{\partial Z}(X,0,T) = -\hat{w}_0(X,T)\gamma\tanh(\gamma L_z), \tag{50}$$

is substituted into Eq. (42a), which gives

$$\frac{\partial^2 \hat{w}_0}{\partial X^2} = \eta\hat{w}_0, \text{ with } \eta = \sqrt{\gamma^2 + \overline{n}\frac{R_{P\infty}}{R_{B\infty}}\ \gamma\ \tanh(\gamma L_z)}. \tag{51}$$

Applying the Fourier transformed boundary condition from Eq. (44a), the solution becomes

$$\hat{w}_0(X,\omega) = \hat{I}_{app}(\omega)\frac{R_{P\infty}}{\eta}\frac{\cosh\left(\eta(X-L_x)\right)}{\sinh(\eta L_x)}, \tag{52a}$$

$$\hat{u}_0(X,Z,\omega) = \hat{w}_0(X,\omega)\frac{\cosh\left(\gamma(Z-L_z)\right)}{\cosh(\gamma L_z)}. \tag{52b}$$

Let η_R, γ_R be the real and η_I, γ_I be the imaginary parts of η and γ, respectively. Further, let

$$\alpha = \gamma_I L_z, \quad \beta = \gamma_R L_z, \quad \rho = \gamma_I L_x, \quad \omega = \gamma_R L_x. \tag{53}$$

The amplitude of the voltage response at location X to an sinusoidal input current with frequency ω is

$$|\hat{w}_0| = \frac{R_{P\infty}}{|\eta|}\sqrt{\frac{\cosh(2(\rho-\eta_R X))+\cos(2(\omega-\eta_I X))}{2(\sinh(\rho)^2+\sin(\omega)^2)}}, \tag{54a}$$

$$|\hat{u}_0| = |\hat{w}_0|\sqrt{\frac{\left(\sinh(2\beta)^2+\sin(2\alpha)^2\right)\left(\cosh(2(\beta-\gamma_R Z))+\cos(2(\alpha-\gamma_I Z))\right)}{\left(\cosh(2\beta)+\cos(2\alpha)\right)^2 2\left(\sinh(\beta)^2+\sin(\alpha)^2\right)}}, \tag{54b}$$

and the phase shift is

$$\arg\{\hat{w}_0\} = \arctan\left(\frac{\eta_R}{\eta_I}\right) - \arctan\left(\frac{\tan(\omega)}{\tanh(\rho)}\right) + \arctan\left(\frac{\tan(\eta_I X-\omega))}{\coth(\eta_R X-\rho))}\right), \tag{55a}$$

$$\begin{aligned}\arg\{\hat{u}_0\} = \arg\{\hat{w}_0\} \\ + \arctan\left(\frac{\sin(2\alpha)}{\sinh(2\beta)}\right) - \arctan\left(\frac{\tan(\alpha)}{\tanh(\beta)}\right) + \arctan\left(\frac{\tan(\gamma_I Z-\alpha)}{\coth(\gamma_R Z-\beta)}\right).\end{aligned} \tag{55b}$$

4.3.1.2.3 Current Injection into Branches

If a current I_{app} is applied to each branch, the boundary conditions for the primary neurite and the branches become:

$$\frac{\partial w_0}{\partial X}(0,T) = 0 \qquad \text{and} \qquad \frac{\partial w_0}{\partial X}(L_x,T) = 0. \tag{56a}$$

$$u_0(X,0,T) = w_0(X,T) \qquad \text{and} \qquad \frac{\partial u_0}{\partial Z}(X,L_z,T) = -R_{B\infty}\overline{n}I_{app}(X). \tag{56b}$$

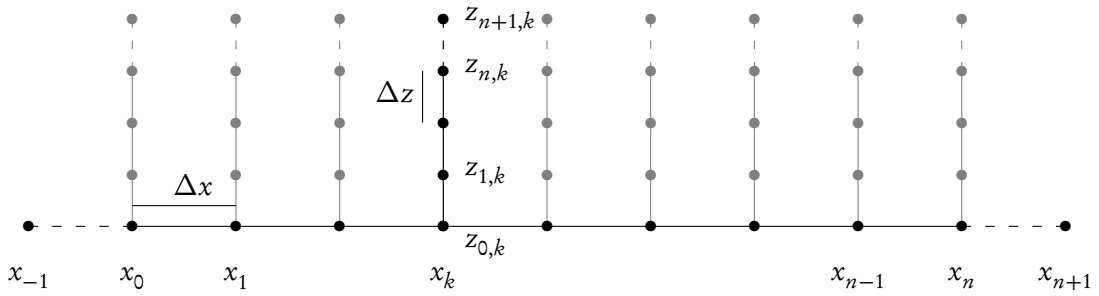

Figure 4.2 Finite differences grid. The points in the domain are on solid lines. Virtual grid points are on dashed lines and included to accommodate boundary conditions.

With boundary conditions from Eq. (56b), the steady-state voltage distribution of the branches is

$$u_0(X,Z) = w_0(X)(\cosh(Z) - \tanh(L_z)\sinh(Z)) - \frac{R_{B\infty}\overline{n}I_{app}(X)}{\cosh(L_z)}\sinh(Z). \tag{57}$$

Substitution of

$$\frac{\partial \hat{u}_0}{\partial Z}(X,0) = -w_0(X)\tanh(L_z) - \frac{R_{B\infty}\overline{n}I_{app}(X)}{\cosh(L_z)} \tag{58}$$

into Eq. (18a) gives

$$\frac{\partial^2 w_0}{\partial X^2} = w_0\left(1 + \overline{n}\frac{R_{P\infty}}{R_{B\infty}}\tanh(L_z)\right) + \frac{R_{B\infty}\overline{n}I_{app}}{\cosh(L_z)}. \tag{59}$$

For constant $I_{app}(X)$ the solution is

$$w_0 = \frac{R_{B\infty}\overline{n}I_{app}}{\cosh(L_z) + \overline{n}\frac{R_{P\infty}}{R_{B\infty}}\sinh(L_z)}. \tag{60}$$

4.3.1.2.4 Numerical Solution

For the finite difference approximation of $\frac{\partial \hat{u}_0}{\partial Z}(X,0,T)$ we use a one-sided approximation as in Eq. (28). i_{pb_i} in Eq. (29a) can now be substituted by

$$i_{pb_i} = \frac{1}{R_{B\infty}}(3u_{i,0} - 4u_{i,1} + u_{i,2}). \tag{61}$$

An illustration of the grid points is shown in Fig. 4.2.

4.3.2 Model Validation

In order to demonstrate the validity of the approach, the continuum branch model is compared to a multicompartment model with discrete branches implemented in NEURON, with parameters as summarized in Tab. 4.1. The passive electrical parameters R_a, R_m and C_m are as in Chapter 3. The parameters for the primary neurite d_p and l_p were set to the mean diameter and the length of the primary neurite between the first and the last subtree, as obtained from the three dimensional reconstructions. Further, $\overline{N}$ is determined by the mean density of the subtrees. The parameters of the branches are not strictly restricted to match the subtrees of MN5, since the major concern here is the comparison of the continuum model with a corresponding discrete model. l_p was set 100 µm, and d_b was set to be half of d_p.

Table 4.1 Parameters for the model

Symbol		Value	Units
R_m		6000	Ωcm^2
R_a		150	Ωcm
C_m		1.5	$\mu\text{F/cm}^2$
τ_m	$= R_m C_m$	9	ms
d_p		2	µm
λ_p	$= \sqrt{\frac{R_m d_p}{4R_a}}$	0.447	mm
$R_{P\infty}$	$= \frac{R_m}{\pi \lambda_p d_p} = \lambda_p r_{a_p}$	213.63	MΩ
l_p		74.4	µm
L_x	$= \frac{l_p}{\lambda_p}$	0.166	µm
$\overline{N}$		0.8199	/µm
$\overline{n}$	$= \lambda_p \overline{N}$	366.67	-
d_b		1	µm
λ_b	$= \sqrt{\frac{R_m d_b}{4R_a}}$	0.316	mm
$R_{B\infty}$	$= \frac{R_m}{\pi \lambda_b d_b} = \lambda_b r_{a_b}$	604.39	MΩ
l_b		100	µm
L_z	$= \frac{l_p}{\lambda_p}$	0.316	µm

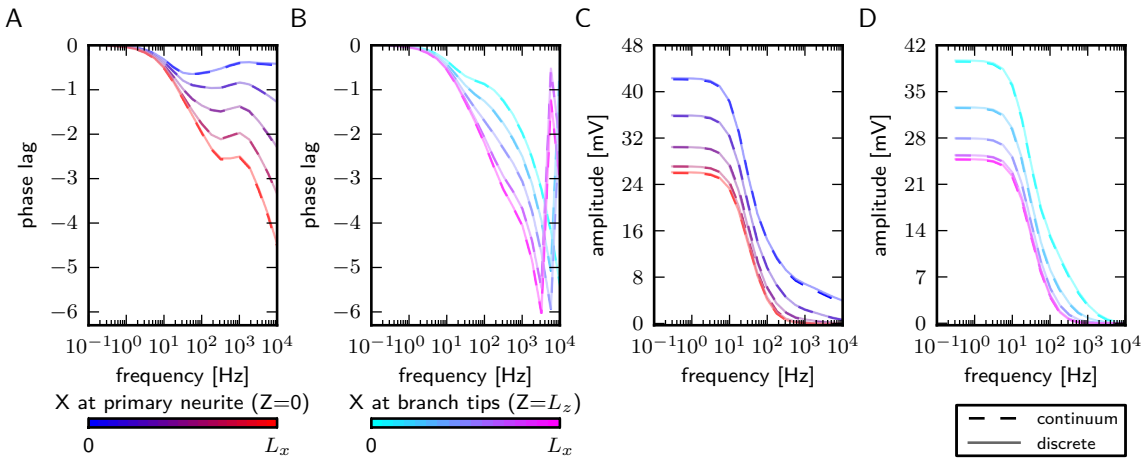

Figure 4.3 Comparison of transfer properties calculated with the continuum and discrete branch models. Responses to periodic forcing at location $X = 0$ with frequencies between $10^{-0.5}$ to 10^4 Hz. Input frequency dependence of the phase shift corresponding to the time delay of the voltage peak (A, B) and the maximal voltage response (C, D). Responses are measured along the primary neurite (A, C) and the branch tips (B, D).

4.3.2.1 Transfer Properties

The frequency dependent input and transfer properties, given as the amplitude and the phase lag, of the discrete and the continuum model were compared. For the continuum model this is done by solving Eqs. (54) and (55), and for the discrete model the Impedance-Class function of NEURON was used. The amplitude can be seen as the voltage change at a specified location in response to a sinusoidal current stimulus injected at the left end of the primary neurite. Here we use frequencies of $10^{-0.5}$,$10^{-0.25}$, … ,10^4 Hz and an amplitude of 1 nA. The phase lag corresponds to the delay between the peak of the current injection and the peak of the voltage response. Fig. 4.3 shows the results for the primary neurite and the endpoints of the branches, respectively. The frequency dependence of the phase lag and the amplitude at five locations x along the primary neurite and at the tips of five branches emerging from the primary neurite at location x, respectively are compared. For the chosen set of parameters, the analytic solution of the continuum model provides very good results for transfer properties with respect to current injection

to the primary neurite as compared to the discrete model. This holds for frequencies at least up to 10×10^4 Hz and all locations in the model.

4.3.2.2 Branch Density

The continuum formulation is based on an assumption that the branch density is 'high enough' for the continuum abstraction to result in accurate results. We vary the branch density $\overline{n}$ to get an estimate of the densities where the model is valid. The smallest possible density is constrained by the corresponding discrete model having a single branch. The error is accessed by calculating percentual difference of the voltage amplitude and the phase shift in response to sinusoidal current injection between the two models. As expected, reducing $\overline{n}$ first leads to a higher deviation from the discrete model (Fig. 4.4), which increases with increasing frequencies. However, the error decreases when the branch density approaches very small values. Only at the end of the primary neurite, where no current is injected ($X = L_x$), the error for high frequencies first decreases and then increases when decreasing $\overline{n}$ (Fig. 4.4 second column).

For frequencies up to 100 Hz the difference of the voltage amplitudes is smaller than 1 % and of the phase shift smaller than 2 % for the entire range of chosen $\overline{n}$ and all four locations. A frequency of 1000 Hz results in a maximal error of the voltage amplitude of about 5 %, which reduces to about 2.5 % when increasing $\overline{n}$ to 600. With high frequencies the error of the phase increases more at the location of the current injection as compared to the other locations. For 1000 Hz the maximal error at the location of current injection is about 6 % and reduces to about 3 %, while the maximum at the other locations is about 3 % and reduces to below 1 % with increasing $\overline{n}$.

Changing the geometric properties of the model should also have an effect on the deviation between the models. From Eq. (25a) it follows that decreasing $R_{P\infty}/R_{B\infty}$ reduces the

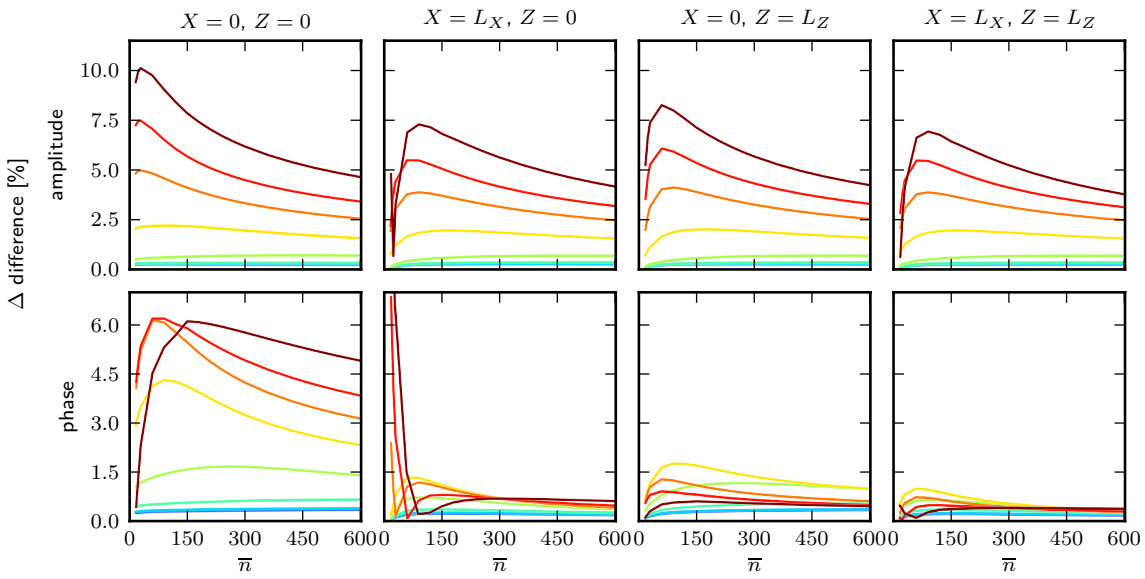

Figure 4.4 Differences between continuum and discrete model as a function of branch density $\overline{n}$. The amplitude (top) and the phase shift (bottom) of the continuum and discrete models in response to different frequencies are compared. The panels from left to right display the differences at four different locations as indicated; $Z = 0$ corresponds to locations at the primary neurite and $Z = L_Z$ to locations at the branch tips. Colors from blue to red represent frequencies from $10^{-0.5}$ to 10^4 Hz.

impact of the branches; therefore decreasing this ratio should improve the error. Decreasing the d_p increases $R_{P\infty}$, therefore it increases the ratio and leads to a higher deviation and increasing d_p has the opposite effect (Fig. 4.5A). Considering the limiting case, by letting $d_p \to 0$ it follows that $R_{P\infty} \to \infty$ and the models reduce to the standard cable model. Changing d_b has the inverse influence on the error between the models, since increasing it decreases $R_{B\infty}$ and therefore increases the ratio. This leads to a higher deviation and decreasing d_b has the opposite effect (Fig. 4.5B). For high frequencies and for small $\overline{n}$, the error increases by up to 15 %, when either d_p is decreased to be equal d_b, or d_b is increased to be equal d_p. In this case $\overline{n}$ has to be larger in order to achieve a good agreement between the models.

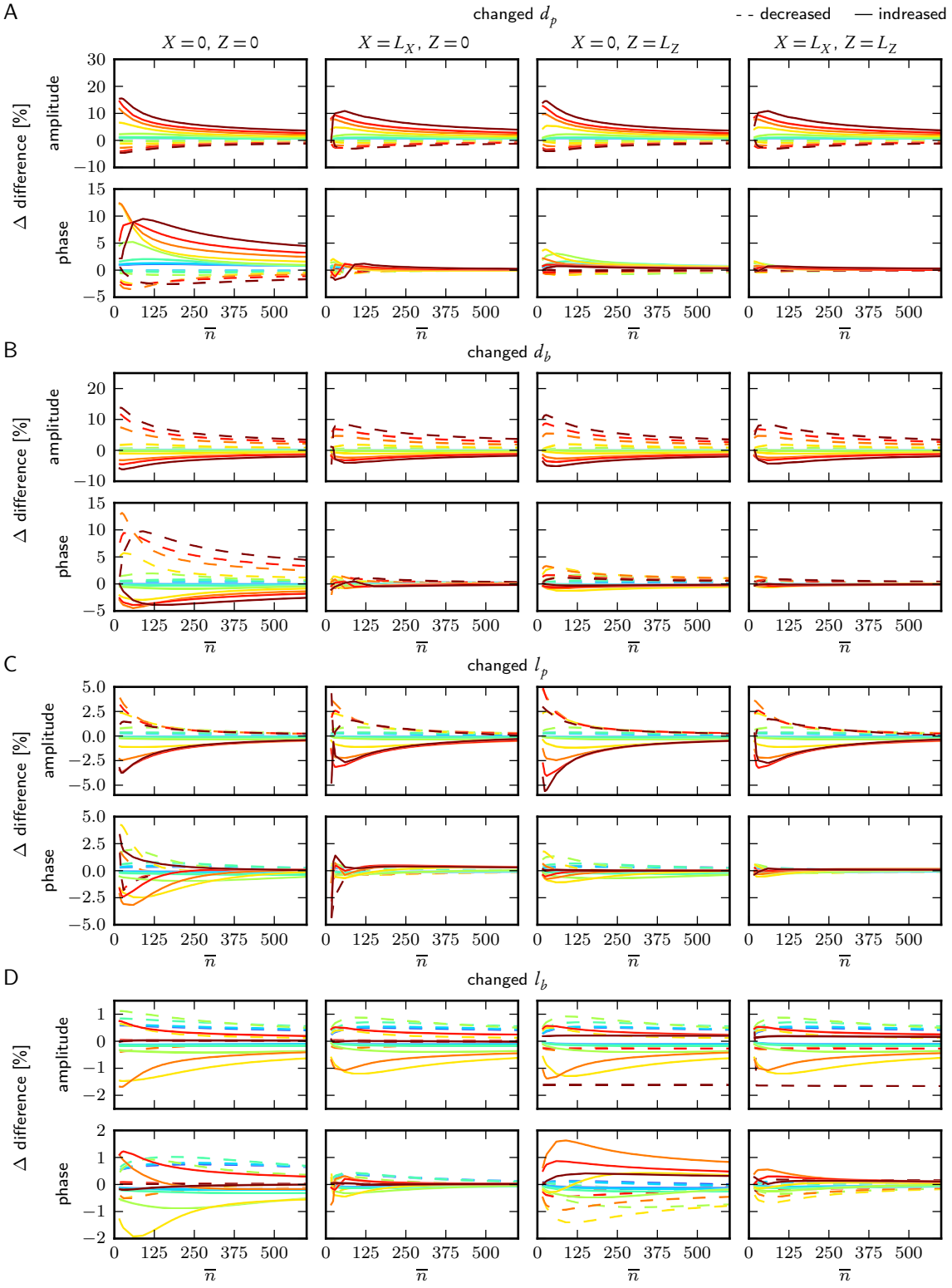
A
changed d_p
- - decreased
— indreased
$X = 0,\ Z = 0$
$X = L_X,\ Z = 0$
$X = 0,\ Z = L_Z$
$X = L_X,\ Z = L_Z$
Δ difference [%]
amplitude
phase
$\overline{n}$
B
changed d_b
C
changed l_p
D
changed l_b

Next we varied l_p, when increasing it amplified while decreasing it reduced the error of the maximal amplitude (Fig. 4.5C, top). The error of phase shift is frequency dependent (Fig. 4.5C, bottom), but for high $\overline{n}$ the difference in the error is below 1 %. Changing l_b has only a small effect on the error of both the amplitude and the phase shift (Fig. 4.5D). In the limiting case $l_b \to 0$ the model reduces to the standard cable model.

In summary, for large $\overline{n}$ the geometrical model parameters do not have much influence on the model accuracy compared to a discrete brach model.

4.3.2.3 Numerical Simulations

4.3.2.3.1 Passive Model

Next we compare the continuum branch model solutions obtained using the finite difference method to the results from the discrete model. Fig. 4.6A shows the voltage response to a 10 ms constant current injection to the primary neurite. Different d_b and l_b were used where the middle panel shows the model with the default parameters. All parameter combinations for the continuum branch model are in excellent agreement with the discrete model (see insets in Fig. 4.6A for enlargements).

4.3.2.3.2 Active Model

In a first step, we insert the voltage dependent ion channels from Chapter 2 uniformly over the entire membrane of both models and compare the responses to square pulse cur-

Figure 4.5 *(preceding page)* Influence of parameter variation on the differences between the continuum and discrete model. A-D: The differences to the results displayed in Fig. 4.9 are assessed. A: d_p is increased to 3 µm and decreased to 1 µm. B: d_b is increased to 2 µm and decreased to 0.5 µm. C: l_p is increased to 148.8 µm and decreased to 37.2 µm. D: l_b is increased to 500 µm and decreased to 50 µm. The panels from left to right display the differences at four different locations as indicated; $Z = 0$ corresponds to locations at the primary neurite and $Z = LZ$ to locations at the branch tips. Colors from blue to red represent frequencies from $10^{-0.5}$ to 10^4 Hz.

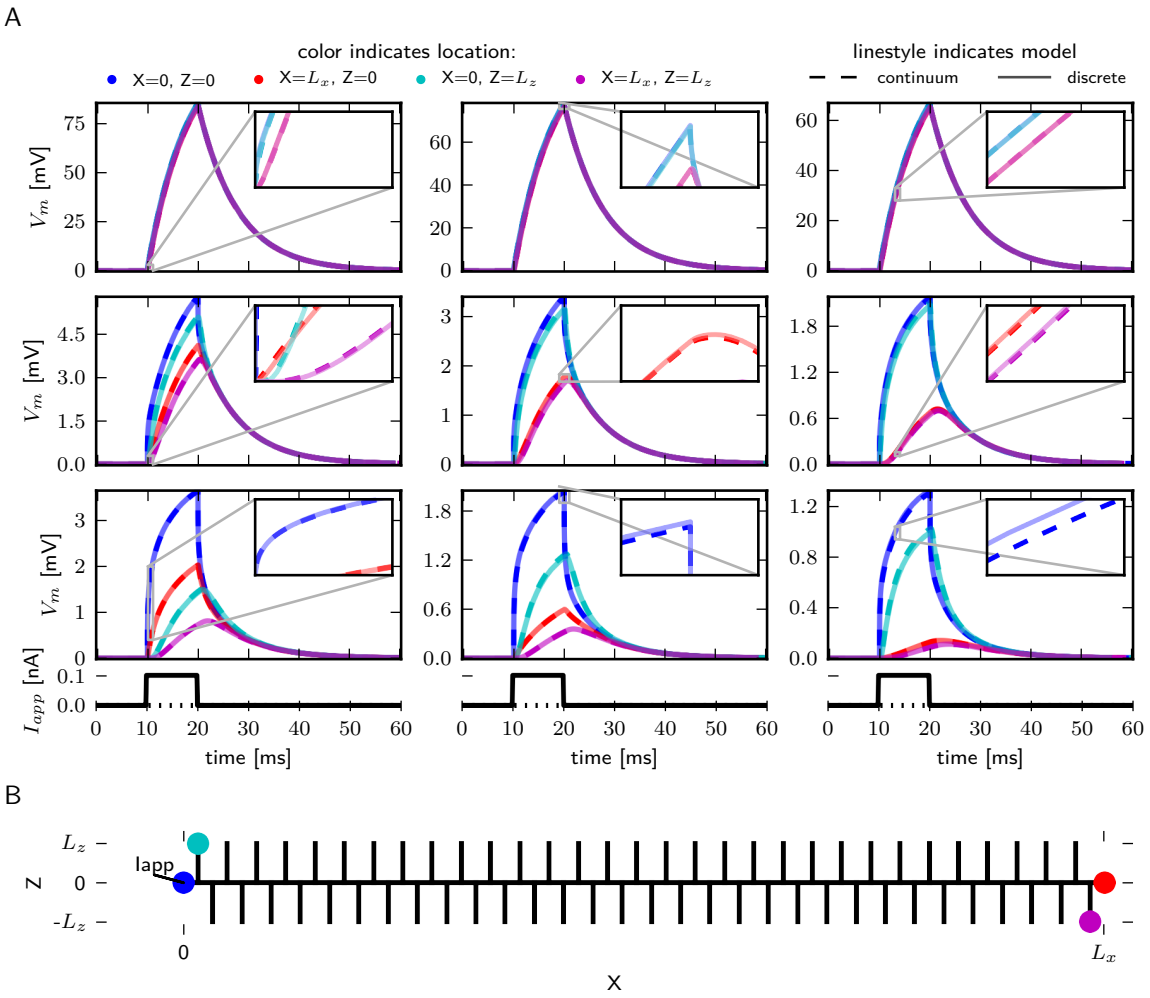

Figure 4.6 Numerical solution of the continuum and discrete branch model in response to constant current pulse. A: Comparison of the two models (dashed lines: continuum, solid lines: discrete) for different l_b (0.5, 100 and 300 µm from top to bottom) and d_b (0.5, 1 and 2 µm from left to right). The stimulus is applied to the left end of the primary neurite. Colors represent the different recording locations as indicated in B. B: Schematic of NEURON model with discrete branches, colored dots represent the recording locations.

rent injection (Fig. 4.7A). As before, different values for d_b and l_b are tested. The response of the two models are similar for some stimulus amplitudes. For other values differences are observed. This is expected, since even in the passive case there are deviations. However, the qualitative behavior is the same, only the sensitivity to the amplitude is warped. Therefore in an amplitude range where little changes in stimulus amplitude have little

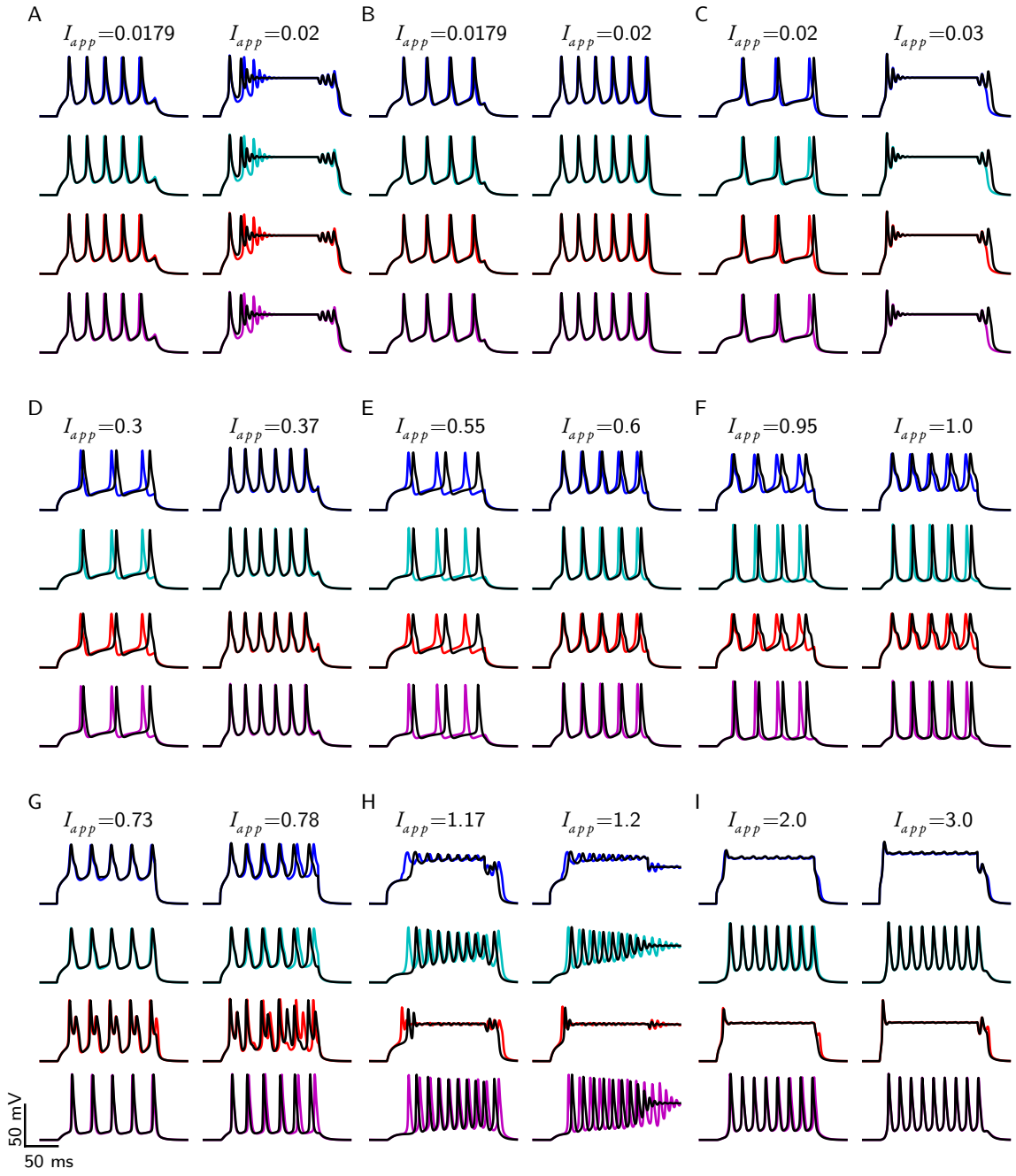

Figure 4.7 Comparison of the continuum and discrete branch model with voltage dependent ion channels. A-I: Responses of the discrete (black lines) and continuum (colored lines) models to two different stimulus amplitudes. From top to bottom different recording locations as indicated by the color for the continuum model (at $X = 0$ and $Z = 0$ (blue) and $Z = L_Z$ (cyan), at $X = L_X$ and $Z = 0$ (red) and $Z = L_Z$ (magenta)). In the panels A-I different values for l_b (from top to bottom) and d_b (from left to right) are used. A-C: l_b=0.5 µm, D-F: l_b=100 µm and G-I: l_b=300 µm; A,D,G: d_b=0.5 µm, B,E,H: d_b=1.0 µm and C,F,I: d_b=2.0 µm.

effect on the model response, there are no differences between the two models. On the other hand, in an amplitude range, where little changes in stimulus amplitude have a lage effect on the model response the two models display differences in the response and the models exhibit the same behavior in response to slightly different amplitudes.

4.3.3 Comparison to MN5

4.3.3.1 Reducing Morphology

We used the morphological realistic multicompartment models to generate and compare the continuum model. In the analyses carried out so far, the values for $\overline{n}$, l_b and l_p were determined by the data from the reconstructions. Since $\overline{n}$ is assumed to be constant for now, the model is symmetric with respect to stimulations at both sides. We first investigate whether this is also the case in the morphological realistic multicompartment model at the range where the subtrees branch off. The axon and the primary neurite at the soma end are cropped (Fig. 4.8A, dark gray area), since these are long portions of the neurite without branches. Stimulations at either side results in some differences between the voltage responses along the primary neurite (Fig. 4.8B). Visual inspection of the locations where the subtree branch off reveals that the first branches at either end have a bigger distance to the next subtree then subsequent branches. Therefore we remove those parts as well. This leads to an almost symmetric voltage attenuation in most of the reconstructions (Fig. 4.8B), indicating that uniform distributions of branches may be sufficient to model at least parts of MN5.

There is no obvious way to determine the parameters for the branches. Therefore, these parameters are obtained by fitting the maximal amplitude of the voltage responses of the continuum model to responses of the morphologically realistic model. We also fit

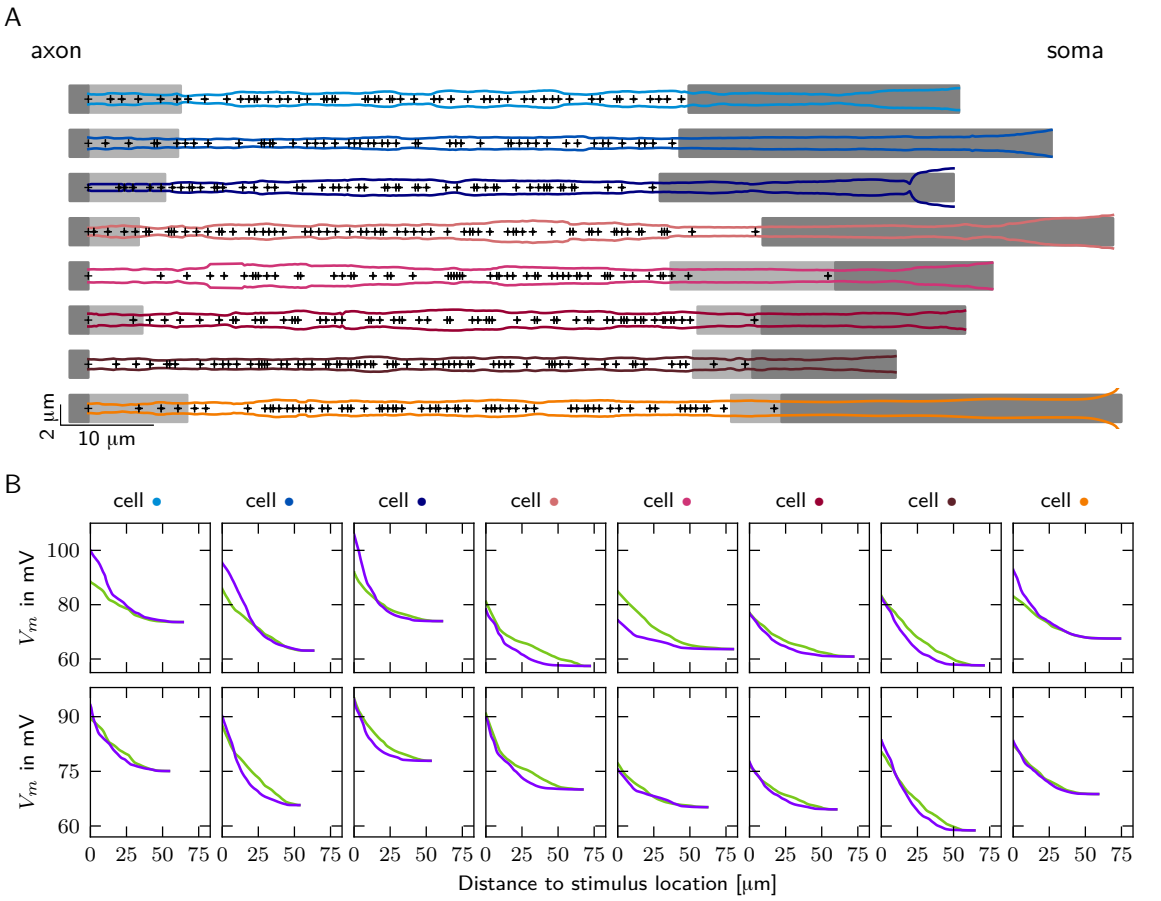

Figure 4.8 Symmetry of eight MN5 reconstructions.A: Primary neurite of eight MN5 reconstructions. Black pluses indicate the locations of emerging subtrees. Grey shaded areas indicate parts that are removed. B: Comparison of V_m along the cropped primary neurite in response to stimulation at the axon (purple) and soma end (green). Responses of the different reconstructions are displayed from left to right. In the top row only dark grey shaded areas are removed. In the bottom row both dark and light grey areas are removed.

d_p in order to compare it with the mean value of the primary neurite from the reconstructions.

The response to constant current injection and sinusoidal current injection with frequencies of 1.0, 10.0, 60.0, 100.0 and 1000.0 Hz are fitted simultaneously (Fig. 4.9). Superposition of V_m as a function of the location along the primary neurite of the two models in response to stimulation at the soma end (Fig. 4.9, top) and the axon end (Fig. 4.9,

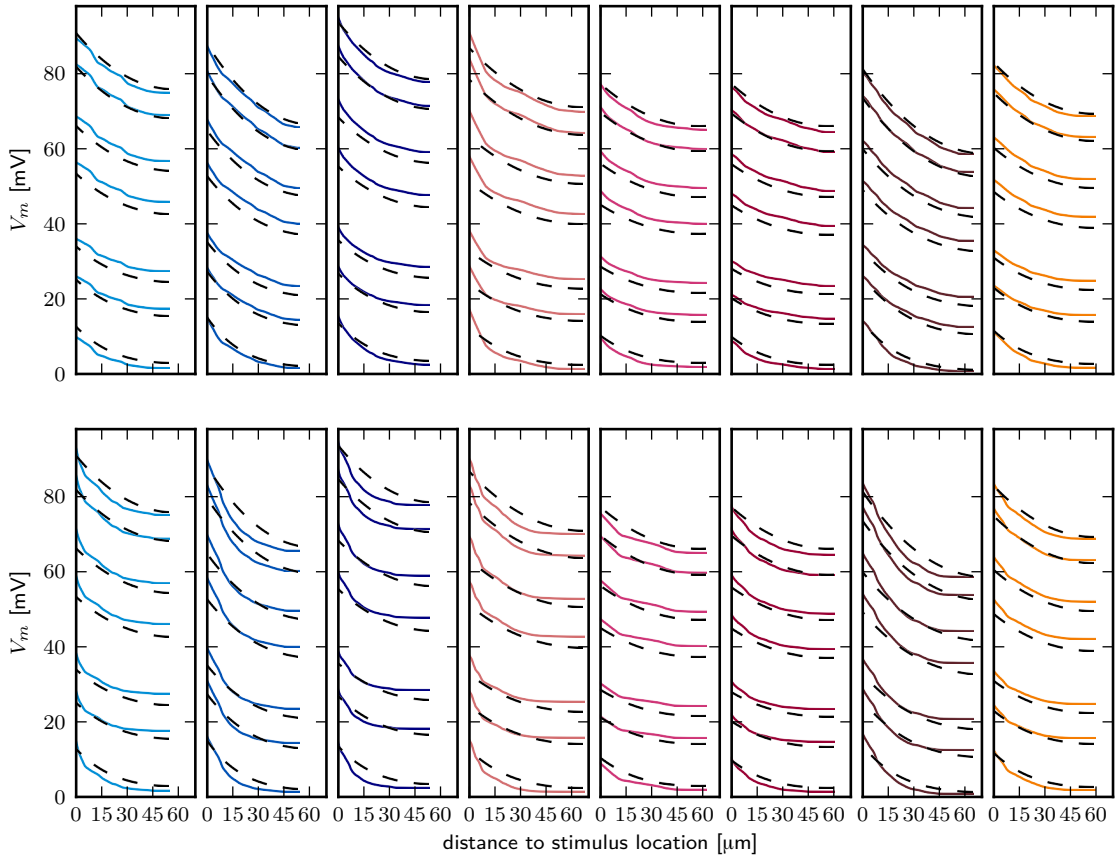

Figure 4.9 Fitting results. Response of cropped MN5 compartment model along the primary neurite to current injection at soma (top) and axon end (bottom) along with the results from the continuum branch model (black, dashed lines) with parameters obtained from fit to the corresponding MN5 model.

bottom) reveals that the continuum branch model provides good approximations of the responses elicited in some of the morphologically realistic models. As expected, the morphologically realistic models that displayed a big deviation of the voltage attenuation in the two directions can not be represented well by a continuum branch model with uniform $\overline{n}$. Tab. 4.3 summarizes the parameters obtained from the fits.

4.3.4 Continuum Branch Model of MN5

In order to model the linking segment that connects the soma with the branching part of MN5 as well as the axon, the $\overline{n}$ is changed with a Heaviside function. $\overline{n}$ is set to 0 for

Table 4.2 Model parameters to fit responses to stimulation at a single end. Parameters obtained from fitting of V_m of the morphologically realistic model to the continuum model. Responses to current injection to the axon and soma end where used as indicated.

reconstr.	d_b		l_b		d_p	
	axon	soma	axon	soma	axon	soma
cell 1	0.38	0.37	131.36	134.98	1.89	1.90
cell 2	0.43	0.40	130.36	140.53	1.46	1.55
cell 3	0.35	0.34	127.44	131.88	1.87	1.85
cell 4	0.34	0.32	114.82	122.07	1.95	2.05
cell 5	0.37	0.37	141.49	140.96	2.60	2.37
cell 6	0.38	0.37	125.51	127.87	2.31	2.34
cell 7	0.39	0.35	107.70	120.02	1.57	1.65
cell 8	0.34	0.34	122.82	124.12	2.11	2.07

Table 4.3 Model parameters to fit responses to stimulation at a single end . Parameters obtained from fitting of V_m of the morphologically realistic model to the continuum model. Responses to current injections at both ends are fitted simultaneously.

	parameter from fits			parameter from data		
reconstr.	d_b	l_b	d_p	l_p	$\overline{N}$	$\hat{D}_p$
cell 1	0.42	112.51	1.84	54.38	0.96	1.86
cell 3	0.45	119.98	1.51	53.41	0.95	1.51
cell 4	0.37	116.00	1.81	52.98	1.08	1.83
cell 2	0.37	102.34	2.00	66.85	1.02	1.97
cell 10	0.41	120.23	2.30	62.00	0.94	2.46
cell 11	0.43	105.16	2.26	60.04	1.03	2.20
cell 12	0.41	99.78	1.61	64.42	1.15	1.66
cell 18	0.38	105.25	2.02	58.86	1.14	1.95

x <37.7 μm or x >111.7 μm. We keep the branches passive, while the primary neurite is partially active. Active properties are inserted starting at four different locations and are uniformly distributed until the end of the primary neurite: x >=0 μm (the entire primary neurite is active), x >=50 μm, x >=100 μm (corresponding to results from Kühn and Duch (2013)) and x >=150 μm. In Chapter 2, $\overline{g}_{sb}$ and $\overline{g}_L$ were normalized to $\overline{g}_{Na}$. The maximal conductance of a channel can be seen as the product of the total channel

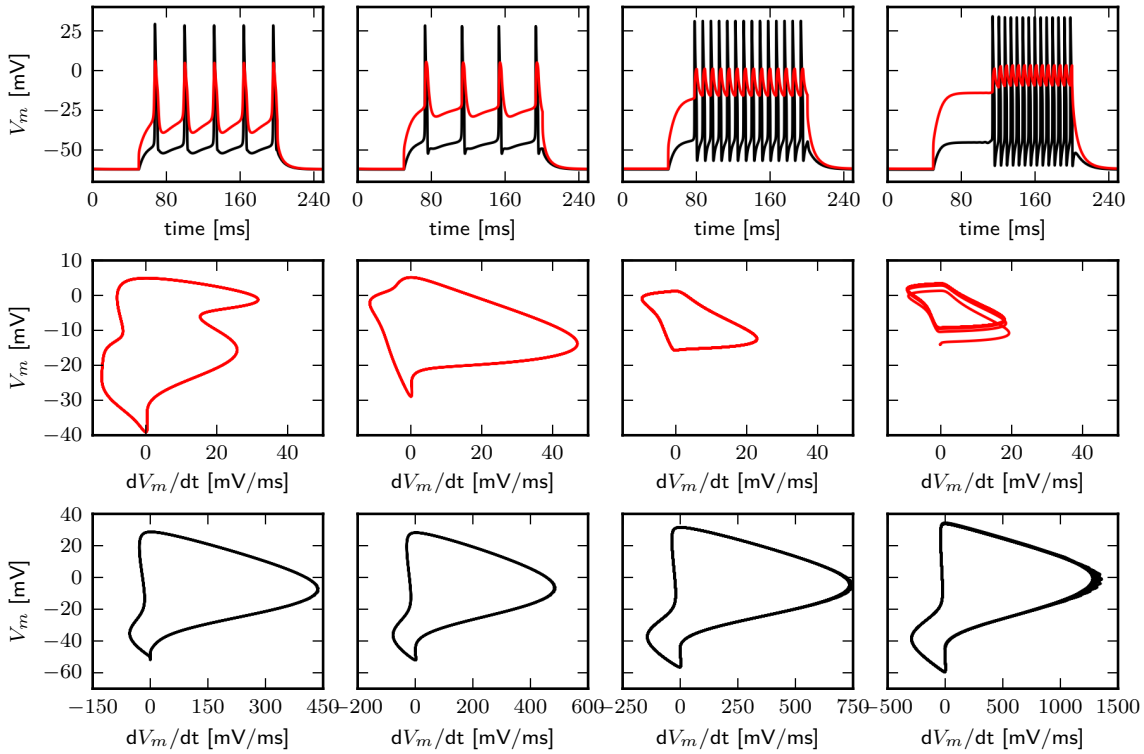

Figure 4.10 Membrane potential dynamics in response to current injection at the soma site. Response at the soma end (red lines) and axon end (black lines) to current injections just above the threshold. From left to right: channel onset location 0, 50, 100 and 150 µm. Top panels show the time evolution; middel and bottom panels the phase plot.

amount and the maximal conductance of a single channel. We start with setting the total amount of Na^+ channels to be the same as in Chapter 2. The amount of Shab channels is determined by the different $\widetilde{g}_{sb}$ used in Chapter 2. Leak channels are in the passive as well as in the active part of the model. We used $\overline{g}_L$ from Chapter 3 for the passive part and $\overline{g}_L$ from Chapter 2 for the active part and scaled those values to match the total amount of leak channels as determined by $\widetilde{g}_L$ from Chapter 2. Note that this approach results in different maximal conductances per unit area for different locations of active channel onset.

Current injection at the soma site with sufficient amplitude elicits repetitive spiking (Fig. 4.10). The amplitude of the APs at the end of the axon is similar for all channel onset

locations. As expected, the onset location has a severe effect on the amplitude at the soma end. However, even if the entire primary neurite is active the maximal depolarization at the soma is smaller than at the axon. The maximal $^{dV_m}/_{dt}$ at the soma is between 20 and 45 $^{mV}/_{ms}$ depending on the channel onset location, which corresponds to the range observed in MN5 (see Section 2.3.3.2).

4.3.4.1 Action Potential Amplitude

Since the maximal $^{dV_m}/_{dt}$ particularly for the channel onset at 100 µm is at the lower end of experimentally observed values we use three additional values for $\overline{g}_{Na}$, determined by the factor ξ by which the amount of Na^+ channels is increased as compared to the point model. In the following we use $\xi =$ 1, 1.5, 2 and 4. During repetitive firing, the minimal and maximal V_m at the end of the axon is only little affected by the location of channel onset and so is the amplitude (Fig. 4.11). Increasing ξ increases the amplitude from about 80 mV to 110 mV. $\widetilde{g}_{sb}$ has almost no effect on the amplitude, however moving the channel onset location from $x =$0 µm to $x =$150 µm $\widetilde{g}_{sb}$ has an increasing influence on the minimal and maximal V_m at the soma, while the minimal and maximal V_m at the axon end is not much effected.

The general slope of the maximal V_m as a function of the distance from the soma seems to be more influenced by the onset of the branches than by the location of channel onset. All channel onset locations, ξ and $\widetilde{g}_{sb}$ combinations have in common that the minimum is located within the branching region. The curve of the minimal V_m as a function of the distance from the soma reveals that the observation of spikes that sit on elevated potentials is a consequence of the spatial structure. The farther the channel onset is away from the soma, the higher the baseline depolarization.

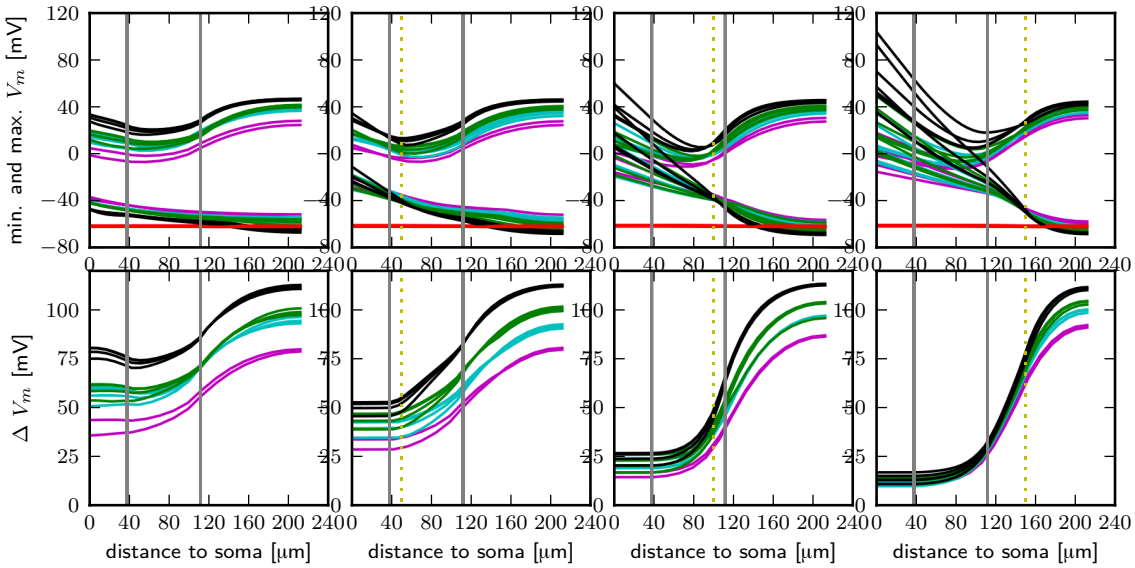

Figure 4.11 Action potential properties as a function of distance along the primary neurite. From left to right: Results for different onset locations of active channels (yellow lines indicate beginning of active part). Top: Minimal and maximal depolarization during an AP. Red lines show the resting membrane potential. Bottom: Amplitudes of APs. Gray lines indicate branches on and off set. Colors represent the ξ: magenta: 1; cyan: 1.5; green: 2, black: 4. Different lines of the same color are responses to different $\widetilde{g}_{sb}$ values.

4.3.4.2 Time to Peak

In order to further investigate the functional SIZ we evaluate the time to AP peak along the primary neurite. Other than in the case where the entire primary neurite is active, the location where active channels are started to be placed has little impact on where the peak is reached first (Fig. 4.12). It is always behind the branching part, along the axon. Only if the entire primary neurite is active, in most cases the peak is reached first at the soma site. But even under this conditions, for small channels densities the peak is reached first at the axon. Differences are be found in the shape of the curves. The curves for channels onset locations 50, 100 and 150 µm away from the soma display a sigmoidal course. The difference between the time to peak at axonal locations and the soma site increases when moving channel onset father away from the soma. Furthermore, for a

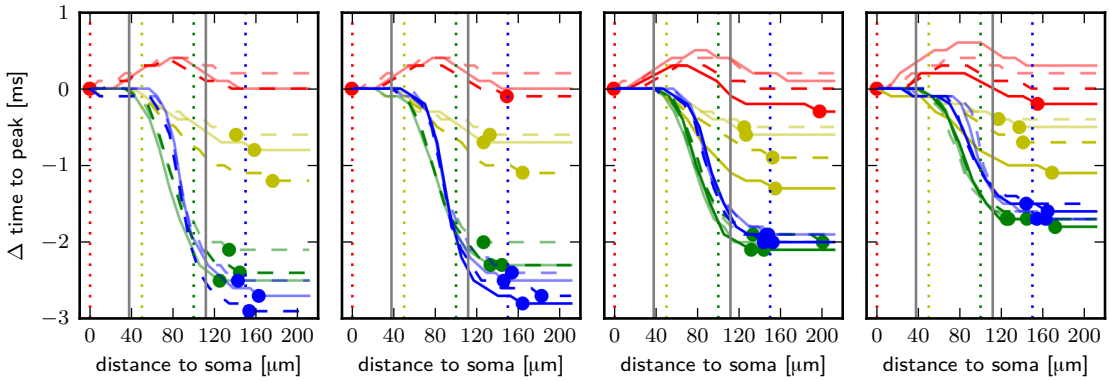

Figure 4.12 Time to peak as a function of distance along the primary neurite. From left to right: $\widetilde{g}_{sb}$= 0.57, 0.6, 0.782, 1.1382. Densityfactors are represented as follows: solid, dark :1, dashed dark: 1.5; solid, light 2, dashed, light: 4. Colors indicate different onset locations of active channels (dotted lines in the respective color indicate beginning of active part). Dots indicate location of minimal time to peak along primary neurite. Gray lines indicate branches on and off set.

channel onset 150 μm away from the soma, the beginning of the time difference increase tends to be farther away from the soma. While for the above considered channel onset locations the time to peak is reached last at the soma, when the entire primary neurite is active the time to peak is reached last at locations along the branching part. This indicates that the spike is initiated at two locations. The channel density has a minor impact on the curves. Increasing $\widetilde{g}_{sb}$ reduces the maximal difference of the time to peak for channel onset locations 100 and 150 μm. This, in particular, decreases the difference of the curves for channel onset locations along the branching part of the primary neurite 50 and 100 μm.

4.4 Discussion

The continuum branch formulation provides a link between analytical and computational approaches and it allows for detailed models of structural plasticity with the advantage that parameters like branch density can be varied dynamically.

The analytic estimates of electrical parameters are in good agreement with the discrete mode and so are numerical simulations. The continuum model provides a good approximation of the voltage response along the primary neurite of the branching part of MN5, even if using a uniform distribution of only one type of branches. Better results may be achieved by including more branch types with different distributions. For example, two types of branches could be used, in order to represent the many small subtrees with one type of branches and the big ones with another type of branches. Furthermore single subtrees that cannot be described with a distribution, could be modeled as discrete branches by including branch points.

The subtrees of MN5 are different from each other and not distributed uniformly. Even if two types of branches are modeled, the subtrees belonging to each group will show considerable differences. However, it is a better representation than using a ball and stick model or a two compartment model with one compartment representing the SIZ and another compartment the dendritic tree.

4.4.1 Continuum Branch Model of MN5

In order to investigate whether the SIZ can be determined by investigating the onset of Na^+ channels, we investigate the time to peak along the primary neurite. Interestingly, the channel onset location has not much impact on where the peak is reached first along the primary neurite. That implies that the onset of channels has only a minor impact on the SIZ, at least with uniform channel distribution over the active part of the model neuron. While there is experimental evidence that the distribution of Na^+ channels is uniform (Kühn and Duch, 2013), it is not known how Shab channels are distributed. Furthermore, additional channels may also influence the spike initiation. There are big

differences of the time to peak when the channel onset varies along the primary neurite, indicating that the exact location of the SIZ has a major impact on the membrane dynamics, at least in response to current injection at the soma.

Another approach to estimate the SIZ location was used by Gouwens and Wilson (2009). A passive multicompartment model was used, and a current that mimics the AP shape was injected at different locations. If this approach was valid it could be used to draw conclusions about the SIZ by analyzing the broadening and attenuation of APs measured in MN5 in conjunction with the voltage attenuation of the models measured in Chapter 3. Although we find that the amplitude measured at the soma site increases with increasing distance of the channel onset, the maximal amplitude of an AP occurs towards the end of the axon independent from channel onset.

CHAPTER 5

CONCLUSIONS

Drosophila has become an important model organism. However, not much is known about signal processing and propagation in its neurons. This is of particular interest since many invertebrate neurons have a monopolar structure, where the soma gives rise to the primary neurite from which the dendritic tree and the axon emerges. In these neurons the action potential is usually not initiated at the soma, which considerably distinguishes them from commonly studied vertebrate neurons. Besides morphologically realistic multicompartment models, we use spatially collapsed mathematical models and models with idealized structural features to analyze and compare the influence of locally changing dynamical profiles on neuronal output properties. The investigation of these models gives insight into properties that emerge from biophysical mechanisms, from cell geometry and from a combination of both in monopolar neurons. Reduced models have the advantage that they can reveal the general roles of the different underlying currents and make it possible to utilize a systematic approach to study the influence of certain parameters. This provides a better understanding of the mechanisms underlying model behavior. These results can help to build a framework to interpret electrophysiological experiments as well as to design them. Considerable insight in synaptic input integration in these neurons is given. Consequently, conclusions about the demand on spatio-temporal input patterns can be drawn.

The electrotonic distance from the SIZ indicates that MN5 is, compared to other cells, rather compact. Hence, it is possible that the reduction to a point model is sufficient in order to study the excitability of that neuron, with respect to the SIZ. However electrophysiological recordings are only available from the soma, which is electrotonically distant from the SIZ. At least in order to assess the impact of the dendritic load between the SIZ and stimulus and recording site on experimental results it is inevitable to include

the spatial dimension. The monopolar structure of the neuron with, as we find in Chapter 3, independently operating democratic subtrees emerging along the primary neurite motivates our approach of extending the point model developed in Chapter 2 to a model representing the primary neurite with an unbranched cable based description. This leads to the continuum branch model proposed in Chapter 4.

5.1 Future Directions

The continuum branch formulation will be used to study the impact of morphological variations of MN5 due to natural variability, genetic manipulations and across all developmental stages. Considering only the steady state voltage distribution in response to constant current injection, Eqs. (52) reduce to the regular cable equation. Therefore parameters can be found for which the voltage distribution is equivalent to the voltage distribution along the primary neurite of the continuum branch model (Eq. (52a)). However, if also considering periodic forcing, this does not hold. It would be interesting to investigate the impact of branch parameters on the frequency dependence of models that show the same steady-state voltage distribution for constant forcing. This will give insights on how branching influences transfer properties of neurons.

Further, A-type K^+ channels based on Shaker and Shal mediated currents in MN5 will be included in future models (Ryglewski and Duch, 2009). Incomplete space clamp has been found to influence the measurement of the kinetics from voltage dependent channels severely (Schaefer et al., 2003). Numerical simulations reveal that the activation curves measured in spatially extended model neurons do not reach saturation and are shallower as compared to curves measured in point models (Bar-Yehuda and Korngreen, 2008). This could explain why the activation curves of A-type channels measured in MN5 do not show saturation (Ryglewski and Duch, 2009). The continuum model will be used

to investigate the impact of branch density, distribution and parameters on the measurement of the kinetics from voltage dependent channels, by simulating voltage clamp experiments. We also will analyze the firing patterns that can be induced by varying the channel onset location, $\widetilde{g}_{sb}$ and the densityfactor, by calculating the f-I curves. Setting this In relation to the firing patterns found in Chapter 2 will give insight to whether varying $\widetilde{g}_{sb}$ has the same influence on the firing pattern as in the point model and further whether the channel onset locations play a role.

Input to branches also will be modeled. Some subtrees emerge from locations distal to the SIZ, meaning they emerge from the active part of the primary neurite. The exact location of the SIZ determines how many subtrees converge on the passive and how many converge on the active part of the primary neurite. This is likely to have an influence on synaptic integration and AP generation. Furthermore, it will be interesting to model inhibitory and excitatory together in order to investigate the impact of the experimentally observed GABAergic synapse placement on excitatory input.

REFERENCES

Baer, S. M. and J. Rinzel (1991). Propagation of dendritic spikes mediated by excitable spines: a continuum theory. *Journal of Neurophysiology*. 65(4):874.

Baines, R. and E. Pym (2006). Determinants of electrical properties in developing neurons. In: *Seminars in Cell and Developmental Biology*. Vol. 17-1. Elsevier:12–19.

Bar-Yehuda, D. and A. Korngreen (2008). Space-clamp problems when voltage clamping neurons expressing voltage-gated conductances. *Journal of neurophysiology*. 99(3):1127–1136.

Bekkers, J. M. (2011). Changes in dendritic axial resistance alter synaptic integration in cerebellar Purkinje cells. *Biophysical journal*. 100(5):1198–1206.

Borst, A. and J. Haag (1996). The intrinsic electrophysiological characteristics of fly lobula plate tangential cells: I. Passive membrane properties. *Journal of Computational Neuroscience*. 3(4):313–336.

Brembs, B., F. Christiansen, H. J. Pflüger, and C. Duch (2007). Flight initiation and maintenance deficits in flies with genetically altered biogenic amine levels. *The Journal of Neuroscience*. 27(41):11122–11131.

Brown, T., A. Zador, Z. Mainen, and B. Claiborne (1992). Hebbian computations in hippocampal dendrites and spines. In: *Single neuron computation*. Academic Press Professional, Inc.:116.

Bucher, D., C. D. Johnson, and E. Marder (2007). Neuronal morphology and neuropil structure in the stomatogastric ganglion of the lobster, Homarus americanus. *Journal of Comparative Neurology*. 501(2):185–205.

Carnevale, N. and D. Johnston (1982). Electrophysiological characterization of remote chemical synapses. *Journal of Neurophysiology*. 47(4):606.

Chen, X., L. Yuan, C. Zhao, S. Birnbaum, A. Frick, W. Jung, T. Schwarz, J. Sweatt, and D. Johnston (2006). Deletion of Kv4. 2 gene eliminates dendritic A-type K+ current and enhances induction of long-term potentiation in hippocampal CA1 pyramidal neurons. *Journal of Neuroscience*. 26(47):12143.

Choi, J., D. Park, and L. Griffith (2004). Electrophysiological and morphological characterization of identified motor neurons in the Drosophila third instar larva central nervous system. *Journal of Neurophysiology*. 91(5):2353.

Clewley, R., W. Sherwood, M. LaMar, and J. Guckenheimer (2007). PyDSTool, a software environment for dynamical systems modeling. *URL http://pydstool. sourceforge. net*.

Coetzee, W., Y. Amarillo, J. Chiu, A. Chow, D. Lau, T. McCormack, H. Morena, M. Nadal, A. Ozaita, D. Pountney, et al. (1999). Molecular Diversity of K^+ Channels. *Annals of the New York Academy of Sciences*. 868(1):233–255.

Corty, M., B. Matthews, and W. Grueber (2009). Molecules and mechanisms of dendrite development in Drosophila. *Development*. 136(7):1049.

Covarrubias, M., A. Wei, and L. Salkoff (1991). Shaker, Shal, Shab, and Shaw expresss independent K-current systems. *Neuron*. 7(5):763–773.

Crook, S. M., B. Ermentrout, and J. M. Bower (1998). Dendritic and Synaptic Effects in Systems of Coupled Cortical Oscillators. *Journal of Computational Neuroscience*. 5(3):315–329.

Cuntz, H., A. Borst, and I. Segev (2007). Optimization principles of dendritic structure. *Theoretical Biology and Medical Modelling*. 4:21.

De Schutter, E. (2002). *Computational neuroscience: realistic modeling for experimentalists*. CRC Press.

Diao, F., J. Chaufty, G. Waro, and S. Tsunoda (2010). SIDL interacts with the dendritic targeting motif of Shal (K(v)4) K+ channels in Drosophila. *Molecular and Cellular Neuroscience*. 45(1):75–83.

Dickinson, M. H. and M. S. Tu (1997). The Function of Dipteran Flight Muscle. *Comparative Biochemistry and Physiology Part A: Physiology*. 116(3):223 –238.

Doedel, E., R. C. Paffenroth, A. R. ChampneyS, T. Fairgrieve, Y. A. Kuznetsov, B. Oldeman, B. Sandstede, and X. Wang (2002). AUTO2000. *Concordia University*.

Duch, C., F. Vonhoff, and S. Ryglewski (2008). Dendrite elongation and dendritic branching are affected separately by different forms of intrinsic motoneuron excitability. *Journal of Neurophysiology*. 100(5):2525–2536.

Duch, C. and R. Levine (2000). Remodeling of membrane properties and dendritic architecture accompanies the postembryonic conversion of a slow into a fast motoneuron. *Journal of Neuroscience*. 20(18):6950.

Elburg, R. A. J. van and A. van Ooyen (2010). Impact of Dendritic Size and Dendritic Topology on Burst Firing in Pyramidal Cells. *PLoS Computational Biology*. 6(5):e1000781.

Endresen, L., K. Hall, J. Høye, and J. Myrheim (2000). A theory for the membrane potential of living cells. *European Biophysics Journal*. 29(2):90–103.

Ermentrout, B. (1996). Type I membranes, phase resetting curves, and synchrony. *Neural Computation*. 8(5):979–1001.

Ermentrout, B. (2002). *Simulating, analyzing, and animating dynamical systems: a guide to XPPAUT for researchers and students*. Vol. 14. Siam.

Ermentrout, B., M. Pascal, and B. Gutkin (2001). The effects of spike frequency adaptation and negative feedback on the synchronization of neural oscillators. *Neural Computation*. 13(6):1285–1310.

Ermentrout, G. B. and N. Kopell (1991). Multiple pulse interactions and averaging in systems of coupled neural oscillators. *Journal of Mathematical Biology*. 29(3):195–217.

Evers, J., S. Schmitt, M. Scholz, and C. Duch (2005). New frontiers in functional neuroanatomy: Precise automatic reconstruction from confocal image stacks. *Journal of Neurophysiology*. 93:2331–2342.

Fayyazuddin, A., M. A. Zaheer, P. R. Hiesinger, and H. J. Bellen (2006). The nicotinic acetylcholine receptor Dalpha7 is required for an escape behavior in Drosophila. *PLoS Biology*. 4(3):e63.

Fohlmeister, J. and R. Miller (1997). Impulse Encoding Mechanisms of Ganglion Cells in the Tiger Salamander Retina. *Journal of Neurophysiology*. 78(4):1935–1947.

Gasque, G., P. Labarca, E. Reynaud, and A. Darszon (2005). Shal and Shaker differential contribution to the K+ currents in the Drosophila mushroom body neurons. *Journal of Neuroscience*. 25(9):2348–2358.

Gidon, A. and I. Segev (2012). Principles governing the operation of synaptic inhibition in dendrites. *Neuron*. 75(2):330–341.

Goldberg, J. A., C. A. Deister, and C. J. Wilson (2007). Response Properties and Synchronization of Rhythmically Firing Dendritic Neurons. *Journal of Neurophysiology*. 97(1):208–219.

Goldman, M., J. Golowasch, E. Marder, and L. Abbott (2001). Global structure, robustness, and modulation of neuronal models. *Journal of Neuroscience*. 21(14):5229.

Gordon, S. and M. H. Dickinson (2006). Role of calcium in the regulation of mechanical power in insect flight. *Proceedings of the National Academy of Sciences*. 103(11):4311–4315.

Gouwens, N. W. and R. I. Wilson (2009). Signal propagation in Drosophila central neurons. *Journal of Neuroscience*. 29(19):6239–6249.

Greenwood, I. A. and N. Leblanc (2007). Overlapping pharmacology of Ca< sup> 2+</sup>-activated Cl< sup>-</sup> and K< sup>+</sup> channels. *Trends in pharmacological sciences*. 28(1):1–5.

Grolleau, F. and D. Sattelle (2000). Single channel analysis of the blocking actions of BIDN and fipronil on a Drosophila melanogaster GABA receptor (RDL) stably expressed in a Drosophila cell line. *British Journal of Pharmacology*. 130(8):1833–1842.

Guckenheimer, J., R. Harris-Warrick, J. Peck, and A. Willms (1997). Bifurcation, bursting, and spike frequency adaptation. *Journal of computational neuroscience*. 4(3):257–277.

Guckenheimer, J. and P. Holmes (1983). *Nonlinear oscillations, dynamical systems, and bifurcations of vector fields*. Vol. 42. New York Springer Verlag.

Gutkin, B., G. Ermentrout, and M. Rudolph (2003). Spike generating dynamics and the conditions for spike-time precision in cortical neurons. *Journal of Computational Neuroscience*. 15(1):91–103.

Harcombe, E. and R. Wyman (1977). Output pattern generation by Drosophila flight motoneurons. *Journal of Neurophysiology*. 40(5):1066–77.

Häusser, M. (2001). Synaptic function: dendritic democracy. *Current Biology*. 11(1):R10–R12.

Häusser, M. and B. Mel (2003). Dendrites: bug or feature? *Current Opinion in Neurobiology*. 13(3):372–383.

Häusser, M., N. Spruston, and G. Stuart (2000). Diversity and dynamics of dendritic signaling. *Science*. 290(5492):739.

Herrera-Valdez, M. A., S. Berger, C. Duch, and S. Crook (2009). Predicting changes in neuronal excitability type in response to genetic manipulations of K+-channels. *BMC Neuroscience*. 10(Suppl 1):P301.

Herrera-Valdez, M. A., S. Berger, C. Duch, and S. Crook (2010). Differential contribution of voltage-dependent potassium currents to neuronal excitability. *BMC Neuroscience*. 11:P159.

Herrera-Valdez, M. A., E. McKiernan, S. Berger, S. Ryglewski, C. Duch, and S. Crook (2012). Relating ion channel expression, bifurcation structure, and diverse firing patterns in a model of an identified motor neuron. *Journal of Computational Neuroscience*.1–19.

Herrera-Valdez, M. A. (2012). Membranes with the same ion channel populations but different excitabilities. *PLoS ONE*. 7(4):e34636.

St-Hilaire, M. and A. Longtin (2004). Comparison of coding capabilities of type I and type II neurons. *Journal of Computational Neuroscience*. 16(3):299–313.

Hille, B. (1992). *Ionic Channels of Excitable Membranes*. Sinauer Associates, Inc. Sunderland, Mass. 01375: Sinauer Associates.

Hines, M. L. and N. T. Carnevale (1997). The NEURON simulation environment. *Neural Computation*. 9(6):1179–1209.

Hines, M. L. and N. T. Carnevale (2001). NEURON: a tool for neuroscientists. *The Neuroscientist*. 7(2):123.

Hines, M. L., A. P. Davison, and E. Muller (2009). NEURON and Python. *Frontiers in neuroinformatics*. 3.

Hodgkin, A. (1948). The local electric changes associated with repetitive action in a non-medullated axon. *The Journal of Physiology*. 107(2):165.

Hodgkin, A. and A. Huxley (1952). A quantitative description of membrane current and its application to conduction and excitation in nerve. *The Journal of Physiology*. 117:500–544.

Hutcheon, B. and Y. Yarom (2000). Resonance, oscillation and the intrinsic frequency preferences of neurons. *Trends in Neurosciences*. 23(5):216–222.

Islas, L. and F. Sigworth (1999). Voltage sensitivity and gating charge in Shaker and Shab family potassium channels. *Journal of General Physiology*. 114(5):723.

Izhikevich, E. (2007). *Dynamical Systems in Neuroscience*. MIT Press, 55 Hayward Street, Cambridge MA 02142: MIT.

Jaffe, D. and N. Carnevale (1999). Passive normalization of synaptic integration influenced by dendritic architecture. *Journal of Neurophysiology*. 82(6):3268.

Jan, L. and Y. Jan (1997). Voltage-gated and inwardly rectifying potassium channels. *The Journal of Physiology*. 505(Pt 2):267.

Jan, Y., L. Jan, and M. Dennis (1977). Two mutations of synaptic transmission in Drosophila. *Proceedings of the Royal Society of London. Series B, Biological Sciences*. 198(1130):87–108.

Johnston, D., D. Hoffman, J. Magee, N. Poolos, S. Watanabe, C. Colbert, and M. Migliore (2000). Dendritic potassium channels in hippocampal pyramidal neurons. *The Journal of Physiology*. 525(1):75.

Katz, Y., V. Menon, D. Nicholson, Y. Geinisman, W. Kath, and N. Spruston (2009). Synapse distribution suggests a two-stage model of dendritic integration in CA1 pyramidal neurons. *Neuron*. 63(2):171–177.

Kirst, C., A. Herz, and M. Stemmler (2008). From Integrator to Resonator: The Effect of Dendritic Geometry on Neuronal Excitability. In: *Frontiers in Computational Neuroscience. Conference Abstract: Bernstein Symposium*.

Koch, C. and I. Segev (2000). The role of single neurons in information processing. *Nature Neuroscience*. 3(suppl 1):1171–1177.

Koenig, J. H. and K. Ikeda (1980a). Interspike interval relationship among flight muscle fibres in Drosophila. *Journal of Experimental Biology*. 87(1):137–147.

Koenig, J. H. and K. Ikeda (1980b). Neural interactions controlling timing of flight muscle activity in Drosophila. *Journal of Experimental Biology*. 87(1):121–136.

Koenig, J. H. and K. Ikeda (1983). Reciprocal excitation between identified flight motor neurons inDrosophila and its effect on pattern generation. *Journal of Comparative Physiology A: Neuroethology, Sensory, Neural, and Behavioral Physiology*. 150(3):305–317.

Kühn, C. and C. Duch (2013). Putative excitatory and putative inhibitory inputs are localised in different dendritic domains in a Drosophila flight motoneuron. *European Journal of Neuroscience*. 37(6):860–875.

Lee, J., A. Ueda, and C. Wu (2008). Pre-and post-synaptic mechanisms of synaptic strength homeostasis revealed by slowpoke and shaker K+ channel mutations in Drosophila. *Neuroscience*. 154(4):1283–1296.

Levine, J. and R. Wyman (1973). Neurophysiology of flight in wild-type and a mutant Drosophila. *Proceedings of the National Academy of Sciences*. 70(4):1050–1054.

Lewis, T. J. and J. Rinzel (2004). Dendritic effects in networks of electrically coupled fast-spiking interneurons. *Neurocomputing*. 58-60:145–150.

Lin, W.-H., C. Günay, R. Marley, A. A. Prinz, and R. A. Baines (2012). Activity-dependent alternative splicing increases persistent sodium current and promotes seizure. *The Journal of Neuroscience*. 32(21):7267–7277.

Lin, W., D. Wright, N. Muraro, and R. Baines (2009). Alternative Splicing in the Voltage-Gated Sodium Channel DmNav Regulates Activation, Inactivation, and Persistent Current. *Journal of Neurophysiology*. 102(3):1994.

Li, Z., K.-I. Okamoto, Y. Hayashi, and M. Sheng (2004). The importance of dendritic mitochondria in the morphogenesis and plasticity of spines and synapses. *Cell*. 119(6):873–887.

London, M. and M. Häusser (2005). Dendritic computation. *Annual Review of Neuroscience*. 28:503–532.

Magee, J. C. and E. P. Cook (2000). Somatic EPSP amplitude is independent of synapse location in hippocampal pyramidal neurons. *Nature Neuroscience*. 3(9):895–903.

Mainen, Z. F., N. T. Carnevale, A. M. Zador, B. J. Claiborne, and T. H. Brown (1996). Electrotonic architecture of hippocampal CA1 pyramidal neurons based on three-dimensional reconstructions. *Journal of neurophysiology*. 76(3):1904–1923.

Mainen, Z. and T. Sejnowski (1996). Influence of dendritic structure on firing pattern in model neocortical neurons. *Nature*. 382(6589):363–366.

Major, G., A. Larkman, P. Jonas, B. Sakmann, and J. Jack (1994). Detailed passive cable models of whole-cell recorded CA3 pyramidal neurons in rat hippocampal slices. *Journal of Neuroscience*. 14(8):4613.

Marder, E. (2011). Variability, compensation, and modulation in neurons and circuits. *Proceedings of the National Academy of Sciences*.

Marder, E. and J. Goaillard (2006). Variability, compensation and homeostasis in neuron and network function. *Nature Reviews Neuroscience*. 7(7):563–574.

Mee, C., E. Pym, K. Moffat, and R. Baines (2004). Regulation of neuronal excitability through pumilio-dependent control of a sodium channel gene. *The Journal of Neuroscience*. 24(40):8695.

Meseke, M., J. F. Evers, and C. Duch (2009). Developmental Changes in Dendritic Shape and Synapse Location Tune Single-Neuron Computations to Changing Behavioral Functions. *Journal of Neurophysiology*. 102(1):41–58.

Miyazaki, M., K. Ohyama, D. Dunlap, and F. Matsumura (1996). Cloning and sequencing of the para-type sodium channel gene from susceptible and kdr-resistant German cockroaches (Blattella germanica) and house fly (Musca domestica). *Molecular and General Genetics*. 252(1):61–68.

Morris, C. and H. Lecar (1981). Voltage oscillations in the barnacle giant muscle fiber. *Biophysical Journal*. 35:193–213.

Naundorf, B., F. Wolf, and M. Volgushev (2006). Unique features of action potential initiation in cortical neurons. *Nature*. 440(7087):1060–1063.

Nusser, Z. (2009). Variability in the subcellular distribution of ion channels increases neuronal diversity. *Trends in Neurosciences*. 32(5):267–274.

O'Dowd, D. and R. Aldrich (1988). Voltage-clamp analysis of sodium channels in wild-type and mutant Drosophila neurons. *Journal of Neuroscience*. 8(10):3633–3643.

Olson, R., Z. Liu, Y. Nomura, W. Song, and K. Dong (2008). Molecular and functional characterization of voltage-gated sodium channel variants from Drosophila melanogaster. *Insect Biochemistry and Molecular Biology*. 38(5):604–610.

Peng, I.-F. and C.-F. Wu (2007). Differential contributions of Shaker and Shab K+ currents to neuronal firing patterns in Drosophila. *Journal of Neurophysiology*. 97(1):780.

Ping, Y., G. Waro, A. Licursi, S. Smith, D.-A. Vo-Ba, and S. Tsunoda (2011). Shal/Kv4 Channels Are Required for Maintaining Excitability during Repetitive Firing and Normal Locomotion in Drosophila. *PLoS ONE*. 6(1):e16043.

Poznanski, R. R. (1991). A generalized tapering equivalent cable model for dendritic neurons. *Bulletin of mathematical biology*. 53(3):457–467.

Prescott, S., Y. De Koninck, and T. Sejnowski (2008). Biophysical basis for three distinct dynamical mechanisms of action potential initiation. *PLoS Computational Biology*. 4(10).

Rall, W. (1962a). Electrophysiology of a dendritic neuron model. *Biophysical Journal*. 2(2 Pt 2):145.

Rall, W. (1962b). Theory of physiological properties of dendrites. *Annals of the New York Academy of Sciences*. 96(Mathematical Theories of Biological Phenomena):1071–1092.

Rall, W. (1964). Theoretical significance of dendritic trees for neuronal input-output relations. *Neural Theory and Modeling*.73–97.

Rall, W. and J. Rinzel (1973). Branch input resistance and steady attenuation for input to one branch of a dendritic neuron model. *Biophysical journal*. 13(7):648–688.

Remme, M. W. H., M. Lengyel, and B. S. Gutkin (2009). The role of ongoing dendritic oscillations in single-neuron dynamics. *PLoS Computational Biology*. 5(9):e1000493.

Remme, M. and J. Rinzel (2010). Role of active dendritic conductances in subthreshold input integration. *Journal of Computational Neuroscience*.1–18.

Rinzel, J. (1985). Excitation dynamics: insights from simplified membrane models. *Federation Proceedings*. 44(15):2944–2946.

Rinzel, J. and G. Ermentrout (1989). *Analysis of neural excitability and oscillations, Methods in neuronal modeling: From synapses to networks*.

Rinzel, J. and G. Ermentrout (1998). Analysis of neural excitability and oscillations. In: *Methods in neuronal modeling: from ions to networks*. Ed. by C. Koch and I. Segev. The MIT Press.

Rogero, O., B. Hammerle, and F. Tejedor (1997). Diverse expression and distribution of Shaker potassium channels during the development of the Drosophila nervous system. *Journal of Neuroscience*. 17(13):5108.

Av-Ron, E., H. Parnas, and L. Segel (1991). A minimal biophysical model for an excitable and oscillatory neuron. *Biological Cybernetics*. 65(6):487–500.

Roth, A. and M. Häusser (2001). Compartmental models of rat cerebellar Purkinje cells based on simultaneous somatic and dendritic patch-clamp recordings. *The Journal of physiology*. 535(2):445–472.

Ryglewski, S. and C. Duch (2009). Shaker and Shal mediate transient calcium-independent potassium current in a Drosophila flight motoneuron. *Journal of Neurophysiology*. 102(6):3673–3688.

Schaefer, A. T., M. Helmstaedter, B. Sakmann, and A. Korngreen (2003). Correction of Conductance Measurements in Non-Space-Clamped Structures: 1. Voltage-Gated K< sup>+</sup> Channels. *Biophysical journal*. 84(6):3508–3528.

Schaefer, J. E., J. W. Worrell, and R. B. Levine (2010). Role of intrinsic properties in Drosophila motoneuron recruitment during fictive crawling. *Journal of neurophysiology*. 104(3):1257.

Schmitt, S., J. F. Evers, C. Duch, M. Scholz, and K. Obermayer (2004). New methods for the computer-assisted 3-D reconstruction of neurons from confocal image stacks. *Neuroimage*. 23(4):1283–1298.

Schulz, D., J. Goaillard, and E. Marder (2006). Variable channel expression in identified single and electrically coupled neurons in different animals. *Nature Neuroscience*. 9(3):356–362.

Schulz, D., J. Goaillard, and E. Marder (2007). Quantitative expression profiling of identified neurons reveals cell-specific constraints on highly variable levels of gene expression. *Proceedings of the National Academy of Sciences*. 104(32):13187.

Schwemmer, M. and T. Lewis (2011). Effects of dendritic load on the firing frequency of oscillating neurons. *Physical Review E*. 83(3):031906.

Segev, I. and M. London (2000). Untangling dendrites with quantitative models. *Science*. 290(5492):744–750.

Segev, I., J. Rinzel, and G. Shepherd (1995). *The theoretical foundation of dendritic function: collected papers of Wilfrid Rall with commentaries*.

Shepherd, G. (2004). *The synaptic organization of the brain*. Oxford University Press, USA.

Silver, R. A. (2010). Neuronal arithmetic. *Nature Reviews Neuroscience*. 11(7):474–489.

Steuber, V., E. De Schutter, and D. Jaeger (2004). Passive models of neurons in the deep cerebellar nuclei: the effect of reconstruction errors. *Neurocomputing*. 58:563–568.

Stuart, G. and N. Spruston (1998). Determinants of voltage attenuation in neocortical pyramidal neuron dendrites. *The Journal of neuroscience*. 18(10):3501–3510.

Su, H. and D. K. O'Dowd (2003). Fast synaptic currents in Drosophila mushroom body Kenyon cells are mediated by alpha-bungarotoxin-sensitive nicotinic acetylcholine receptors and picrotoxin-sensitive GABA receptors. *Journal of Neuroscience*. 23(27):9246–9253.

Tateno, T., A. Harsch, and H. Robinson (2004). Threshold firing frequency-current relationships of neurons in rat somatosensory cortex: type 1 and type 2 dynamics. *Journal of Neurophysiology*. 92(4):2283.

Tateno, T. and H. Robinson (2006). Rate coding and spike-time variability in cortical neurons with two types of threshold dynamics. *Journal of Neurophysiology*. 95(4):2650.

Tateno, T. and H. Robinson (2007). Phase resetting curves and oscillatory stability in interneurons of rat somatosensory cortex. *Biophysical Journal*. 92(2):683–695.

Tsunoda, S. and L. Salkoff (1995a). Genetic analysis of Drosophila neurons: Shal, Shaw, and Shab encode most embryonic potassium currents. *Journal of Neuroscience*. 15(3):1741–1754.

Tsunoda, S. and L. Salkoff (1995b). The major delayed rectifier in both Drosophila neurons and muscle is encoded by Shab. *Journal of Neuroscience*. 15(7):5209–5221.

Ueda, A. and C. Wu (2006). Distinct frequency-dependent regulation of nerve terminal excitability and synaptic transmission by IA and IK potassium channels revealed by Drosophila Shaker and Shab mutations. *Journal of Neuroscience*. 26(23):6238.

Van Pelt, J., H. Uylings, R. W. Verwer, R. J. Pentney, and M. J. Woldenberg (1992). Tree asymmetry—a sensitive and practical measure for binary topological trees. *Bulletin of Mathematical Biology*. 54(5):759–784.

Vonhoff, F. and C. Duch (2010). Tiling among stereotyped dendritic branches in an identified Drosophila motoneuron. *Journal of Comparative Neurology*. 518(12):2169–2185.

Wei, A., M. Covarrubias, A. Butler, K. Baker, M. Pak, and L. Salkoff (1990). K+ current diversity is produced by an extended gene family conserved in Drosophila and mouse. *Science*. 248(4955):599.

Wilson, C. and M. Park (1989). Capacitance compensation and bridge balance adjustment in intracellular recording from dendritic neurons. *Journal of Neuroscience Methods*. 27(1):51–75.

Zador, A. M., H. Agmon-Snir, and I. Segev (1995). The morphoelectrotonic transform: a graphical approach to dendritic function. *The Journal of Neuroscience*. 15(3):1669–1682.

Zeberg, H., C. Blomberg, and P. Århem (2010). Ion Channel Density Regulates Switches between Regular and Fast Spiking in Soma but Not in Axons. *PLoS Computational Biology*. 6(4):e1000753.